ABSTRACT

Title of dissertation: REDUCED ORDER MODELING OF FLAPPING WING FLIGHT DYNAMICS

Kenneth MacFarlane, Doctor of Philosophy, 2017

Dissertation directed by: Professor J. Sean Humbert
Department of Aerospace Engineering

Flapping wing vehicles have become a compelling alternative to classical fixed or rotary wing aircraft, especially as unmanned aircraft technology focuses on smaller, more agile platforms. Flying insects provide an inspiration for the control of flapping wing platforms, using limited computational resources in their specialized neural pathways to generate robust, agile performance. The flapping wing design is less studied, and the underlying physical principles are often more complex – non-linear time varying dynamics are dominated by forcing due to complex, unsteady aerodynamics. Reduced order models are critical to formulating tractable sensing and control concepts from the complex physics of flapping wing flight. Previous research has focused on a single methodology for the estimation of flight dynamics. This dissertation investigates the reduced order modeling of flapping wing flight dynamics for the purposes of tractable simulation and control, comparing multiple methodologies. Simplification of rigid body vehicle dynamics due to both linearization and time-invariance is discussed, and computational and experimental verification is presented for a simplified model of flapping wing aerodynamics. Additionally, a novel

method is presented to maximize the agility and performance of a flapping wing vehicle when reducing the number of control inputs. These reduced order modeling techniques are applied to both a model of a small flying insect and to a flapping wing micro air vehicle.

REDUCED ORDER MODELING OF FLAPPING WING FLIGHT DYNAMICS

by

Kenneth MacFarlane

Dissertation submitted to the Faculty of the Graduate School of the
University of Maryland, College Park in partial fulfillment
of the requirements for the degree of
Doctor of Philosophy
2017

Advisory Committee:
Professor J. Sean Humbert, Chair/Advisor
Professor James Baeder
Professor Inderjit Chopra
Professor Anya Jones
Professor Kenneth Kiger

© Copyright by
Kenneth MacFarlane
2017

Acknowledgments

First and foremost, I would like to thank my advisor, Dr. J. Sean Humbert, who provided me this opportunity to work on an exciting new field. When I started looking for a place of graduate school study in aerospace engineering, I never thought I would study bugs! Much less be so impressed by them. Dr. Humbert, you maintain a sense of enthusiasm I doubt I will see again. Thank you for your support over the years. I will always aspire to maintain your level of energy.

I would also like to thank the rest of my committee: Dr. James Baeder, Dr. Inderjit Chopra, Dr. Anya Jones, and Dr. Kenneth Kiger. Each of whom has been willing to take the time to discuss my research despite their busy schedules. In addition to assistance with research, I owe much of my education to you. Dr. Baeder, thank you in particular for your assistance these past years: the code developed by you and your team forms the basis for an integral part of this work, but your instruction is even more integral. Dr. Chopra, thank you for your support as well over the years, and the opportunity to work with your team's flapping wing MAV that makes a great capstone to my work at UMD. Dr. Jones, thank you for the time you took discussing the vagaries and quirks of low Reynolds number flapping wing flight.

I also acknowledge the support and funding from the Army Research Lab Micro Autonomous Systems & Technology (MAST) CTA, without whose funding this research would not have been possible.

Nothing starts from scratch, and this dissertation stands on the shoulders of

some giants as well. I thank Dr. Imraan Faruque for his mentorship and friendship over the years. Imraan, you helped get me started on this project, and I have only followed in your footsteps since then. I can only hope to work together in the future. I must thank Brandon Bush for starting me up with his IBINS CFD solver, and the many hours spent instructing me on his code. Thanks also go to Micheal Elzinga and Micheal Dickinson for their help and collaboration in providing the opportunity to work with their RoboFly. Also to Dr. Moble Benedict for collaboration on the flapping wing MAV. I'm indebted to Nick Kostreski, for all those hours wrangling fruitflies in the bug lab. Finally, thanks to all the other members of the AVL over the years: Badri, Greg, Joe, Lina, Renee, Steve, Doug, Jishnu, Kedar, and Utsav. Without our discussions on MAVs, insect flight, control theory, and who knows what else, I'm sure we would all have stalled out.

Most of all I'm grateful to my family and friends who stuck with me over this long process. Dad, you were always ready to inspire my curiosity to learn all I could of the natural world. Mom, you instilled the discipline I needed to make the most of that. Billie, you are always there to talk to, and encourage me to take some time out for gaming. Duke, for inspiring me to go into engineering. My friends, particularly Gray and the brothers of Mathew House, thank you for all the support over the years. Finally, Katerina, without whose love and support I could not have completed this dissertation.

Contents

1. Introduction . . . 1
1.1 Motivation and Background . . . 1
1.1.1 Micro Air Vehicles . . . 1
1.1.2 MAV Technical Challenges . . . 6
1.1.3 Flapping Wing Flight . . . 10
1.1.4 Flapping Wing Dynamical Modeling . . . 14
1.2 Previous Modeling of Flapping Wing Vehicle Dynamics . . . 18
1.2.1 Bare-Airframe Dynamical Modeling . . . 18
1.2.2 Modeling Flapping Wing Control . . . 24
1.3 Dissertation Objectives and Approach . . . 25
1.3.1 Objectives . . . 25
1.3.2 Dissertation Organization . . . 28

2. Flapping Wing Kinematics . . . 31
2.1 Coordinates Definition . . . 31
2.2 Flight Capture and Kinematics Extraction . . . 35
2.2.1 Flight Capture Apparatus . . . 35
2.2.2 Insect Forward Flight Kinematics Extraction . . . 36
2.3 Idealized Insect Kinematics . . . 41
2.3.1 Hover Kinematics . . . 41
2.3.2 Biologically-Motivated Control Inputs . . . 43
2.4 Summary . . . 44

3. Flapping Wing Aerodynamics . . . 46
3.1 Motivation for Aerodynamic Modeling . . . 46
3.2 Previous Insect Aerodynamic Modeling . . . 47
3.3 Aerodynamic Estimation Methods . . . 48
3.3.1 Quasi-Steady . . . 49
3.3.2 Computational Fluid Dynamics . . . 53
3.3.3 RoboFly . . . 55
3.3.4 Comparison for Example Wingstroke . . . 56
3.3.5 Calculation of Power Required for Flight . . . 59
3.4 Summary . . . 62

4. Dynamical Modeling . . . 64
4.1 Rigid Body Dynamics . . . 64
4.1.1 Small Perturbation Theory . . . 65
4.1.2 Wingstroke Averaging . . . 67
4.2 Linear Time Invariant Models . . . 68
4.2.1 Hovering Flight . . . 68
4.2.2 Forward Flight . . . 74
4.3 Linear Time Periodic Model . . . 83
4.4 Summary . . . 91

5. Control Input Modeling . . . 94
5.1 Biologically-Motivated Input Modeling . . . 94
5.2 Reachability Analysis . . . 98
5.2.1 The Reachability Gramian . . . 98
5.2.2 Reachability Analysis of Biologically-Motivated Control Inputs 100
5.2.3 Power-Normalized Reachability . . . 103
5.3 Control Input Reduction . . . 109
5.3.1 Defining a More General Set of Flapping Wing Control Inputs 109
5.3.2 Energy-Optimizing Input Reduction . . . 111
5.3.3 Results for Forward Flying Insect . . . 114
5.3.4 Discussion . . . 121
5.4 Summary . . . 125

6. Application to Flapping Wing Micro Air Vehicle . . . 129
6.1 Motivation . . . 129
6.2 Flapping Wing Platform . . . 131
6.3 OVERTURNS Computational Solver . . . 132
6.4 Linear Dynamical Modeling . . . 134
6.4.1 Linear Time Invariant System . . . 134
6.4.2 Linear Time Periodic System . . . 137
6.5 Reachability Analysis for Kinematic Control Inputs . . . 142
6.6 Summary . . . 147

7. Conclusions and Future Work . . . 149
7.1 Conclusions . . . 150
7.1.1 Verification of a reduced-order aerodynamic method for dynamical modeling at insect scale . . . 150
7.1.2 Time-invariance assumptions . . . 153
7.1.3 Control input selection for flapping wing flight . . . 155
7.2 Future Work . . . 157

Appendix 161

A. Compilation of Stability and Control Derivatives 162
A.1 *Drosophila* 162
A.2 Flapping Wing MAV 164

B. Compilation of Linear Dynamical Systems 165

C. Flapping wing aerodynamic loads 168
C.1 *Drosophila* 168
C.1.1 Stability Derivatives 168
C.2 Flapping wing MAV 178

List of Tables

2.1 Kinematic parameters identified for freely-flying *Drosophila* in slow forward flight (FF1) and fast forward flight (FF2). (All angles are in degrees.) 38

5.1 Power normalized control derivatives. Each derivative is scaled to show the control force or moment obtainable with $1\mu J$. 105

6.1 Hankel operator norms of the system for a variety of control input options. The offset control input contributes most of the input-output energy for the system, but a linear combination of inputs $\mathbf{q_1}$ can get even closer to the maximal value that is given by a full range of the control inputs. 144

A.1 Longitudinal stability derivatives for the *Drosophila* in the three flight conditions studied in this work: hover, slow forward flight (FF1), and fast forward flight (FF2). The estimates based on each of the three aerodynamic methods are given here. Robofly results were not available for the hover condition. See discussion of these results in Chapter 4. 162

A.2 Lateral-Directional stability derivatives in the fast forward flight condition (FF2). The estimates based on the quasi-steady aerodynamic method and IBINS CFD solver are given here. Robofly results were not available for lateral-directional perturbations. See discussion of these results in Chapter 4. 163

A.3 Longitudinal control derivatives in the two flight conditions considered in this work: slow forward flight (FF1), and fast forward flight (FF2). The estimates based on the quasi-steady aerodynamic method and IBINS CFD solver are given here (CFD results are not available for control perturbations in FF1). See discussion of these results in Chapter 5. 163

A.4 Longitudinal stability derivatives for the flapping wing MAV in hover. See discussion of these results in Chapter 6. 164

A.5 Longitudinal control derivatives for the flapping wing MAV in hover. See discussion of these results in Chapter 6. 164

B.1 Longitudinal modes for the *Drosophila* in the three flight conditions studied in this work: hover, slow forward flight (FF1), and fast forward flight (FF2). Robofly results were not available for the hover condition. See discussion of these results in Chapter 4. 166
B.2 Lateral-directional modes for the *Drosophila* in the fast forward flight condition (FF2). Robofly results are not available for lateral-directional perturbations. See discussion of these results in Chapter 4. 167
B.3 Longitudinal modes of the flapping wing MAV in hover. See discussion of these results in Chapter 6. 167

List of Figures

1.1 Micro air vehicle reconnaissance will allow soldiers to view interiors of unknown, possibly dangerous, buildings. Search and rescue teams can explore unsafe structures without exposing themselves to danger. 2

1.2 Future micro air vehicle applications are not limited to government work. Clockwise from top left: UPS delivery drone developed by CyPhy Works, Amazon's delivery octoquad, Zipline delivery system dropping medical supplies, and Facebook's Aquila solar powered communications aircraft. 3

1.3 A selection of the wide variety of MAVs. Clockwise from top left: a fixed wing MAV (Black Widow [12]), coaxial rotor [17], Aerovironment Nano Hummingbird [18], Harvard's RoboBee [19], the Delfly Micro [20], micro helicopter (Walker CB100), and a flexible wing MAV [16]. 5

1.4 Flight time versus vehicle mass of several MAVs. Smaller vehicles struggle with endurance, regardless of platform design. (from Floreano & Wood (2015) [28]) 8

1.5 Thick turbulent vortex sheets form under a rotary wing at low Reynolds number. (from Ramasamy et al. (2007) [31]) 9

1.6 Tennekes' *Great Flight Diagram* shows relationship between cruising speed, wing loading, and weight among insects, birds, and man-made aircraft. [34] 11

1.7 Flow structures around a flapping wing at insect scale: "dss" refers to dividing stream surface, "le" designates leading edge, "te" trailing edge, and "SS vortex" refers to the combined starting/stopping vortex. Spanwise flow is believed to keep the leading edge vortex (LEV) attached over the span of a flapping wing for several chord lengths. From Van den Berg & Ellington (1997) [37] 13

1.8 Typical feedback loop structure. Control inputs and environmental disturbances are input to the system dynamics, onboard sensors detect the resulting vehicle motion, and sensing data is used to estimate that motion for use in future control inputs. Understanding the dynamics of the system will inform design and analysis of vehicle sensing and control. 15

1.9 Preferred sensing axes of the compound eyes (left) and ocelli (right) of a blowfly. From Parsons et al. (2010) [42] 16
1.10 The Robofly experimental test apparatus. [54] 20

2.1 Insect flapping motion is horizontal. The downstroke (A) is followed by pitching of the wing up (pronation) that rotates the leading edge of the wing to prepare for the upstroke. The upstroke (B) is then followed by another pitching rotation back (supination) so the leading edge is again forward for the downstroke. This motion features lift generation during both half-strokes. 32
2.2 The body and wing coordinate systems. The body coordinate system $\hat{\mathbf{e}}$ is fixed to the rigid insect body at the center of mass, with $\hat{e}_1$ pointing in the direction of forward flight, $\hat{p}_2$ pointing to the insect's right, and $\hat{p}_3$ down. The wing coordinate system $\hat{\mathbf{p}}$ remains fixed to the wing root, and rotates with the wing. Thus, $\hat{p}_1$ always passes through the chord of the wing away from the leading edge, $\hat{p}_2$ remains along the span of the wing, but $\hat{p}_3$ will be on the lower surface during downstroke and upper surface during the upstroke. 33
2.3 The definition of wing kinematic angles is dependent on the order of the rotation, in this case, a 3-1-2 rotation. When all wing kinematic angles are 0, the wings lie flat to either side with the wing coordinate frame ($\hat{\mathbf{p}}$) aligned with the body frame ($\hat{\mathbf{e}}$). The first rotation about $\hat{p}_3$ is the flap angle ϕ. The second rotation about $\hat{p}_1$ occurs after the first rotation, by the elevation angle ζ. The final rotation about $\hat{p}_2$ by the wing pitch angle α, occurs after both the ϕ and ζ rotations. . 34
2.4 The insect motion capture setup. A snapshot of a *Drosophila* in the flight chamber as photographed by the orthogonal camera setup. Digitization includes marking the head, tail, wing root, and wing tip, and fitting a wireframe over each wing. 35
2.5 Digitization of free flight insect motion used for the forward flight reference condition (a) in the body frame, where the kinematics can be seen to be relatively constant, and (b) in the global frame, where the steady forward flight motion can be seen. 37
2.6 Captured wing kinematics (above) from slow forward flying *Drosophila Melanogaster*. Phase portraits (below) show the leading edge of the wingtip as a dot, with a protruding stick to show wing pitch. 39
2.7 Captured wing kinematics (above) from fast forward flying *Drosophila Melanogaster*. Phase portraits (below) show the leading edge of the wingtip as a dot, with a protruding stick to show wing pitch. 40

2.8 Flat wingstroke kinematics for an idealized hovering insect. Wing kinematic angles (above) show a simple sine wave for the flapping angle and a square wave for the angle of attack. A dot-and-stick diagram in a phase portrait (below) provides more intuition for wing kinematics. Note the wing rotation is advanced – it pronates and supinates well before wing reversal. 42
2.9 Basic wing kinematic control inputs: stroke amplitude $\phi_{\max}$, stroke bias ϕ_{off}, and stroke plane tilt β. Note that due to the orientation of the wing coordinate y-axis $\hat{p}_2$, stroke plane tilt is positive when pitching the stroke plane back. 44

3.1 Lift and drag coefficients versus angle of attack for a rotating *Drosophila* wing at constant angle of attack. From Dickinson et al. (1999). . . . 50
3.2 The three immersed bodies (insect body and two wings) in the computational flow domain. The body remains stationary in the Cartesian grid while both wings rotate according to prescribed kinematics and force the aerodynamic flow. 54
3.3 Iso-surfaces of q-criterion of vorticity for the idealized hover kinematics near pronation. Vortical structures are shown attached to each wing and in the wake from previous strokes. 55
3.4 The Robofly experimental apparatus from below the flapping wings. . 56
3.5 Longitudinal loads throughout a wingstroke for a *Drosophila* in slow forward flight, as determined by the three modeling techniques: quasi-steady, computational, and experimental. 58

4.1 Aerodynamic loads of an idealized hovering *Drosophila* calculated by IBINS with translational perturbations in the x-direction from hover. CFD results are solid lines; Quasi-steady are dashed. 69
4.2 Time-averaged aerodynamic loads of an idealized hovering *Drosophila* with perturbations in longitudinal states. Circles show X, triangles Z, and squares M; results from the quasi-steady model are in black, CFD in blue. The resulting linear regressions are shown as dashed lines of the corresponding color. 71
4.3 Longitudinal LTI modes of an idealized hovering *Drosophila* in slow forward flight. Adding pitch rate feedback gives similar results to those presented in Faruque and Humbert (2011a). 72

4.4 Argand diagrams displaying the variation in eigenstructure for each aerodynamic model. Each plot shows the components of the eigenvector plotted on the complex plane, each component corresponding to an individual state. The first two modes shown are subsidence modes, and eigenvectors exist completely on the real axis. The second two modes are the oscillatory modes; the angle between u and q components shows the lead or lag in phase of the interchange of motion between the two components. Eigenvectors are scaled to unit norm. Note the isolation of vertical motion to the slow subsidence mode, λ_2. 73
4.5 Time-averaged aerodynamic loads of a forward flying *Drosophila* with perturbations in longitudinal states. Circles show X, triangles Z, and squares M; results from the quasi-steady model in black, CFD in blue, RoboFly in red. The resulting linear regressions are shown as dashed lines of the corresponding color. 75
4.6 Longitudinal LTI modes of a forward flying *Drosophila* in slow forward flight. 76
4.7 Longitudinal LTI modes of *Drosophila* in fast forward flight. 77
4.8 Comparison of longitudinal flight modes of *Drosophila* in fast and slow forward flight. Slow forward flight is shown with circles, fast with x's; as before, quasi-steady results are in black, CFD in blue, and RoboFly in red. 78
4.9 Argand diagrams displaying the variation in eigenstructure for each aerodynamic model. Each plot shows the components of the eigenvector plotted on the complex plane, each component corresponding to an individual state. Note that the heave dynamics are fully coupled to the surge and pitching motion in forward flight. 79
4.10 Time-averaged aerodynamic loads of a forward flying *Drosophila* with perturbations in lateral-directional states. Diamonds show Y, circles L, and triangles N; results from the quasi-steady model in black, CFD in blue. The resulting linear regressions are shown as dashed lines of the corresponding color. 81
4.11 Lateral-directional LTI modes of *Drosophila* in fast forward flight. . . 82
4.12 Rolling moment throughout a wingstroke in fast forward flight for varying sideslip. Quasi-steady results are dashed, CFD in solid. . . . 83
4.13 Surface plots of forces and moments as functions of both time and perturbation in pitch rate. The stability and control matrices can be characterized as functions of time by measuring the change in loads with perturbations in state or control input for each instant in time. . 85
4.14 LTI and LTP initial condition responses for fast forward flight *Drosophila* dynamics with an initial vertical velocity, showing 10 wing strokes (about 0.05 seconds). The LTP model contains more information on scales between wing strokes, evident here in the higher definition of the pitch rate response. 88

4.15 LTI and LTP initial condition responses for closed loop forward flight *Drosophila* dynamics over 100 wingstrokes (about 0.5 seconds). Full state feedback and LQR gains were utilized for closing the loop and stabilizing the system. The LTI characterization is close to the LTP model for this small vehicle with fast flapping frequency. 90

5.1 Aerodynamic loads for several perturbations of $\delta_{\phi_{\max}}$ during a wingstroke of forward flying *Drosophila* estimated via IBINS CFD. The wing stroke begins with the upstroke followed by the downstroke. The wing encounters higher local velocity on the downstroke than the upstroke due to incoming flow, leading to larger aerodynamic loading during the downstroke. Increasing $\delta_{\phi_{\max}}$ amplifies loads throughout the stroke. 96
5.2 Stroke-averaged longitudinal loads due to perturbations in control inputs from the forward flight reference condition. Circles show X, triangles Z, and squares M; results from the quasi-steady model in black, CFD in blue. The resulting linear regressions are shown as dashed lines of the corresponding color. 97
5.3 Frobenius norm of the reachability gramian for each of the example control inputs. 101
5.4 Example control input reachability ellipsoids projected onto the $[u, w]$ and $[q, \theta]$ planes. Each ellipsoid corresponds to system reachability given unit energy of that input ($\|\mathbf{u}(t)\| = 1$). 102
5.5 Aerodynamic power required during a single wingstroke with varying stroke amplitude. The wing stroke begins with the upstroke followed by the downstroke. The wing encounters higher local velocity on the downstroke than the upstroke due to incoming flow, resulting in larger aerodynamic power required during the downstroke. 104
5.6 Stroke-averaged power required with perturbations to control inputs. This average power is a combination of both aerodynamic and inertial power; see Equation 3.7. 104
5.7 Power normalized reachability ellipsoids for each control input show that stroke offset is an effective control term with lowest energetic cost. 106
5.8 Power normalized reachability ellipsoids for pairs of control inputs again show the great effectiveness of the stroke offset term. 107
5.9 The determinant and Froebinius norms of the reachability ellipsoid quantify the reachable space for each individual control term or set thereof. 107
5.10 Pitch rate feedback is added to stabilize the longitudinal modes for the fast forward flying *Drosophila*. 115
5.11 Frobenius norm of the reachability gramian for the first two reachability-maximizing combinations of the example control inputs. The linear combination of these inputs is given below. 117

5.12 Reachability ellipsoids for optimized example control inputs projected onto the $[u, w]$ and $[q, \theta]$ planes. Each ellipsoid corresponds to system reachability given unit energy of that input ($\|\mathbf{u}(t)\| = 1$). 118
5.13 Reachability ellipsoids for optimized general control inputs from projected onto the $[u, w]$ and $[q, \theta]$ planes. 120
5.14 Kinematics resulting from the reachability-maximizing linear combination of the first harmonic, $\mathbf{u}_{n=1}$. Baseline kinematics are in red, reachability-maximizing control input ($\mathbf{q}$) in black. 121
5.15 Kinematics resulting from the reachability-maximizing linear combination of the first and second harmonic $\mathbf{u}_{n=2}$. Baseline kinematics are in red, reachability-maximizing control input ($\mathbf{q}$) in black. 122
5.16 Kinematics resulting from the reachability-maximizing linear combination of the first through third harmonic kinematic control inputs, $\mathbf{u}_{n=3}$. Baseline kinematics are in red, reachability-maximizing control input ($\mathbf{q}$) in black. 123

6.1 The flapping wing MAV platform. 131
6.2 The overset mesh system used for this study. (a) The wing mesh surface with the backround mesh behind, (b) a chordwise view of the O-O wing mesh extending from the surface of the wing, and (c) a close-up view of the curvilinear O-O mesh around the leading edge of the wing. 133
6.3 Longitudinal loads on the flapping wing MAV throughout the wingstroke for variation in vertical motion, w, as estimated by OVERTURNS. Stroke reversals occur at $t/T = 0.25$ and $t/T = 0.75$. 135
6.4 Stroke-averaged longitudinal loads for the flapping wing MAV in perturbations away from the hovering flight condition. 136
6.5 Longitudinal linear modes for the flapping wing MAV. 136
6.6 Eigenstructure of the linear modes for the hovering flapping wing MAV. Each eigenvector (scaled to norm 1) is plotted on the Real-Imaginary plane. Note the complete decoupling of the heave motion in the slow subsidence mode λ_2. 137
6.7 Surface plots of longitudinal forces and moments as functions of both time and perturbation in heave velocity. Each of the five perturbation in Δw are shown in varying color bands. 138
6.8 LTI and LTP initial condition responses for the hovering flapper MAV with an initial forward velocity, showing 80 wing strokes (about 3.6 seconds). The LTP model contains more information on scales between wing strokes, evident here in the higher definition of the heave response. Both responses are unstable, but the LTP builds instability more quickly. Also note the decoupling of the heave response is an artifact of the LTI system. 139

6.9 LTI and LTP initial condition responses for closed loop longitudinal dynamics over 40 wingstrokes (about 1.8 seconds). Full state feedback and LQR gains were utilized for closing the loop and stabilizing the system. The LTI characterization fails to accurately predict the instability in the closed loop system. 141
6.10 CFD-estimated longitudinal loads on the flapping wing MAV throughout the wingstroke for variation in the amplitude control input, $\delta_{\phi_{\max}}$. 143
6.11 Stroke-averaged longitudinal loads for the flapping wing MAV in control input perturbations away from the hovering flight condition. . . . 143
6.12 Above, the Hankel norm of system for individual control inputs. Below, the projection of the Hankel norm onto the state-space for each input. Again, the stroke offset, $\delta_{\phi_{\text{off}}}$, contributes the most output energy. Like the forward flying *Drosophila*, the amplitude does not contribute high energy in the system statespace, but does project onto the heave state substantially more than the other control inputs. 145
6.13 Components of the reducing input vector $\mathbf{q}$ and the resulting Hankel operator norms for the flapper control inputs for a hovering reference condition. On the left are the results for the first, and most optimal, linear combination ($\mathbf{q_1}$); on the right is the second most optimal ($\mathbf{q_2}$). 146

C.1 Longitudinal loads calculated by the quasi-steady method over a single wingstroke for the *Drosophila* in hover. Left three plots show loads for varying Δu, center 3 show loads for varying Δw, right 3 show loads for varying Δq. 168
C.2 Longitudinal loads calculated by IBINS CFD over a single wingstroke for the *Drosophila* in hover. Left three plots show loads for varying Δu, center 3 show loads for varying Δw, right 3 show loads for varying Δq. 169
C.3 Longitudinal loads calculated by quasi-steady method over a single wingstroke for the *Drosophila* in slow forward flight. Left three plots show loads for varying Δu, center 3 show loads for varying Δw, right 3 show loads for varying Δq. 170
C.4 Longitudinal loads calculated by IBINS CFD over a single wingstroke for the *Drosophila* in slow forward flight. Left three plots show loads for varying Δu, center 3 show loads for varying Δw, right 3 show loads for varying Δq. 171
C.5 Longitudinal loads measured using Robofly over a single wingstroke for the *Drosophila* in slow forward flight. Left three plots show loads for varying Δu, center 3 show loads for varying Δw, right 3 show loads for varying Δq. 172
C.6 Longitudinal loads calculated using the quasi-steady method over a single wingstroke for the *Drosophila* in fast forward flight. Left three plots show loads for varying Δu, center 3 show loads for varying Δw, right 3 show loads for varying Δq. 173

C.7 Longitudinal loads calculated by IBINS CFD over a single wingstroke for the *Drosophila* in fast forward flight. Left three plots show loads for varying Δu, center 3 show loads for varying Δw, right 3 show loads for varying Δq. 174
C.8 Longitudinal loads measured using Robofly over a single wingstroke for the *Drosophila* in fast forward flight. Left three plots show loads for varying Δu, center 3 show loads for varying Δw, right 3 show loads for varying Δq. 175
C.9 Lateral-directional loads calculated by the quasi-steady method over a single wingstroke for the *Drosophila* in fast forward flight. Left three plots show loads for varying Δv, center 3 show loads for varying Δp, right 3 show loads for varying Δr. 176
C.10 Lateral-directional loads calculated by IBINS CFD over a single wingstroke for the *Drosophila* in fast forward flight. Left three plots show loads for varying Δv, center 3 show loads for varying Δp, right 3 show loads for varying Δr. 177
C.11 Longitudinal loads calculated by OVERTURNS CFD over a single wingstroke for the flapping wing MAV in hover. Left three plots show loads for varying Δu, center 3 show loads for varying Δw, right 3 show loads for varying Δq. 178
C.12 Longitudinal loads calculated by OVERTURNS CFD over a single wingstroke for the flapping wing MAV in hover. Left three plots show loads for varying Δu, center 3 show loads for varying Δw, right 3 show loads for varying Δq. 179

Nomenclature

α	Wing angle of attack, rad
α_{tip}	Wingtip angle of attack, rad
β	Stroke plane tilt, rad
Γ_G	Hankel operator of system G
$\delta_{[\cdot]}$	Control input in $[\cdot]$
$\Delta_{[\cdot]}$	State perturbation in $[\cdot]$
ζ	Wing elevation angle, rad
η	Power recovered due to wing elasticity, W
θ	Body pitch angle, rad
λ_i	Eigenvalue i
ρ	Air density, kg/m^3
ϕ	Wing stroke angle, rad
ϕ_{max}	Stroke amplitude, rad
ϕ_{off}	Stroke offset, rad
$\psi(t)$	Fundamental solution to linear system
Ψ_c	Controllability operator
Ψ_o	Observability operator
$\omega_{\mathbf{b}}$	Body angular velocity, rad/s
$\omega_{\mathbf{w}}$	Wing angular velocity, rad/s
A	Linear system matrix
A_{CL}	Closed Loop system matrix
A_z	LTI stability matrix transformed from LTP state space
B	Control Matrix
C	Sensitivity Matrix
C_D	Drag Coefficient
C_L	Lift Coefficient
$\bar{c}$	Mean chord length, m
$\{\hat{\mathbf{e}}_\mathbf{1}, \hat{\mathbf{e}}_\mathbf{2}, \hat{\mathbf{e}}_\mathbf{3}\}$	Body-fixed axes
$\mathcal{E}_c$	Reachable state space
E_{kin}	Kinetic energy, J
f	Stroke frequency, 1/s
g	Gravitational Acceleration, 9.81 m/s^2
$\mathbf{h}$	Vector from center of gravity to wing hinge, m
$\mathbf{F}$	Force vector $\mathbf{F} = [X, Y, Z]^T$
$I_{[\cdot]}$	Vehicle moments of inertia about y-axis, kgm^2
J	Cost function
k	Reduced frequency
K	Gain Matrix

L, M, N	Moments about body axes, Nm
$L_{[\cdot]}, M_{[\cdot]}, N_{[\cdot]}$	Moment stability and control derivatives relating L, M, and N to perturbations of $[\cdot]$
m	Vehicle mass, kg
$\{\hat{\mathbf{p}}_\mathbf{1}, \hat{\mathbf{p}}_\mathbf{2}, \hat{\mathbf{p}}_\mathbf{3}\}$	Wing-fixed axes
$\mathbf{q}$	Input reduction vector
p, q, r	Body angular rates $\omega_\mathbf{b}$ about body axes $\hat{\mathbf{e}}$, rad/s
P_{aero}	Aerodynamic power required for flight, W
P_{inert}	Inertial power required for flight, W
P_{tot}	Total power required for flight, W
$P_{[\cdot]}$	Power stability and control derivatives relating P to perturbations of $[\cdot]$
Q	Periodic transition matrix
Q_{CL}	Closed Loop periodic transition matrix
$\hat{r}_2$	Non-dimensional second moment of wing area
R	Wing span, m
$\mathbf{R}_{60}$	Vector to 60% span location, m
$\mathbf{R}_{\text{tip}}$	Vector to wingtip, m
Re	Reynolds number
S	Wing area, m^2
S_u	Control input scaling matrix
S_x	State scaling matrix
t	Time, s
T	Period of wing stroke, s
$T_{bw}(\theta)$	3-1-2 rotation matrix from wing axes $\hat{\mathbf{p}}$ to body axes $\hat{\mathbf{p}}$ by angle θ
$T_i(\theta)$	3D rotation matrix for rotation about i^{th} axis by angle θ
$\mathbf{u}$	Control input vector
$\tilde{\mathbf{u}}$	Reduced control input vector
u, v, w	x,y,z components of body velocity , m/s
$\mathbf{v_b}$	Body velocity, m/s
U_{tip}	Wing tip speed, m/s
U_{ref}	Average wing tip speed, m/s
W_c	Controllability Gramian
W_o	Observability Gramian
$\mathbf{x}$	State vector
$\mathbf{x_0}$	Initial state at $t = 0$
X, Y, Z	Forces in the $\hat{\mathbf{e}}_{\mathbf{1,2,3}}$ directions, N
$X_{[\cdot]}, Y_{[\cdot]}, Z_{[\cdot]}$	Force stability and control derivatives relating X, Y, and Z to perturbations of $[\cdot]$

$\mathbf{z}$ transformed LTI state space from LTP system: $\dot{\mathbf{z}}(t) = A_z\mathbf{z}(t)$

Abbreviations

CFD	Computational Fluid Dynamics
IBINS	Immersed Boundary Incompressible Navier Stokes
FAA	Federal Aviation Administration
LQR	Linear Quadratic Regulator
LTI	Linear Time Invariant
LTP	Linear Time Periodic
MAV	Micro Air Vehicle
OVERTURNS	Overset Transonic Unsteady Reynolds-averaged Navier Stokes
RANS	Reynolds Averaged Navier Stokes
SWaP	Size Weight and Power
VTOL	Vertical Take-Off and Landing

Chapter 1: Introduction

1.1 Motivation and Background

1.1.1 Micro Air Vehicles

The history of aircraft innovation throughout the 20th Century subscribed to the paradigm of 'higher and faster.' This was especially true in the realm of surveillance aircraft that had to outrun pursuing aircraft or surface to air missiles. In the 21st Century, another frontier for surveillance aircraft has opened in the opposite direction: micro air vehicles (MAVs). The advent of MAVs will allow reconnaissance below the tree line, down urban streets, and into buildings. Dangerous areas, concealed to high altitude reconnaissance, can now be scouted before sending in personnel, potentially saving the lives of service members and first responders.

MAV technology has a variety of opportunities outside the realm of government uses, and technology companies have recently begun to take notice. Unmanned air systems (UAS) have the potential to revolutionize a variety of currently untapped industries, including agriculture, civil engineering, architecture, and energy. [1] In 2013, Amazon, Inc. announced that it would begin using unmanned systems to deliver packages to customers' doorsteps. [2] Multiple companies have announced



Fig. 1.1: Micro air vehicle reconnaissance will allow soldiers to view interiors of unknown, possibly dangerous, buildings. Search and rescue teams can explore unsafe structures without exposing themselves to danger.

plans to deliver medical supplies in remote areas via small unmanned systems. [3–5] Facebook, Inc. has an ambitious plan to fly small unmanned solar powered systems to provide internet communications to undeveloped regions. [6].

In 2016, the Federal Aviation Administration (FAA) released a set of rules to govern appropriate use of small unmanned aircraft that will allow these businesses and others to legally operate in the US national airspace. [7] The demand for small unmanned air systems (both commercial and recreational) has been surprisingly strong: in the first month of registration for such aircraft, over 300,000 owners registered with the FAA. [8] With the new rules out in 2016, codifying the legal use of the airspace for these aircraft, the business and economic case only grows stronger.

Micro air vehicles are typically defined as an aircraft an order of magnitude smaller than the smallest system at the turn of the century (this usually leads to a definition of about 15 cm span). [9] The onset of MAV research is due to a variety



Fig. 1.2: Future micro air vehicle applications are not limited to government work. Clockwise from top left: UPS delivery drone developed by CyPhy Works, Amazon's delivery octoquad, Zipline delivery system dropping medical supplies, and Facebook's Aquila solar powered communications aircraft.

of technological precursors. Foremost among these advances is the availability of brushless electric motors combined with higher energy density lithium-based batteries. [10] Improved materials, especially composites, allows for construction of low weight and high strength components. Finally, the advancement of micro electrical mechanical systems (MEMS) has provided a variety of sensors useful for both vehicle control and payload.

Micro air vehicle development derives from its the radio controlled aircraft ancestry. Fixed wing MAVs were the first developed. Research into basic design parameters for smaller, non-recreational aircraft began in the 1990's. [9, 11] A variety of fixed wing designs began development soon afterwards. [12–15] These vehicles struggle with the endurance and range limitations of small scale flight, and their susceptibility to wind. With the goal of improving performance in these areas, aerodynamicists began to look at the complex unsteady flow structures at low Reynolds numbers (i.e. below 10^5); work that is still ongoing. Even so, fixed wing designs remain the best in terms of endurance and range for a given weight. A special set of aircraft designs, flexible wings, was developed specifically to counter the susceptibility of fixed wing MAVs to wind gusts. [16]

Rotary-wing MAVs offer the significant benefit over fixed wing designs by allowing hover and vertical take-off and landing (VTOL). This capability is critical in many missions, especially reconnaissance and surveillance. There are many variants of these designs from a single rotor [21], to a coaxial rotor [17], to multirotors [22]. MAV rotorcraft are more difficult to design and build and have lower range and

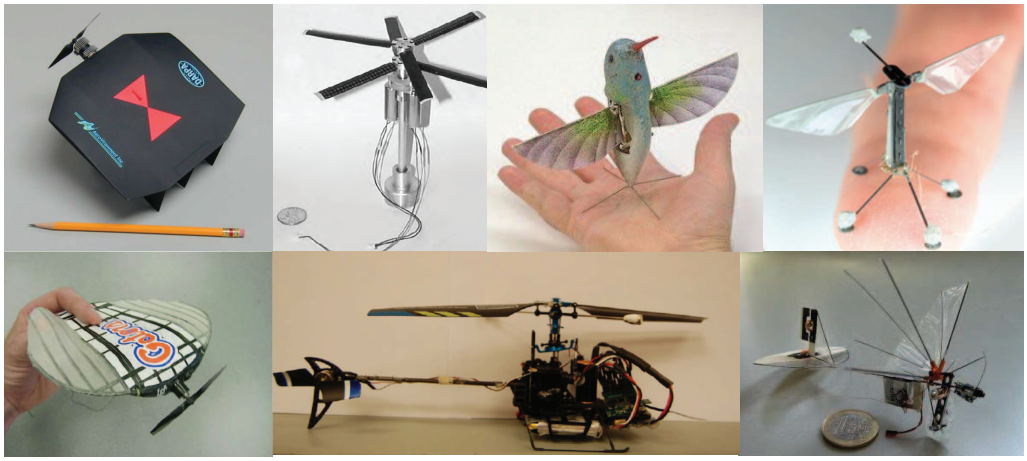


Fig. 1.3: A selection of the wide variety of MAVs. Clockwise from top left: a fixed wing MAV (Black Widow [12]), coaxial rotor [17], Aerovironment Nano Hummingbird [18], Harvard's RoboBee [19], the Delfly Micro [20], micro helicopter (Walker CB100), and a flexible wing MAV [16].

endurance than fixed wing MAV of a similar scale; however, the benefit of the VTOL capability is often worth these performance sacrifices. Shrouded rotor concepts have been developed with the aim of increasing endurance for hovering flight. [23] Control of rotary wing systems is more difficult than for fixed wings, due to inherent instabilities in vehicle dynamics. [24]

Flapping wing vehicles are the more complicated of MAV designs, inspired by avian and insect flight. Avian-style designs (often referred to as ornithopters), such as the RoboRaven [25] have a vertical wingstroke that generates thrust; lift is generated by air flowing over the wing similar to a fixed wing. Insect-based designs instead have a predominantly horizontal wingstroke that produces much of the lift. Due to the horizontal insect stroke, flow over the wings is not required to generate

lift, and such flapping wing MAVs are hover-capable. These designs range from the scale of an insect [19] to that of a hummingbird [18]. The aerodynamics and control of flapping wing systems are much more complicated than for rotary or fixed wing designs, and the mechanical construction is more involved and suffers under the oscillatory motion required for flapping. However, the agility of flapping wing systems may offer potential for gust-tolerant platforms, and the flapping wing motion could provide aerodynamic benefits that increase endurance and range. Additionally, the flapping wing design is much quieter, which can be essential for military missions.

Hover-capable flapping wing MAVs have similar control issues to rotorcraft, due to unstable dynamics. Moreover, the control actuation is more difficult on flapping wings, as there is no intuition and design basis as there is for rotorcraft. Several designs have used a tail to stabilize the vehicle in flight. [20, 26, 27] The tail reduces sensing and control requirements, but limits the vehicle's agility and increases it's susceptibility to environmental disturbances. The Aerovironment Nano Hummingbird, weighing only 19 grams with an endurance just over 10 minutes, is a particularly impressive tailless design, and has excited the possibility for future flapping wing system development.

1.1.2 MAV Technical Challenges

Design and operation of aircraft at smaller scales presents a variety of technical challenges. Size, weight, and power (or SWaP) restrictions are a concern for any aircraft design, but even more so for MAVs. SWaP restrictions limit vehicle

performance in all aspects of mission planning: endurance, range, maneuverability, and payload capability. As MAV design scales are reduced, the vehicles suffer from these restrictions even more (see Figure 1.4). Improvements in battery technology have allowed small scale flight, but decreasing battery size still limits energy storage. The ceiling on available power affects all aspects of vehicle design, including propulsion, control, communications, and payload. Computing and sensing are also severely limited by size and weight considerations. For small MAVs the electronics must often be custom built to fit these SWaP concerns. Mechanical construction of MAV-scale gearing and propulsion systems are also often custom-built, leading to further efficiency losses.

Limits to vehicle range and endurance are exacerbated by aerodynamic scaling. At low Reynolds numbers air becomes more viscous, decreasing the aerodynamic efficiency of the lifting surfaces. Large boundary layers increase the drag, and cause instabilities that lead to flow separation. Passive and active techniques have been studied to transition the laminar flow to turbulent and reattach flow, but these options are limited by construction and maintainability especially at smaller scales. [29] For hover-capable MAVs (including both rotary-wing and flapping wing platforms), the issue more complex. Shed boundary layers form vortex sheets that disrupt the vertical airflow below the vehicle (see Figure 1.5) [30]. These higher induced power requirements compound aerodynamic and SWaP constraints that limit vehicle endurance.

Sensing and control are also impacted by scale. Smaller vehicles' lower inertia

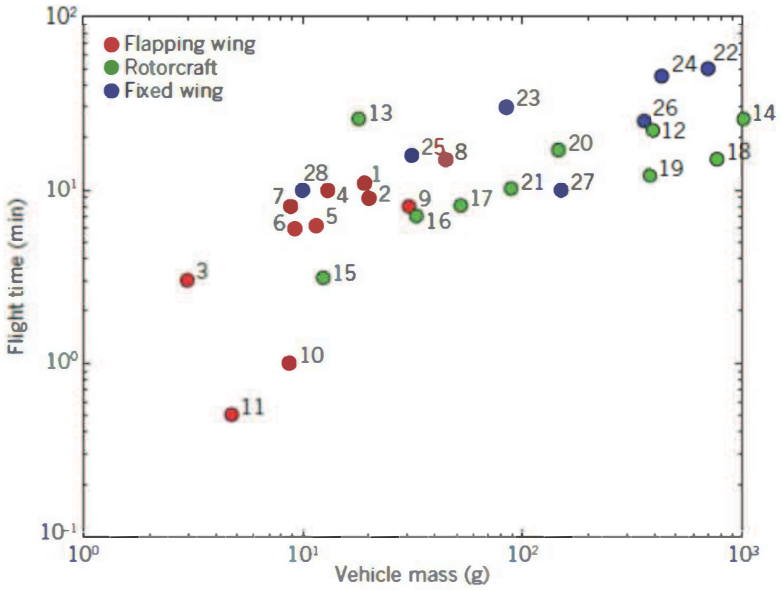


Fig. 1.4: Flight time versus vehicle mass of several MAVs. Smaller vehicles struggle with endurance, regardless of platform design. (from Floreano & Wood (2015) [28])

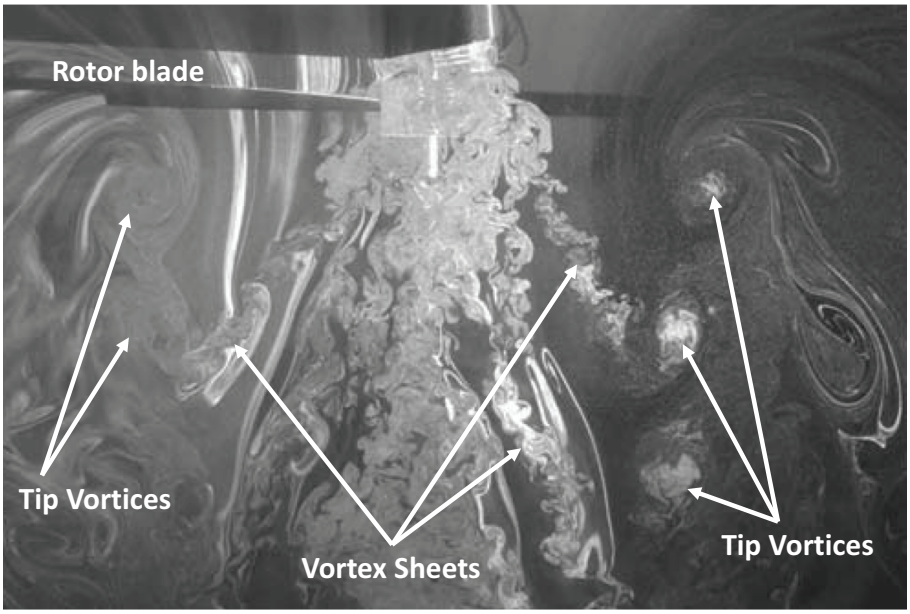


Fig. 1.5: Thick turbulent vortex sheets form under a rotary wing at low Reynolds number. (from Ramasamy et al. (2007) [31])

increases the speed of motion, rotational motion scales more strongly than translational. The mass of a vehicle scales with the cube of the length, while the moments of inertia scale by L^5. The beneficial result is an increase to vehicle agility, but it requires faster sensing and control capabilities. Because of SWaP limitations, high-bandwidth sensing and stability augmentation must operate with as little power and weight as possible. Unmanned vehicle sensing is dominated by a combination of GPS and inertial measurement units (IMUs) that track vehicle motion via translational and rotational accelerations. Neither of these sensors allow knowledge of the surrounding environment, and GPS availability is limited for indoor operation. Stability-enhancing mechanisms like a flybar or tail can reduce the speed of vehicle motion, but they decrease maneuverability and make the vehicle more susceptible

to environmental disturbances.

Environmental disturbances like wind gusts have proportionally greater effect on smaller scale vehicles. MAVs require higher thrust to weight ratios to counter sustained winds. Flexible wing vehicles are designed for the sole purpose of mitigating the gust-response issue of the fixed wing design. [16] Even light winds less than 2 meters per second (about 5 miles per hour) can keep rotary-wing MAVs grounded. [32] This limits MAV operation to indoor work, but fans, vents, and drafts can create challenging situations for a small MAV indoors.

1.1.3 Flapping Wing Flight

While many of the performance and scaling limitations of fixed and rotary wing flights are known, flapping wing flight offers a new paradigm. Like the soaring birds that inspired the Wright brothers and their contemporaries, birds, bats, and insects have long held the interest of those who hope to achieve robust stable flight at small scales. At smaller scales, successful man-made designs become sparse; however there are a multitude of biological specimen to study (see Figure 1.6). Natural flyers have been able to turn many of the above design challenges into advantages. From a mechanical systems perspective, biological flapping wing systems achieve truly impressive performance: about 50% of the body mass can be considered to be devoted to payload and sensing, while only 30% to structure and 20% to propulsion. [33] Studying these biological systems can provide intuition for more successful mechanical small scale flight.

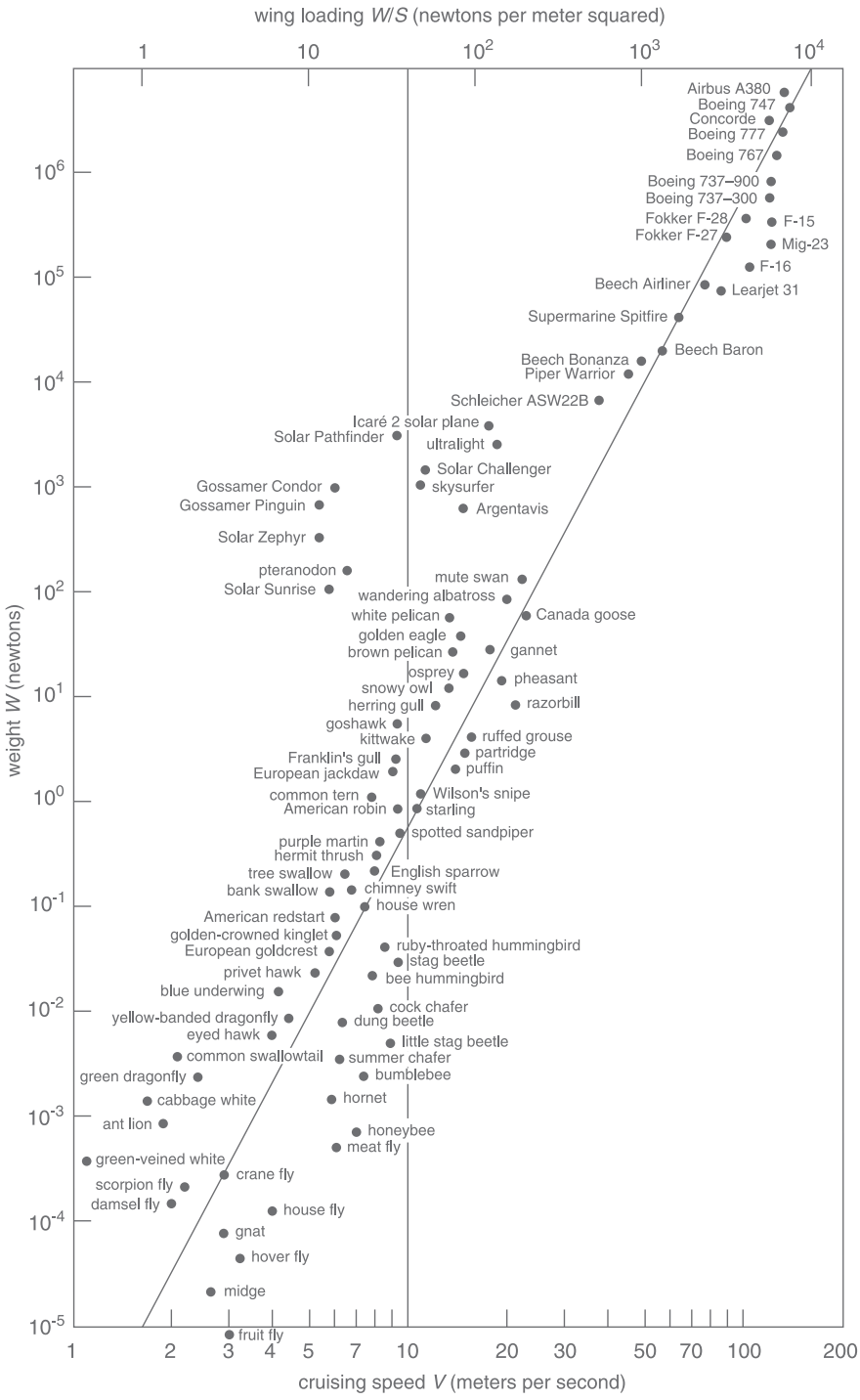


Fig. 1.6: Tennekes' *Great Flight Diagram* shows relationship between cruising speed, wing loading, and weight among insects, birds, and man-made aircraft. [34]

The earliest interest in the field comes from biologists interested in the design of the wings and the generation of aerodynamic forces. The highly unsteady and viscous flow around flapping wings is inherently difficult to understand and estimate; however, the popular saying that science cannot explain how a bee flies is certainly an exaggeration. Birds and insects have exploited the unsteady aerodynamic phenomena that limit the efficiency of their mechanical counterparts.

The importance of the unsteady aerodynamics is well documented and without accounting for these effects, an insect would not be able to generate enough lift to remain aloft. The laminar boundary layer separation on a flapping wing can manifest in a leading edge vortex (LEV). Recent work by Lentink & Dickinson has shown that spanwise flow generated by rotational acceleration keeps the LEV attached for several wingstrokes. [35] On a rotorcraft, the LEV may detach after several chord lengths of travel, but flapping wings stop and reverse motion twice each wingstroke. The LEV is reformed every half-stroke due to more rotational acceleration. The attached LEV and the low pressure it generates on the upper wing surface has been proven vital to generating the necessary lift for insect flight. [36]

At stroke reversal, vortex shedding and wake capture have substantial effect on the aerodynamic loading, but small changes in scale, wing planform, or kinematics could have dramatic effect on these unsteady phenomena. [38, 39] The benefits of a "clap and fling" of fluid around two wings meeting at the end of a stroke was first suggested by Weis-Fogh in 1973, but only recently has computational and experimental techniques tested the concept in detail. [40, 41] Even with considerable

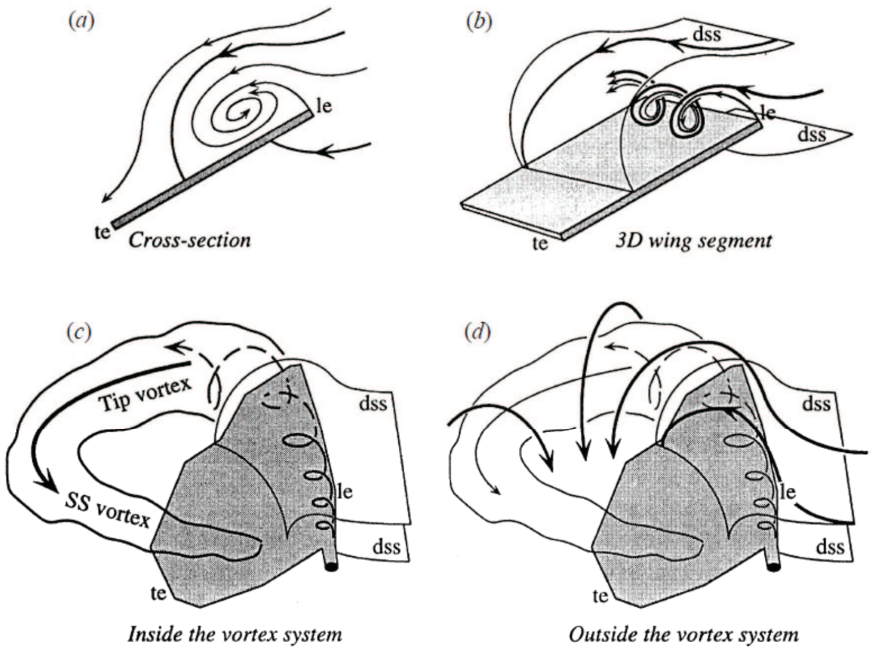


Fig. 1.7: Flow structures around a flapping wing at insect scale: "dss" refers to dividing stream surface, "le" designates leading edge, "te" trailing edge, and "SS vortex" refers to the combined starting/stopping vortex. Spanwise flow is believed to keep the leading edge vortex (LEV) attached over the span of a flapping wing for several chord lengths. From Van den Berg & Ellington (1997) [37]

investment, generating an intuition for these aerodynamic phenomena is difficult enough that future researchers will undoubtedly be discussing the effects due to individual parameters variation for many years to come.

Recently, sensing and control qualities have begun to attract more focus from biologists interested in their agility and robustness in the face of environmental disturbances. Insects display an impressive performance considering their small neurological capacity. Engineers looking to extend the capabilities of MAVs that suffer from similar SWaP constraints are taking notice of promise of robust and agile performance as they develop platforms at increasingly smaller scales. Vision, in particular, is a promising sensing modality that is currently underutilized, and could replace or augment IMU sensors.

1.1.4 Flapping Wing Dynamical Modeling

Understanding the dynamics of an aircraft is integral to assessing its flying qualities and to designing sensing and control strategies. The dynamics of a vehicle, derived from Newton's second law, determine the effect of outside forcing, via control or disturbances, on the vehicle motion. By modeling the underlying physics, we can design control inputs to reject environmental disturbances and select sensors that are customized to vehicle motion. A dynamical model suggests natural modes of motion that the vehicle will be more likely to move. These directions in vehicle state may be more susceptible to wind gusts, and so control actuation can be designed with this in mind. A full flight dynamical model is especially useful in designing

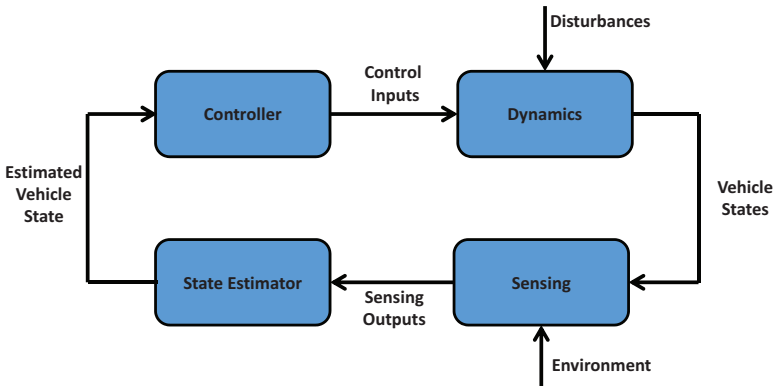


Fig. 1.8: Typical feedback loop structure. Control inputs and environmental disturbances are input to the system dynamics, onboard sensors detect the resulting vehicle motion, and sensing data is used to estimate that motion for use in future control inputs. Understanding the dynamics of the system will inform design and analysis of vehicle sensing and control.

closed loop control schemes to stabilize a naturally unstable platform, or to provide autonomous control. Multivariable control design techniques (e.g. LQR, H_∞) require a dynamical model. Additionally, sensing requirements can be customized for better sensitivity these modal directions.

Insect's sensory structure has been shown to extract motion from non-orthogonal measurement axes, as opposed to the engineering standard of roll, pitch, and yaw motion (see Fig. 1.9). [42] Biologists have proposed that the sensing structures may be aligned instead with the most important insect motions required for flight. [43] Dynamic estimates suggest that this may be the case, as *Dipteran* insects have means via ocelli (simple eyes that detect rate changes) and halteres (under-developed hind wings also used for rate sensing) to detect the most pertinent dynamical features at

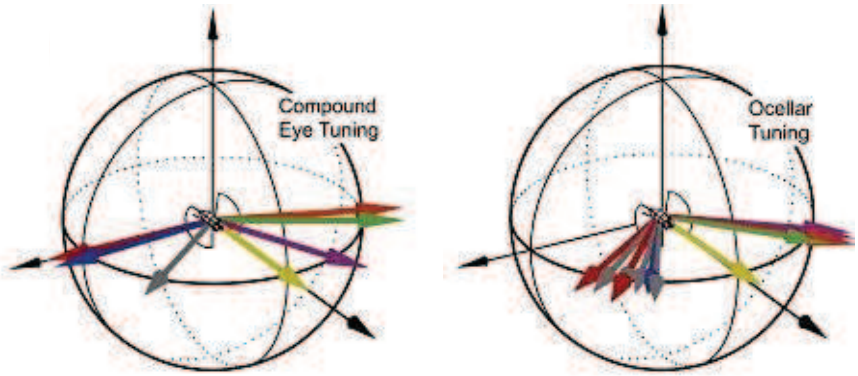


Fig. 1.9: Preferred sensing axes of the compound eyes (left) and ocelli (right) of a blowfly. From Parsons et al. (2010) [42]

high bandwidth. [44, 45] Better dynamical models for flapping wing flight will give a concept for how and why birds and insects apply sensing and control techniques, as well as give inspiration to engineers hoping to apply these effective schemes to flapping wing MAVs.

Flapping wing flight is complete with a myriad of complexities that impede flight dynamical modeling. Even capturing and tracking the motion of insects is a difficult challenge, as insects are difficult to control and tethering them leads to unrealistic kinematic measurements. Additionally, flapping wing vehicles operate at multiple time scales; vehicle dynamics and flight path modulation occur at a much slower speed than the loads generated by the wing motion. Similar to rotorcraft, aerodynamic forcing from the flapping wings is not constant throughout the wingstroke. Unique to flapping flight, however, is the stroke reversal: as the wing must stop motion after half a wingstroke and return back on the other half stroke.

Perhaps most challenging is the highly unsteady and viscous aerodynamics

around a flapping wing. The LEV generated during flapping motion can collapse or detach from the wing at different times of the wingstroke depending on the vehicle scale. Tip vortices are also much larger and dominant at these smaller scales and for these lower aspect ratio wings. The vortical structures are then shed into the wake and re-encountered by the wing on the following half-stroke. [30] Independently, these interactions are difficult to understand, but on a flapping wing they operate in tandem and interact. The LEV spirals into the tip vortex, shedding from the wing depending on Reynolds number, kinematics, and wing planform. How the wing then interacts with the shed vorticity from previous half-strokes contains the same variability.

In addition to the modeling of dynamical equations, the most effective means to control these systems remains an open question. It is not clear which kinematic motions are used by insects in flight to modulate their flight path, nor which would be most valuable for a flapping wing MAV. Unlike man-made aircraft, where designs over the past decades have coalesced on a few preferred means of actuation, insects do not have clearly defined control inputs –there are no rudder, elevators, ailerons, etc. on a fly.

1.2 Previous Modeling of Flapping Wing Vehicle Dynamics

1.2.1 Bare-Airframe Dynamical Modeling

Recent investigations of insect flight dynamics have provided quantitative understanding of underlying flapping wing flight characteristics. Identification of an insects bare-airframe dynamics allows researchers to better understand the sensing and neural pathways necessary to stabilize and control insect flight. Taylor & Thomas (2003) were the first to utilize linear dynamical modeling in empirically describing desert locust in forward flight. [46] Researchers have since used experimentation [47,48], computational fluid dynamics [49–52], and frequency-based methods [45] to identify the rigid body dynamics of a variety of insects at both hover and forward flight.

Reduced-order Aerodynamic Modeling

Each of the above dynamical models required a selection of a methodology to estimate aerodynamic loads on the flapping wing system. For several, a computational solver was used to solve the Navier-Stoke equations, and others developed an experimental apparatus that measured loads on Reynolds number-scaled flapping wings in mineral oil. These methods are expensive, both in money and time, and are not currently an option for frequency-based system identification such as those used by Faruque & Humbert (2010) that require multiple flight simulations with varying control inputs. That work required a reduced-order aerodynamic method

to estimate the flapping wing loads.

The highly unsteady and viscous flow around flapping wings is inherently difficult to model. Unsteady flow structures – particularly the leading edge vortex – are critical to aerodynamic load generation at the insect scale. [36] A reduced order aerodynamic model that results in an accurate estimation of vehicle dynamics is extremely desirable; accurate low Reynolds number computational fluid dynamic solvers for flapping wings are computationally expensive, and Reynolds number scaled experimental setups are extremely expensive and time consuming to create.

Ellington (1984) demonstrated that unsteady mechanisms were necessary to explain the generation of vertical forces necessary to keep insects aloft. [53] A purely quasi-steady method of aerodynamic estimate would not provide the necessary lift. The Robofly experimental apparatus (see Figure 1.10) was used by Dickinson in 1999 to augment the quasi-steady aerodynamic model discussed earlier by Ellington and include unsteady effects. [54, 55] By constructing lift and drag polars from a rotating wing while the LEV was attached, this experimentally-derived quasi-steady model includes additional lift and drag associated with the LEV. Adding terms for wing rotation during pronation and supination, Sane & Dickinson (2002) were able to model the lift for a *Drosophila* in hover and test the effect of varying several kinematic parameters. [56]

Other, more mathematical approaches have been developed to capture the effect of unsteady flows on flapping wings. Instead of an empirical quasi-steady estimate of the lift and drag on the entire wing as derived by Dickinson and his team,

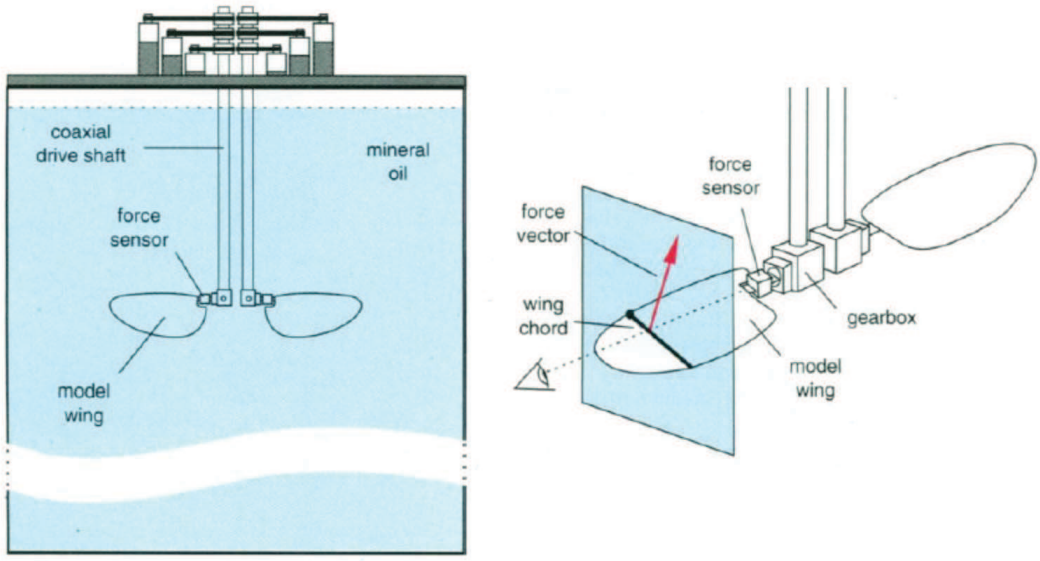


Fig. 1.10: The Robofly experimental test apparatus. [54]

these methods begin with a blade element approach. The wing is divided into many spanwise elements and the aerodynamic loads are the sum of the individual loads on each element. Such a formulation would rely on the extensive work of aerodynamicists throughout the 20th Century that developed quasi-steady aerodynamic models from thin airfoil theory. Wagner, Theodorsen, and others gave 2D analytical models for harmonically oscillated airfoils in inviscid flows; however these were limited to specific environmental perturbations of the airfoil from the steady state condition. [57–59] This limits utility in the case of flapping wings, where the wing undergoes large changes in velocity and angle of attack throughout even an ideal wingstroke.

A more suitable blade element construction is that of an indicial response, where a set of aerodynamic flows are superimposed to create an appropriate solu-

tion to a set of aerodynamic states. The superposition is determined by a set of indicial responses calculated either computationally or experimentally. [60, 61] This methodology has focused exclusively on rotorcraft research until recently. Taha et al. (2014) used superposition of quasi-steady circulation around each blade element instead of angle of attack and blade speed to calculate lift for each element. [62] This new quasi-steady method for estimating flapping wing flight promises for a more precise estimate of the lifting loads especially during wing rotation at the end of each half-stroke. In the current work, the empirically-derived quasi-steady model of Dickinson et al. is utilized for its simplicity and to validate the previous work of Faruque & Humbert.

Stroke Averaging

The flapping wings generate periodic forcing with each wingstroke that determines the vehicles motion. Vehicle motion from unsteady forcing can be broken into two components, high frequency vibrations and the low frequency flight path. The objective when identifying vehicle dynamics is an accurate estimation of the flight path, and higher frequency content can be neglected for tractability. Vehicle inertia limits the speed of a vehicle's response to any periodic aerodynamic forcing, resulting in a low frequency flight path from an averaged high frequency forcing. [63] Previous work on insect flight has shown that the assumption does weakens for smaller systems that have fast dynamics with slower wingbeat frequencies. [64] Vehicle motion can be separated from within wingstroke motion by averaging the aerodynamic

loading on the vehicle during the wingstroke.

This stroke-averaging assumption (sometimes referred to as 'two-timing') is necessary to attain time-invariance of the stability and control matrices in the common form of the linear dynamical equations: $\dot{\mathbf{x}} = A\mathbf{x} + B\mathbf{u}$, where $\mathbf{x}$ is the vector of vehicle states, $\mathbf{u}$ is the vector of vehicle control inputs, A is the stability matrix, and B is the control matrix. The purpose of any linear system modeling technique is to identify the stability and control matrices that describe vehicle motion in response to changes in state or control input. This formulation enables use of powerful linear time invariant (LTI) analysis and control techniques.

Linear Dynamical Models

A variety of insect dynamical models have been given by Sun and colleagues, including a hoverfly, cranefly dronefly, bumblebee, and hawkmoth, using a Navier-Stokes computational solver to measure changes in loads due to perturbations away from hover and forward flight. [49–51,65,66] These works have described a longitudinal system dominated by unstable pitching and surging (fore-aft) oscillatory motion. In hover, heave (vertical) motion is uncoupled and stable, while in forward flight, heave is coupled to the unstable pitching and surging. Longitudinal instability is caused by a large pitching moment caused by fore-aft motion. The static stability created by increased drag on the system due to such motion does not provide enough damping to mitigate this effect.

The time for a disturbance to double is about 100 ms for larger insects like the

bumblebee and hawkmoth; the doubling time for smaller insects in these studies is closer to 50 ms. These estimates suggest the biological sensing necessary to stabilize such motion must operate at a fraction of the latency. Visual feedback is unlikely – vision to motor delays are between 30-40 ms. [67,68] Halteres (underdeveloped hind wings on Dipteran insects) appear well-suited to provide the equivalent of a high bandwidth rate gyro. [69, 70] Halteres have been shown to operate with a delay of about 3 ms, adequate for the instabilities discovered by Sun's team. [71]

These results in longitudinal flight have been repeated by Faruque & Humbert using a frequency-based method and quasi-steady aerodynamics for a hovering *Drosophila* (fruitfly). [45] Faruque & Humbert's model *Drosophila* is again dominated by a large pitching moment due to fore-aft motion, yielding an instability that must be accounted for by some feedback mechanism in their non-linear model. Simple pitch-rate feedback to a control term that defines the average wing position was shown to adequately stabilize the longitudinal motion.

While there has been general agreement about longitudinal flight between these two models, the same is not true for lateral-directional flight. For longitudinal flight especially, the modal structure of the linear dynamical system is agreed upon. Sun and colleagues suggest that the lateral-directional system is also unstable and dominated by coupled rolling and sideslip motion, along with an uncoupled stable yawing subsidence. [51] Faruque & Humbert's work yields a marginally stable system, with an oscillatory roll and sideslip motion. The stable yawing motion is similar to that of Sun's team. [72] The difference between the models is largely in

the roll moment due to sideslip motion – this is large and positive in Sun's work, but is negative in Faruque & Humbert's model. Because the models are of different insects with different kinematics, it is not immediately apparent that either of these models is incorrect.

1.2.2 Modeling Flapping Wing Control

An insect's maneuverability and responsiveness to environmental disturbances depend on the effectiveness of wing kinematic inputs to impart aerodynamic loads on the dynamical system. Identification of baseline flapping wing kinematic trajectories is currently an active field of research that has been explored from multiple perspectives: lift optimization, power optimization, and high speed videography of freely-flying insects. [48, 73, 74] Using Robofly, Sane & Dickinson (2001) estimated kinematics required to give enough lift: including the angle of attack, and the phasing of pronation and supination in the wingstroke. [75] Berman & Wang utilized a quasi-steady aerodynamic method to calculate the most energy-efficient hovering flight for the fruit fly, bumble bee, and hawkmoth. [73] Identification of effective flapping wing kinematic control inputs away from these baseline trajectories is integral to determining the insect's agility.

Several previous works have modeled the impact of control inputs via deviations of the wing kinematics from the baseline. Lehmann & Dickinson (1998) empirically investigated how several species of *Drosophila* vary stroke amplitude and frequency to control vertical motion. [74] Zhang & Sun (2011) identified the

linear contribution of several chosen control inputs to load generation using computational fluid dynamics (CFD) to calculate the unsteady aerodynamic loads on the wings [65] Using the quasi-steady aerodynamic model and frequency-based system identification techniques, Faruque & Humbert (2010) estimated the contribution of select control inputs. [45, 72]

Control input identification gives intuition for how these specific control inputs (usually flapping frequency, amplitude, stroke plane tilt, and fore-aft stroke plane offset) directly effect aerodynamic loading on the insect and provide the opportunity to utilize linear time invariant (LTI) control tools to address insect control strategy. Similar to static stability tests, they explain little of how each input effects the bare-airframe dynamics. It is more difficult to compare the effectiveness of individual kinematic inputs for the ability to generate insect motion. Humbert and Faruque (2011) presented a methodology quantifying the control authority of kinematic control inputs by calculating the complete set of reachable states for combinations of inputs. [76]

1.3 Dissertation Objectives and Approach

1.3.1 Objectives

The perturbation-based models of Sun and colleagues cannot be directly compared to the system identification work of Faruque & Humbert. The *Drosophila* modeled by Faruque & Humbert is not included in the variety of insect systems

modeled by the former group. Even if it were, a direct comparison and verification would require the kinematics and flight condition (e.g. forward flight or hover) to be replicated as well. Such a comparison is necessary to ensure that each model is correct, and more importantly that the methodology is applicable to dynamical modeling of flapping wing systems.

The accuracy of system modeling based on the reduced-order aerodynamic methods such as that of Faruque & Humbert is of particular importance. A quasi-steady aerodynamic solver can yield dynamical models at a fraction of the cost of experimental or computational modeling techniques. This will give freedom to future designers of flapping wing systems for a first-run dynamical estimate, or to resource-constrained biologists hoping to understand insect and avian sensing and control. Quasi-steady aerodynamic methods allow simulation of a flapping wing system for more than a few wingstrokes, a requirement for frequency-based system identification like that of Faruque & Humbert, or for large scale studies of wing kinematic changes.

The assumption of time invariance for smaller vehicles with fast wingstrokes also remains in question. Wu & Sun (2012) demonstrated the limits of the assumption for two model insects (dronefly and hawkmoth), discovering the split-timing modeling technique introduces little variance in the results. [64] Thus, it is not clear where the assumption may break down, and whether a time-invariant model will be useful at the hummingbird scale, where we may expect the first flapping wing MAVs. If applicable, a time invariant system would be much simpler for the design

of on-board model-based control systems.

When previous work has included control inputs in the dynamical model, those inputs were selected *a priori*. A method to construct optimal wing kinematic inputs from a general set are required. It is vital that such a selection accounts for the inherent dynamics of vehicle motion, and not simply maximize generation of aerodynamic loads. Gramian-based metrics proposed by Humbert & Faruque offer a measure of wing kinematic control input effectiveness on the basis of reachability and disturbance rejection. [76] A system's reachability describes the amount of control over the system's state for a specific control input. Maximizing reachability is analogous to improving maneuverability, while disturbance sensitivity describes susceptibility to wind gusts. These gramian-based metrics allow integration of bare-airframe dynamics in the selection of effective control inputs. Instead of selecting control inputs by direct aerodynamic load, consideration can be given to the combination of the direct load and the dynamic motion it imparts.

The present work is motivated by the requirement of a tractable model that accounts for the above complications in flapping wing flight. The goal of this work is to provide a basis for reduced-order modeling of flapping wing dynamical systems by investigating the following:

1. Reduced-order aerodynamic methods for estimating flapping wing dynamics are compared to more rigorous computational and experimental models. The resulting dynamical model derived from experimentally-derived quasi-steady aerodynamic estimate is compared to computational and experimental models

based on identical systems with the same wing kinematics.

2. Time-variance assumptions are tested using periodic time modeling techniques and comparing with time-invariant models. Analysis is performed at insect scale, where aerodynamic forcing from wing flapping is much faster than the rigid body motion, and at avian scale where the forcing is at a similar frequency to vehicle motion.

3. A control-theoretic methodology is presented that selects flapping wing control inputs from a general set. Reachability and disturbance gramians are utilized as metrics to optimize kinematic control inputs for bare-airframe agility and disturbance rejection. The result is a set of wing kinematic inputs that are tuned to the specific dynamics of an individual vehicle.

1.3.2 Dissertation Organization

The organization of this dissertation is as follows. Chapter 2 provides a basis for describing the motion of insect flight, and presents a high-speed camera setup for capturing insect kinematic motion. Frequency-matched transcendental functions are used to extract wing motion from captured data sets of forward-flying *Drosophila*, providing reference wing kinematics for two forward flight conditions. A set of idealized hovering kinematics with flat stroke plane is also defined, along with a set of biologically-motivated wing kinematic control inputs.

Chapter 3 describes several methods of measuring aerodynamic loading on the

flapping wing throughout the wingstroke. An experimentally-derived quasi-steady routine is cost-effective, but unproven in providing accurate estimates of all unsteady loads throughout a wingstroke. The IBINS incompressible flow solver models the wing and body as a set of immersed boundaries in a Cartesian mesh. RoboFly provides verification of the computational model using a dynamically scaled-up version of a *Drosophila* wing capable of a variety of wing and body motions. Results of the three aerodynamic methods are verified using an example forward flight *Drosophila* wingstroke. Aerodynamic power requirements are combined with inertial power to provide a total power estimate for biological flapping wing flight.

Chapter 4 describes linear modeling of the homogeneous *Drosophila* dynamics. Small perturbation theory linearizes the non-linear dynamics of the flapping wing system. The stroke-averaging assumption is described, where the high frequency dynamical forcing from flapping wing aerodynamic loads is discarded. Linear time invariant dynamical models resulting from each of the aerodynamic calculations are compared for the flight conditions described in Chapter 2. The stroke averaging assumption is tested using Floquet decomposition to estimate the linear time periodic model for forward flying *Drosophila* . A model-based control developed with the forward flight time-invariant dynamics is tested on the time-periodic model.

Chapter 5 focuses on the modeling of flapping wing kinematic control inputs. Small perturbation theory is again used to generate linear time invariant approximations to the effect of each control input. The biologically-motivated control inputs are evaluated according to a reachability metric, which is augmented

to include power requirements to enact the motion. A novel method of generating energy-optimal wing kinematic inputs is provided and applied to the forward-flying *Drosophila* model.

Chapter 6 apples the modeling concepts of previous chapters to a hummingbird-scale micro air vehicle. Longitudinal linear dynamics are estimated according to small perturbation theory and compared to the much smaller *Drosophila* . Multiple kinematic control inputs are evaluated according to the reachability metric, providing intuition for more effective vehicle control design. The time-invariant assumption is tested for the vehicle model in both open and closed loop.

Chapter 2: Flapping Wing Kinematics

2.1 Coordinates Definition

Unlike most birds[1] that flap their wings primarily up and down to gain thrust, *Dipteran* insects fly with a wingstroke primarily in a back and forth motion. The wing's leading edge remains constant throughout the stroke, but the upper surface on the downstroke will become the lower surface on the upstroke. This motion generates a force to counter gravity during both the downstroke and upstroke, giving the ability to fly at slow speeds, and for some species, even hover. The wing motion as viewed from the side is typically a flattened figure-8 shape rotated onto the horizontal. Often this figure-8 has some curvature, bent up at the end of each half-stroke. Figure 2.1 shows typical insect flapping motion in the form of a "dot-and-stick" diagram; "dot"s show the leading edge of the wing and the "stick" protuding below shows the wing pitch.

The purpose of this chapter is to define wing motion for a variety of flight conditions. In order to describe the motion precisely throughout the stroke, some definitions of coordinate systems are necessary. Throughout this work, the body

[1] Hummingbirds are notably the only bird species to fly with similar kinematics to insects.

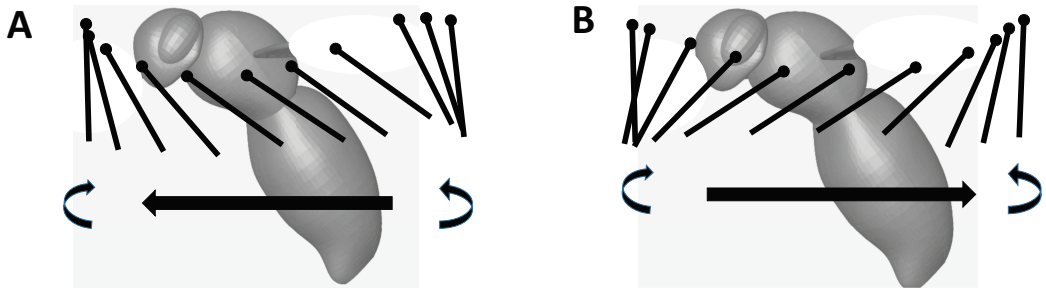


Fig. 2.1: Insect flapping motion is horizontal. The downstroke (A) is followed by pitching of the wing up (pronation) that rotates the leading edge of the wing to prepare for the upstroke. The upstroke (B) is then followed by another pitching rotation back (supination) so the leading edge is again forward for the downstroke. This motion features lift generation during both half-strokes.

frame of an insect or flapping wing vehicle will be defined as a set of coordinates at the center of gravity, with the x-axis forward, the y-axis out to the right side, and the z-axis down. Note that the insect body will typically be pitched up during flight. Figure 2.2 shows the body coordinates $\hat{\mathbf{e}}$ on an insect together with the right wing coordinates $\hat{\mathbf{p}}$.

The wing coordinates system is located at the wing hinge, and is aligned with the body coordinates when the wing is flat and level out to the side, but as the wing moves, the wing coordinates will rotate with the wing. Thus the y-axis ($\hat{p}_2$) will always remain along the span of the wing and x-axis ($\hat{p}_1$) will always point away from the leading edge of the wing and align with the chord; meanwhile, the z-axis ($\hat{p}_3$) will point down during the downstroke and up during the upstroke.

A set of three angles determines the position of the wing at any instant in

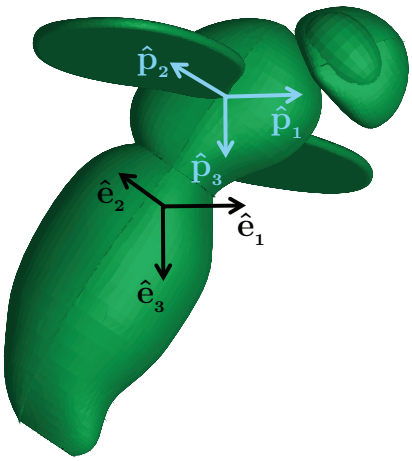


Fig. 2.2: The body and wing coordinate systems. The body coordinate system $\hat{\mathbf{e}}$ is fixed to the rigid insect body at the center of mass, with $\hat{e}_1$ pointing in the direction of forward flight, $\hat{p}_2$ pointing to the insect's right, and $\hat{p}_3$ down. The wing coordinate system $\hat{\mathbf{p}}$ remains fixed to the wing root, and rotates with the wing. Thus, $\hat{p}_1$ always passes through the chord of the wing away from the leading edge, $\hat{p}_2$ remains along the span of the wing, but $\hat{p}_3$ will be on the lower surface during downstroke and upper surface during the upstroke.

time. These wing Euler angles are flapping angle ($\phi(t)$), elevation angle ($\zeta(t)$), and pitch angle ($\alpha(t)$). As shown in Figure 2.3, a 3-1-2 order of rotation is used to give the current wing position; the wing is rotated first around $\hat{p}_3$ by flapping angle, then around $\hat{p}_1$ (that has already moved due to the previous rotation) by elevation angle, and finally pitched around $\hat{p}_1$ (after it has been moved due to both earlier rotations).

The rotation from the wing to body coordinates can be written using a combination of rotation matrices, as shown in Eq. 2.2. The rotation matrix T_{bw} transforms

vectors from the wing to the body frame, such that $[\mathbf{x}]_b = T_{bw}(\phi, \zeta, \alpha)\,[\mathbf{x}]_w$, where $\mathbf{x}$ is a vector, $[\cdot]_b$ denotes the body frame, and $[\cdot]_w$ denotes the wing frame.

$$T_{bw}(\phi, \zeta, \alpha) = T_2(\alpha)T_1(\zeta)T_3(\phi) \tag{2.1}$$

$$= \begin{bmatrix} \cos(\alpha) & 0 & -\sin(\alpha) \\ 0 & 1 & 0 \\ \sin(\alpha) & 0 & \cos(\alpha) \end{bmatrix} \begin{bmatrix} 1 & 0 & 0 \\ 0 & \cos(\zeta) & \sin(\zeta) \\ 0 & -\sin(\zeta) & \cos(\zeta) \end{bmatrix} \begin{bmatrix} \cos(\phi) & \sin(\phi) & 0 \\ -\sin(\phi) & \cos(\phi) & 0 \\ 0 & 0 & 1 \end{bmatrix} \tag{2.2}$$

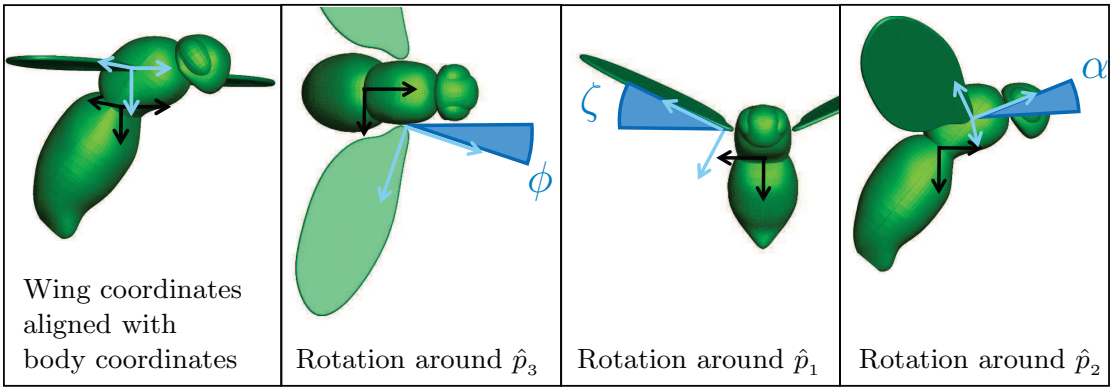


Fig. 2.3: The definition of wing kinematic angles is dependent on the order of the rotation, in this case, a 3-1-2 rotation. When all wing kinematic angles are 0, the wings lie flat to either side with the wing coordinate frame ($\hat{\mathbf{p}}$) aligned with the body frame ($\hat{\mathbf{e}}$). The first rotation about $\hat{p}_3$ is the flap angle ϕ. The second rotation about $\hat{p}_1$ occurs after the first rotation, by the elevation angle ζ. The final rotation about $\hat{p}_2$ by the wing pitch angle α, occurs after both the ϕ and ζ rotations.

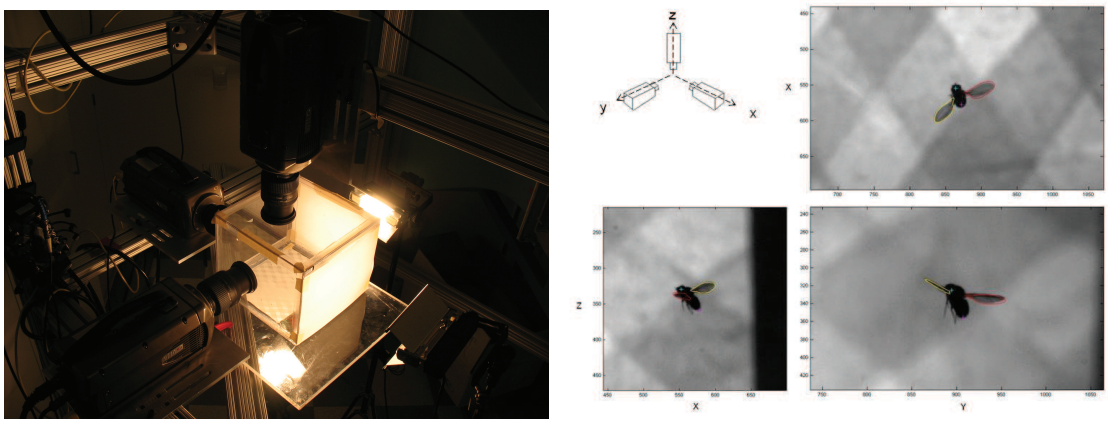


Fig. 2.4: The insect motion capture setup. A snapshot of a *Drosophila* in the flight chamber as photographed by the orthogonal camera setup. Digitization includes marking the head, tail, wing root, and wing tip, and fitting a wireframe over each wing.

2.2 Flight Capture and Kinematics Extraction

2.2.1 Flight Capture Apparatus

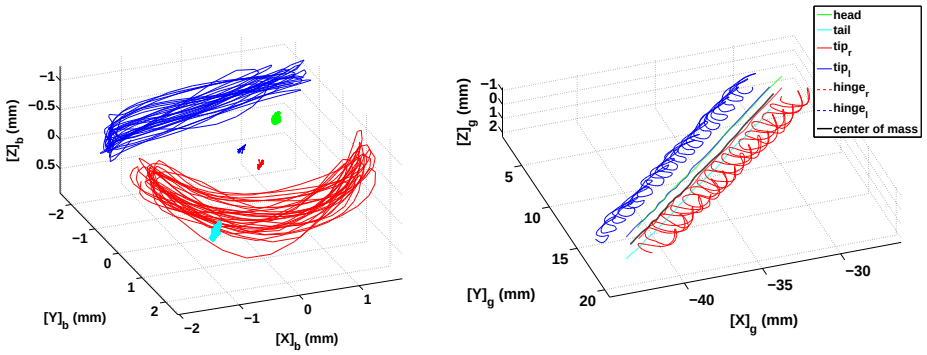
Cultures of *Drosophila Melanogaster* are released into a custom 10x10x8 inch acrylic test chamber, and filmed with three orthogonal high-speed (7500 fps) digital video cameras (Vision Research Phantom v710; 24-85 mm f2.8-f4 Nikkor Nikon Zoom lenses) aligned 6 inches away from a common reference point in the center of the test chamber, as shown in Fig. 2.4. While filming, the chamber is back-lit with 3 Lowel V-lights, diffusing the high intensity light with translucent paper. An exposure of 40 μs was chosen at a resolution of 1280x800 pixels. Due to the short flight times of the *Drosophila Melanogaster* relative to human reaction time,

capturing insects in the focal region of all three cameras required an automatic-trigger system. The cameras were synced to within 1 μs, or about 0.02% of a typical *Drosophila* wingstroke. A manual digitization to extract the body and wing kinematics is performed using a modified version of Dr. Ty Hedrick's freely available MATLAB software [77]. The location of the head, tail, wing hinges, and wing tips are digitized in each frame, and these points are used to extract all three body angles and each wing's stroke amplitude and elevation angles. A wire-frame of the wing is inserted and rotated to fit the wing in each frame to extract the wing's pitch angle.

2.2.2 Insect Forward Flight Kinematics Extraction

From the dozens of captured flight trials, two were selected that were closest to straight and level flight. These two trials provided reference wing kinematics for two reference flight conditions, one in slow forward flight and one in fast forward flight. A mean value from the kinematics extraction of each flight trial is used for both the body pitch and forward flight speed, whereas body sideslip, climb, roll, and yaw were rounded down to zero. Body kinematics are considered constant for the purposes of establishing a forward flight reference condition.

Wing kinematics are described by a set of three periodic functions that determine the position of the wing at any point in time according to the 3-1-2 rotation described in Figure 2.3. Fitted frequency-matched functions of the digitized estimates for the three wing angles were found using an ensemble averaging of curve fit parameters. Curve fits of stroke angles, $\phi_{r,l}$ (where $[\cdot]_{r,l}$ denotes the right and left



(a) (b)

Fig. 2.5: Digitization of free flight insect motion used for the forward flight reference condition (a) in the body frame, where the kinematics can be seen to be relatively constant, and (b) in the global frame, where the steady forward flight motion can be seen.

wings, respectively) can be expressed by a single sinusoid, while wing pitch angles, $\alpha_{r,l}$, and elevation angles, $\zeta_{r,l}$, are a sum of two harmonics of the stroke angle. These are frequency matched so that all terms in $\zeta(t)$ and $\alpha(t)$ have the same frequency of $\phi(t)$, or a multiple of it. It was found that $\zeta_{\omega 1}$ and $\alpha_{\omega 1}$ were equal to 1, while $\zeta_{\omega 2} = 2$ and $\zeta_{\omega 1} = 3$ for both flight conditions studied here.

$$\phi(t) = \phi_{\mathrm{m}} sin(\omega t) + \phi_o \tag{2.3}$$

$$\zeta(t) = \zeta_{\mathrm{m1}} sin(\zeta_{\omega 1}\omega t + \zeta_{\mathrm{p1}}) + \zeta_{\mathrm{m2}} sin(\zeta_{\omega 1}\omega t + \zeta_{\mathrm{p2}}) + \zeta_o \tag{2.4}$$

$$\alpha(t) = \alpha_{\mathrm{m1}} sin(\alpha_{\omega 1}\omega t + \alpha_{\mathrm{p1}}) + \alpha_{\mathrm{m2}} sin(\alpha_{\omega 1}\omega t + \alpha_{\mathrm{p2}}) + \alpha_o \tag{2.5}$$

The right wing kinematic parameters for both flight conditions are given in Table 2.1, and The right wing kinematics for each reference condition are shown in Figures 2.6

& 2.7. The left wing has identical kinematics, but with a sign change for ϕ_l and ζ_l.

	FF1				FF2		
u_0	7.07 cm/s			u_0	32.0 cm/s		
f	$233Hz$			f	$200Hz$		
ϕ_m	-66.4			ϕ_m	-50.2		
ϕ_o	16.8			ϕ_o	24.9		
θ_{m1}	5.2	θ_{m2}	8.3	θ_{m1}	5.3	θ_{m2}	6.2
$\theta_{\omega 1}$	1	$\theta_{\omega 2}$	2	$\theta_{\omega 1}$	1	$\theta_{\omega 2}$	2
θ_{p1}	234.9	θ_{p2}	53.0	θ_{p1}	52.7	θ_{p2}	213
θ_o	-7.62			θ_o	-2.66		
α_{m1}	58.7	α_{m2}	15.0	α_{m1}	59.8	α_{m2}	16.0
$\alpha_{\omega 1}$	1	$\alpha_{\omega 2}$	3	$\alpha_{\omega 1}$	1	$\alpha_{\omega 2}$	3
α_{p1}	271.4	α_{p2}	72.6	α_{p1}	-9.16	α_{p2}	293.3
α_o	87.0			α_o	94.5		

Tab. 2.1: Kinematic parameters identified for freely-flying *Drosophila* in slow forward flight (FF1) and fast forward flight (FF2). (All angles are in degrees.)

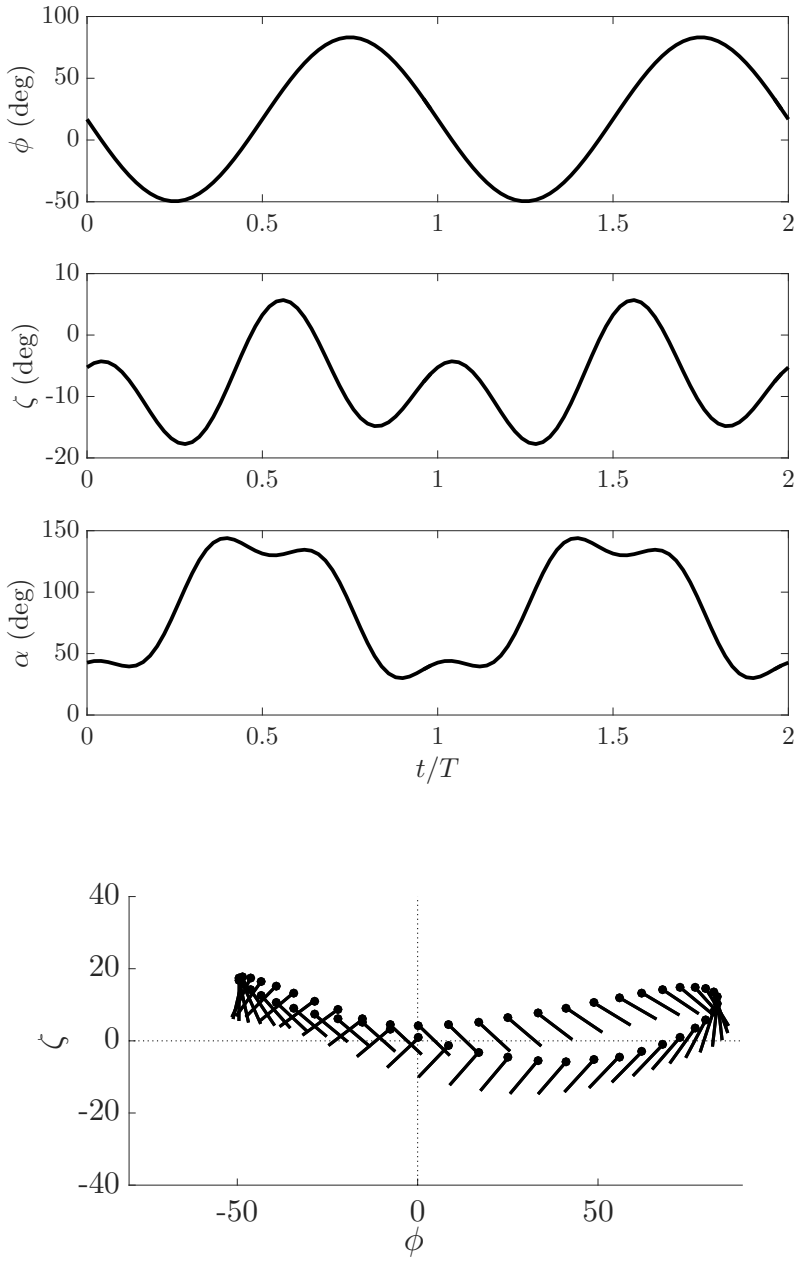


Fig. 2.6: Captured wing kinematics (above) from slow forward flying *Drosophila Melanogaster*. Phase portraits (below) show the leading edge of the wingtip as a dot, with a protruding stick to show wing pitch.

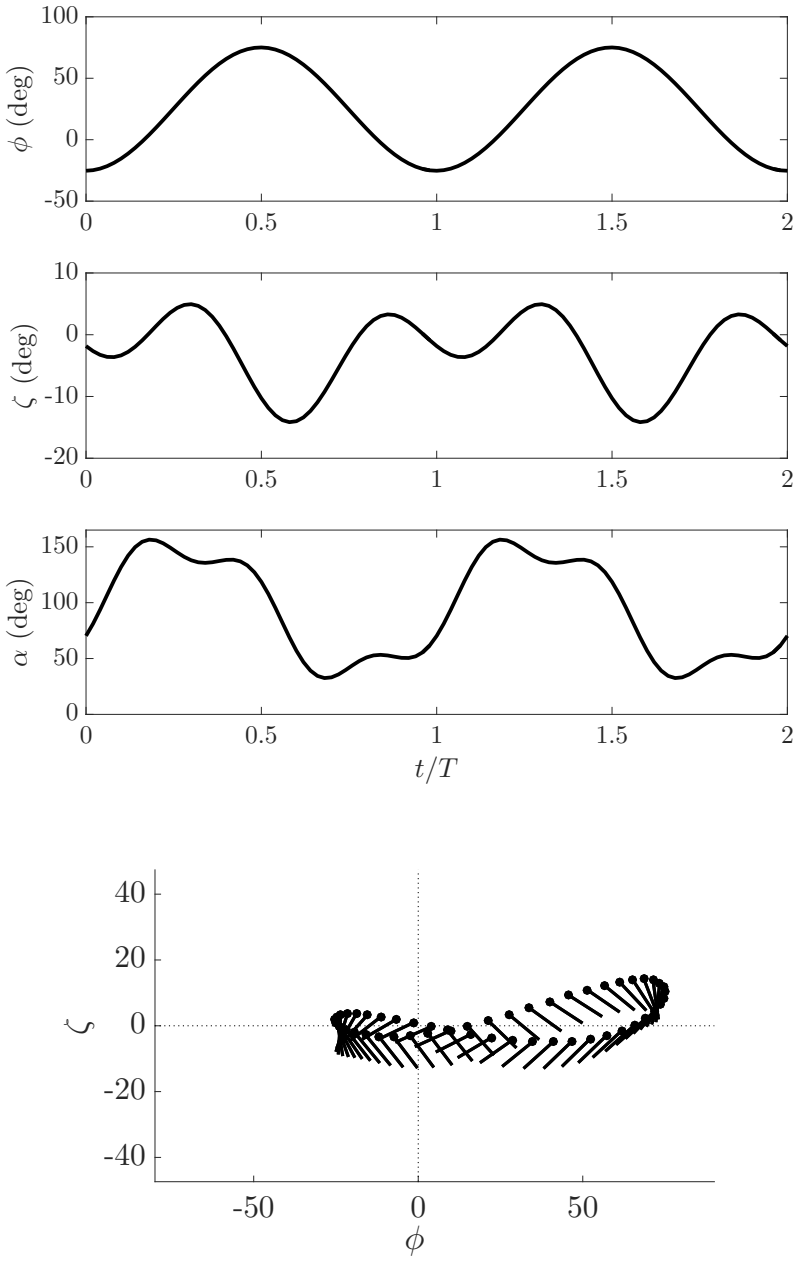


Fig. 2.7: Captured wing kinematics (above) from fast forward flying *Drosophila Melanogaster*. Phase portraits (below) show the leading edge of the wingtip as a dot, with a protruding stick to show wing pitch.

2.3 Idealized Insect Kinematics

2.3.1 Hover Kinematics

In addition to the experimentally extracted kinematics from freely-flying insects discussed above, this work will also present an idealized set of kinematics used by Faruque et al. (2010) in order to present a comparison to those results. [45, 72] These idealized kinematics are simpler, with a flat stroke plane and in hover, giving the opportunity to examine a simpler set of dynamics as a benchmark before the more complicated kinematics used by an actual insect in free flight. The flapping angle is given by a sine wave, while the elevation angle is held to zero, and the pitch angle is a square wave.

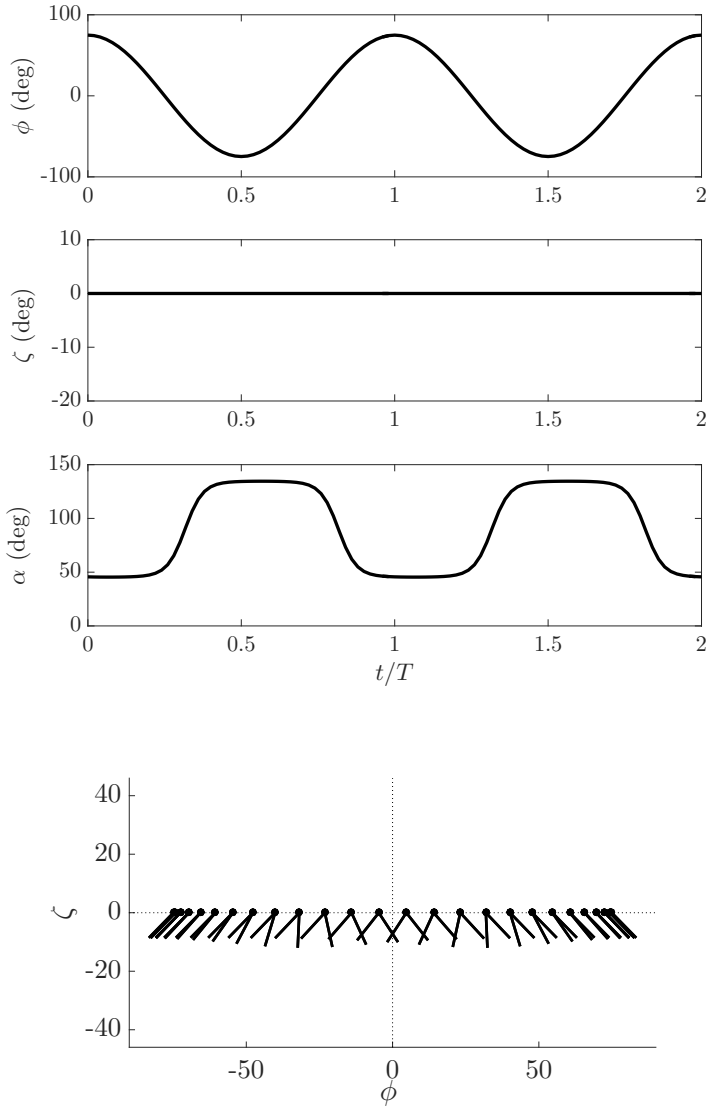


Fig. 2.8: Flat wingstroke kinematics for an idealized hovering insect. Wing kinematic angles (above) show a simple sine wave for the flapping angle and a square wave for the angle of attack. A dot-and-stick diagram in a phase portrait (below) provides more intuition for wing kinematics. Note the wing rotation is advanced – it pronates and supinates well before wing reversal.

2.3.2 Biologically-Motivated Control Inputs

Throughout this work, biologically-inspired wing kinematic control inputs are utilized to give control to a platform. These are shown in Figure 2.9 amplitude ($\phi_{\max}$), stroke offset (ϕ_{off}), and stroke plane tilt (β). Collective changes to these inputs on both wings will affect longitudinal motion, while differential changes can give lateral-directional control. Changing amplitude gives an overall increase in forcing during the wingstroke; stroke offset changes the average location of the wing, effectively moving the center of pressure and generating a pitching moment; and stroke plane tilt is a rotation around $\hat{p}_2$ before the 3-1-2 rotations mentioned above, tilting the thrust vector. The effectiveness of each of these control inputs will be determined in later chapters.

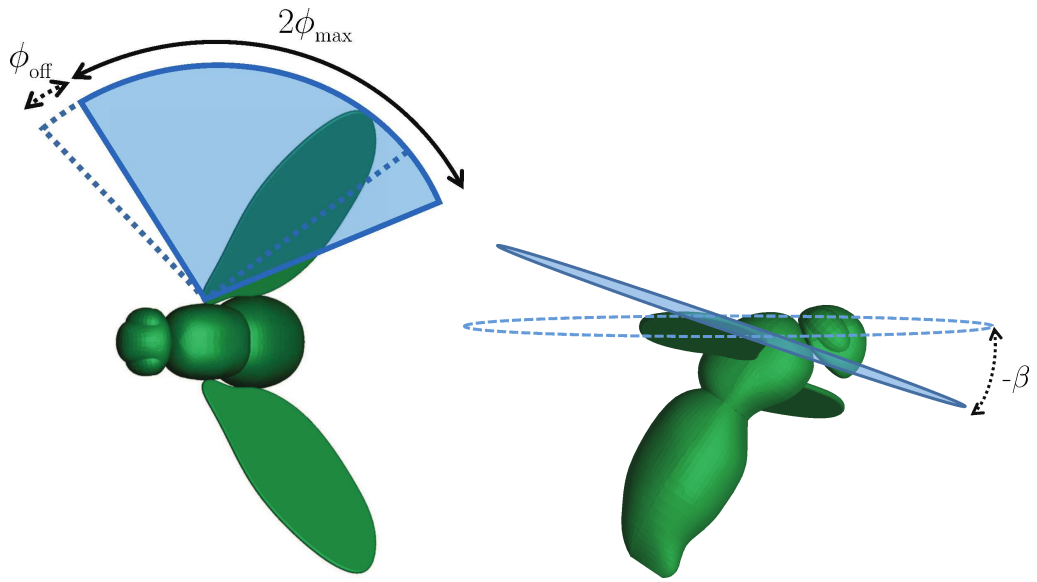


Fig. 2.9: Basic wing kinematic control inputs: stroke amplitude ϕ_{max}, stroke bias ϕ_{off}, and stroke plane tilt β. Note that due to the orientation of the wing coordinate y-axis $\hat{p}_2$, stroke plane tilt is positive when pitching the stroke plane back.

2.4 Summary

This chapter presented a framework for discussing flapping wing kinematics. A set of coordinate frames are used to define wing motion in reference to the body motion of the insect or flapping wing vehicle. Wing kinematics are described in terms of a set of three Euler angles that rotate the wing according to periodic equations. The kinematic equations for a hover reference condition are prescribed as a flat stroke plane with wing pitch modeled approximately as a square wave.

A setup for flight capture and kinematic extraction was presented whereby flight kinematics for *Drosophila* were captured for freely-flying insects. The kinematics for two forward flight reference conditions were described based on insect

wing motion in flight as seen by the high-speed camera setup. A set of biologically-motivated wing kinematic inputs were defined, including changes to stroke amplitude, stroke offset, and stroke plane tilt.

Chapter 3: Flapping Wing Aerodynamics

3.1 Motivation for Aerodynamic Modeling

Aerodynamic loads, along with gravity, are the primary forcing on the insect. Any treatment of the dynamics of insect flight must begin with an estimation of the loads exerted on the insect by the surrounding air. Both the insect scale and the inherent complexity of the fluid flow make estimation of these loads notoriously difficult.

The goal for this work is, in part, to determine the aerodynamic estimation relevant to insect dynamical modeling. A thorough treatment of the individual effect of each of the above aerodynamic phenomena is therefore outside the scope of this work. However, a reduced order aerodynamic model that results in an accurate estimation of vehicle dynamics is extremely desirable; accurate low Reynolds number computational fluid dynamic solvers for flapping wings are computationally expensive, and Reynolds number scaled experimental setups like Dickinson's RoboFly are extremely expensive and time consuming to create. Some of the more complicated aerodynamic effects of the flapping wing flow occur over short time spans relative to the vehicle dynamics. As will be discussed in Chapter 4, high frequency aerody-

namic phenomena (e.g. the quick wing rotation and wake capture during pronation and supination) may not have a dramatic effect on the overall vehicle dynamics because the associated loads occur over only a fraction of a wingstroke, while the body dynamics operate on a time frame longer than several wingstrokes. To demonstrate this, unsteady effects will be estimated with computational and experimental techniques, and compared to a quasi-steady aerodynamic model that does not include them.

3.2 Previous Insect Aerodynamic Modeling

Osborne (1951) and later Weis-Fogh (1972) first suggested a quasi-steady model for estimating the instantaneous forces acting on a flapping wing [40, 78]. Ellington (1984) further developed the concept, but contradicted Weis-Foghs suggestion that quasi-steady aerodynamics can result in the lift necessary for hovering insect flight [53]. Ellington diligently documented insect morphological and kinematic features using techniques available at the time, but with a quasi-steady aerodynamic model constructed from conventional steady state estimates of lift and drag coefficients failed to generate a feasible model that could predict the lift necessary for flight.

Dickinson et al. (1999) used experimental data to augment the quasi-steady aerodynamic model that includes unsteady effects. By constructing lift and drag polars from a rotating wing while the LEV was attached, this experimentally-derived quasi-steady model includes additional lift and drag associated with the LEV. By

adding terms for wing rotation during pronation and supination, Sane & Dickinson were able to model the lift for a *Drosophila* in hover and test the effect of varying several kinematic parameters. Drag, however, was not as accurately modeled and still suffered from inaccuracies compared to the experimental measurements from RoboFly [56].

3.3 Aerodynamic Estimation Methods

Three aerodynamic techniques were utilized to estimate the loads on a flapping wing: an experimentally-derived quasi-steady model, a computational fluid dynamic (CFD) solver, and a scaled up robotic flapping setup (RoboFly). The purpose of the CFD and RoboFly aerodynamic estimates is for verification of the less rigorous quasi-steady methodology. The aerodynamic loads are estimated by each technique.

In this work the wing is treated as a rigid planar plate with *Drosophila Melonogaster* morphology. Actual *Drosophila* wings do in fact flex, but precise measurements of flexing are quite difficult to capture in flight. The small size of these insects coupled with the high flapping speed and unpredictable movement through the focal volume of the kinematic extraction setup lead to a course resolution, such that it is difficult to capture torsion in particular with any accuracy. Moreover, wing flexing is an active area of research in both the experimental and computational methods.

Aerodynamic scaling for similitude is necessary for both CFD and RoboFly. The aerodynamics for a flapping vehicle with rigid wings can be scaled by two parameters: the Reynolds number, Re, and the reduced frequency, k [79]. The reduced

frequency scales the unsteadiness of the flow, and results from nondimensionalizing the Navier-Stokes equations with the flapping frequency. Reynolds number and reduced frequency are dependent on the mean chord length of the wing, $\bar{c} = S/2R$, and the reference velocity, $U_{ref} = 4\phi_{max} f R$, which is the average wing tip speed as specified in Refs. 55 and 80. The model *Drosophila* operates at a Reynolds number near 120, and reduced frequency 0.2.

3.3.1 Quasi-Steady

The quasi-steady aerodynamic model is derived from the Dickinson translational lift and drag force, in which the lift and drag coefficients are experimentally determined. This quasi-steady model is not the conventional aerodynamic quasi-steady model, in which lift is linearly related to wing angle of attack with slope 2π. Here, quasi-steady refers to the determination of lift and drag as functions exclusively of the instantaneous air speed seen by the wingtip, $\mathbf{U}_{\text{tip}}(t)$, and the angle of attack at the wing tip, $\alpha_{\text{tip}}(t)$. By incorporating much of the inherent unsteadiness of flapping wing aerodynamics into the non-dimensional lift and drag coefficients, a much simpler and tractable estimation of the aerodynamic loading is possible for a wide range of flapping wing kinematics.

Lift is given by Eq. (3.1), where ρ is air density, S is the surface area of the wing, and $\hat{r}_2$ is the non-dimensional second moment of wing area: $\hat{r}_2 = \int_0^1 \hat{c}\hat{r}^2 d\hat{r}$, where $\hat{c}$ and $\hat{r}$ are normalized chord and radius, respectively. The addition of the second moment of wing area into the traditional equation for an aerodynamic force

addresses the distribution of lift along the span of the wing, and allows lift along the rotating wing to be calculated solely from tip velocity and angle of attack.

$$L(t) = \frac{1}{2}\rho \|\mathbf{U}_{\text{tip}}(t)\|^2 S \hat{r}_2^2 C_L(\alpha_{\text{tip}}(t)) \tag{3.1}$$

A similar equation can be given for drag. The lift and drag coefficients were obtained experimentally by Dickinson et al. (1999) using RoboFly, and approximated by harmonic functions, as shown in Figure 3.1. These coefficients include the three dimensional effects of a rotating wing, and unsteady effects including the leading edge and tip vortex interaction. Other quasi-steady forces mentioned earlier, such as added mass or wake capture, are not included in the present calculation.

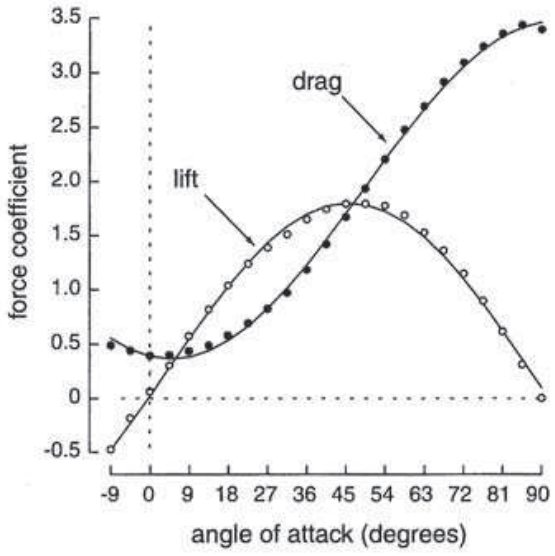


Fig. 3.1: Lift and drag coefficients versus angle of attack for a rotating *Drosophila* wing at constant angle of attack. From Dickinson et al. (1999).

Calculation of the wingtip velocity includes three terms: the first due to the rotation of the wing, another due to the translation of the insect, and finally a term

due to the insect's rotation. As shown in equation 3.2, each term must be written in the wing frame, which means including a transformation from the body frame to the wing frame for the two terms resulting from insect body motion.

$$[\mathbf{U}_{\text{tip}}(t)]_{\text{w}} = \omega_{\mathbf{w}}(t) \times [\mathbf{R}_{\text{tip}}]_{\text{w}} + [\mathbf{v}_{\mathbf{b}}(t)]_{w} + \left[\omega_{\mathbf{b}}(t) \times [\mathbf{R}_{\text{tip}}(t)]_{b}\right]_{w} \tag{3.2}$$

The bracket notation refers to the reference frame where the equation is represented: $[\cdot]_{\text{b}}$ refers to the coordinate frame with the basis $\hat{\mathbf{e}} = [\hat{e}_1, \hat{e}_2, \hat{e}_3]^T$, and $[\cdot]_{\text{w}}$ refers to the coordinate frame with the basis $\hat{\mathbf{p}} = [\hat{p}_1, \hat{p}_2, \hat{p}_3]^T$.

The motion is a combination of the body and wing kinematics. The wing rotation rate, $\omega_{\mathbf{w}}(t)$ is given by the wing kinematics. The body translation, $\mathbf{v}_{\mathbf{b}}(t)$, and rotation rate, $\omega_{\mathbf{w}}(t)$, could be related to a reference flight condition (e.g. forward flight), a translation perturbation, or a wind gust. The location of the wingtip is constant in the wing frame ($[\mathbf{R}_{\text{tip}}]_{w} = [0, R, 0]$, where R is the wingspan). However, due to the coordinate transformation, the wingtip location becomes a function of time in the body frame: $[\mathbf{R}_{\text{tip}}(t)]_{b} = \mathbf{h} + T_{bw}(t)\,[\mathbf{R}_{\text{tip}}]_{w}$. The vector $\mathbf{h}$ is the distance from the center of gravity to the wing hinge.

The angle of attack, is directly calculated from the components of $\mathbf{U}_{\text{tip}}$.

$$\alpha_{\text{tip}}(t) = tan^{-1}\left(\frac{\mathbf{U}_{\text{tip}}(t) \cdot \hat{p}_3}{\mathbf{U}_{\text{tip}}(t) \cdot \hat{p}_1}\right) \tag{3.3}$$

Once the tip velocity and angle of attack are known, the quasi-steady lift and drag are calculated according to Equation 3.1. For the calculation of aerodynamic moments, these forces are assumed to occur at the 60% span location. The forces

and moments on the vehicle can be determined according to the equations below:

$$[\mathbf{F}_{\text{aero}}(t)]_b = T_{bw}(t)\,[\mathbf{F}_{\text{aero}}]_w = T_{bw}(t)T_2(-\alpha_{\text{tip}}(t)) \begin{bmatrix} D(t) \\ 0 \\ L(t) \end{bmatrix} \tag{3.4}$$

$$[\mathbf{M}_{\text{aero}}(t)]_b = [\mathbf{R}_{60}(t)]_b \times [\mathbf{F}_{\text{aero}}(t)]_b \tag{3.5}$$

Given a set of wing and body kinematics, the quasi-steady model will estimate the aerodynamic forces on a flapping wing with minimal computational expense. By incorporating experimentally determined lift and drag coefficients, this estimate includes some, but not all, of the unsteady loads. Aerodynamic phenomena such as the LEV or tip vortex and the induced flow from lift that exist in the unsteady flow of a rotating wing are included in this method, as they would be captured in the experimentally-found lift and drag coefficients. The changes in loads due to alterations in the flow structures due to previous kinematic motion, or to the wake from previous wingstroke will not be accurate. Due to this, this experimentally-derived quasi-steady method of aerodynamic estimate may capture the majority of the flapping wing loads during the translation-dominated parts of the wingstroke; the estimate is not expected to be accurate during wing rotation at pronation or supination. During wing rotation, there are large changes in the flow structures as the LEV detaches from the surface of the wing, and a new LEV forms on the beginning of the next half-stroke. Additionally, a complex interaction with the wake occurs at the beginning of the new half-stroke. None of these phenomena will be accurately described by this simple quasi-steady method. The following two

techniques will aid in determining the overall accuracy.

3.3.2 Computational Fluid Dynamics

The computation of flow around the *Drosophila* model is accomplished by IBINS, an immersed boundary incompressible Navier-Stokes solver developed at the University of Maryland. Development of IBINS for the purpose of flapping wing aerodynamics can be found in Bush et al. (2008, 2010). [81, 82]. The *Drosophila* is treated as three rigid bodies (the insect body with two wings) that move through a stationary three dimensional Cartesian grid as shown in Fig. 3.2.

IBINS solves the incompressible Navier-Stokes equations using a semi-implicit fractional time step similar to the method laid out in Kim and Moin (1984) [83]. The convective terms are discretized using a 2nd order Adams-Bashforth scheme and the diffusive terms use a 2nd order Crank-Nicholson scheme. Spacial differencing is 2nd order central except for regions of high convection, where 2nd order upwind is used on the convective terms. Poisson's equation for pseudo-pressure is solved using Stone's strongly implicit procedure and enforces the zero divergence criterion. Pressure and shear forces on each facet of the immersed body are summed to obtain the aerodynamic forces and moments of the entire wing body system about the center of gravity. The simulation was run on a mesh size of 68 million nodes on a quadcore Intel Xeon 2.8 GHz machine with 24 GB RAM.

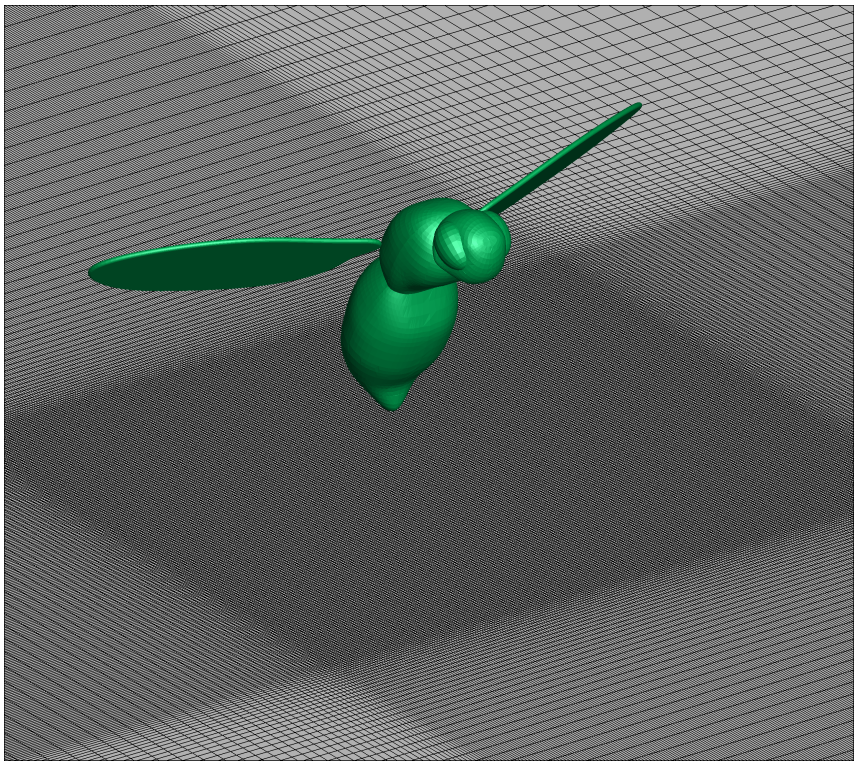
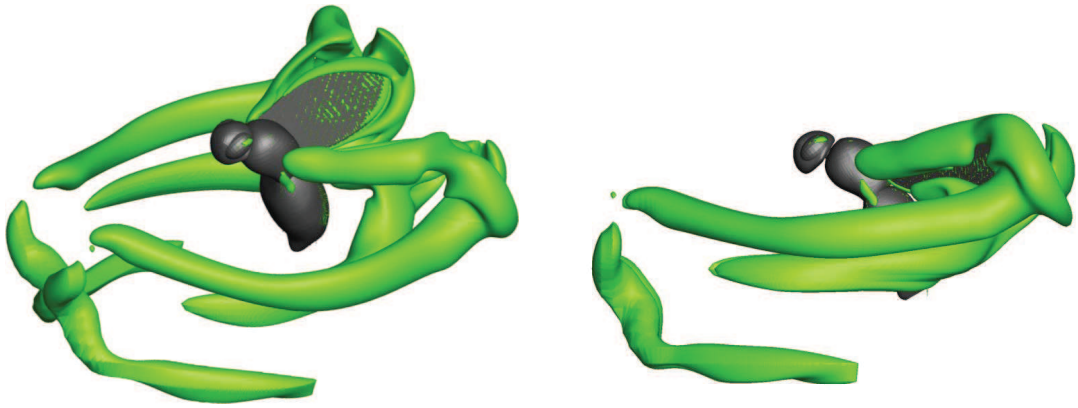


Fig. 3.2: The three immersed bodies (insect body and two wings) in the computational flow domain. The body remains stationary in the Cartesian grid while both wings rotate according to prescribed kinematics and force the aerodynamic flow.



(a) *(b)*

Fig. 3.3: Iso-surfaces of q-criterion of vorticity for the idealized hover kinematics near pronation. Vortical structures are shown attached to each wing and in the wake from previous strokes.

3.3.3 RoboFly

To verify the accuracy of quasi-steady and computational results, experimental estimates were sought. Through collaboration with Micheal Dickinson's lab, then at the University of Washington, the RoboFly setup was made available. The RoboFly apparatus includes a pair of independently controlled *Drosophila* wings scaled up to 0.23m in span. The apparatus was submerged in a tank filled with oil to give Reynolds number aerodynamic similitude. The wings were driven according to the slow and fast forward flight kinematics described in Chapter 2. To replicate forward flight or translational perturbations from a reference condition, RoboFly could be translated across the tank via a gantry system.

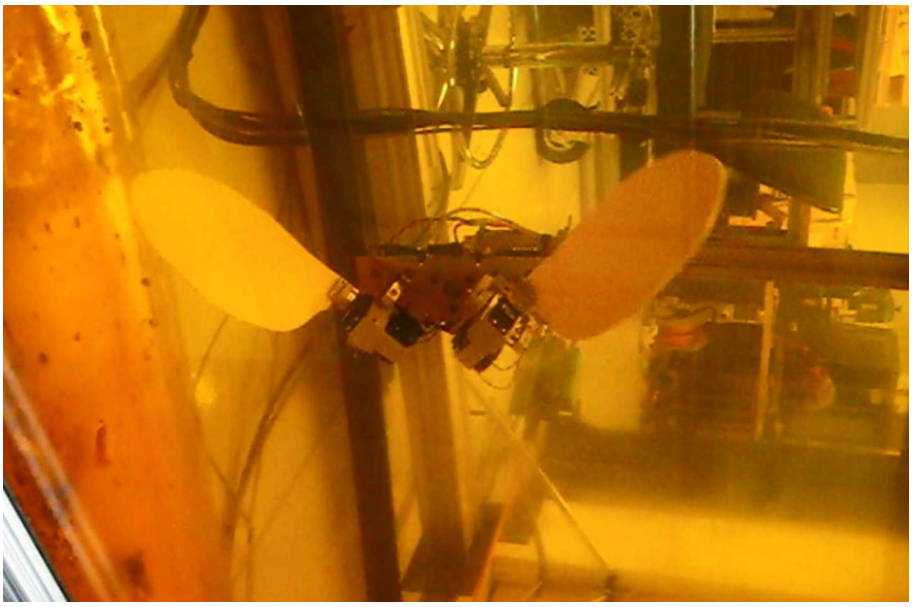


Fig. 3.4: The Robofly experimental apparatus from below the flapping wings.

3.3.4 Comparison for Example Wingstroke

Figure 3.5 shows a comparison of longitudinal loads (fore-aft force, X; vertical force, Z; pitching moment, M) estimated by the three above modeling techniques for the slow forward flight case. Lateral loads (side force, Y; rolling moment, L; yawing moment, N) are not shown because they are near zero due to cancellation by movement of two symmetric wingstrokes. The majority of the force keeping the vehicle aloft is generated during the downstroke (approximately $t/T = [0.7, 0.1]$) and the upstroke (approximately $t/T = [0.3, 0.6]$).

RoboFly and IBINS computational estimates are quite close. The quasi-steady aerodynamic calculation also follows the two more rigorous estimates, but varies slightly in two parts of the stroke. There are small dips in Z and oscillations in X

near pronation ($t/T = 0.25$) and supination ($t/T = 0.75$). This is expected, and can be attributed to the lack of rotational and wake capture estimates involved in the quasi-steady calculation. Perhaps more interesting is the loss of lift between $t/T = [0.5, 0.7]$, that is seen in both the computational and RoboFly results, but not the quasi-steady. This could be due to interaction with the previous wake and the increase in downwash, reducing the perceived angle of attack on the wing. There is little associated deviation in the X force, and this occurs when the wings are at their lowest point in the stroke, lending credence to the concept. Regardless, the quasi-steady model does capture the overall loads fairly well, without the expense of the more rigorous experimental and computational techniques. As will be discussed in the following chapter, high frequency errors between the aerodynamic models may not be important to the overall dynamics of the system.

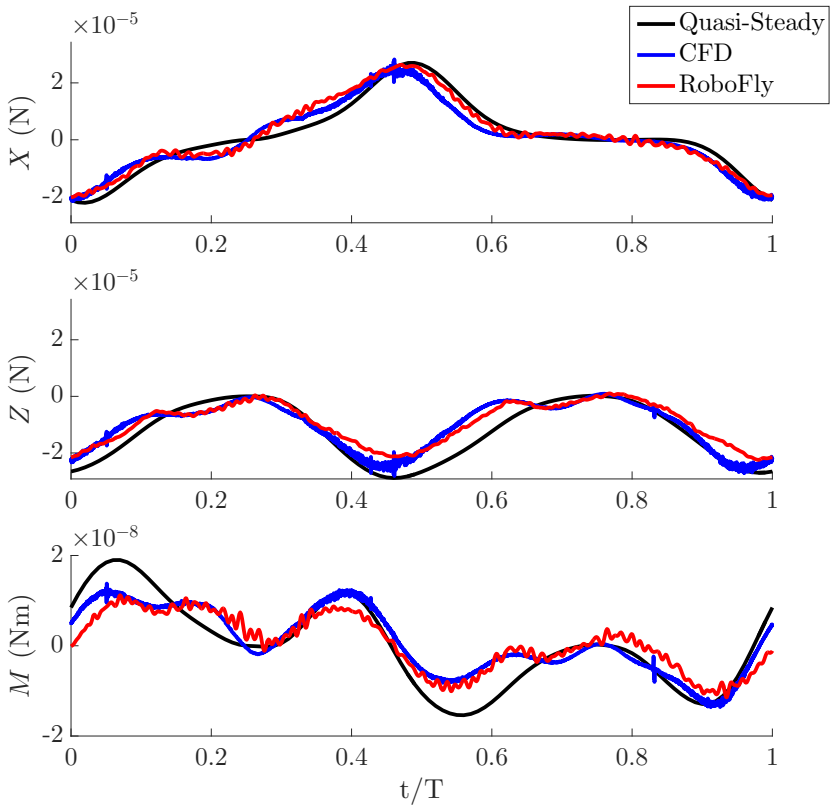


Fig. 3.5: Longitudinal loads throughout a wingstroke for a *Drosophila* in slow forward flight, as determined by the three modeling techniques: quasi-steady, computational, and experimental.

3.3.5 Calculation of Power Required for Flight

Interaction Between Aerodynamic and Inertial Power

The total power required for flight consists of both aerodynamic and inertial considerations. Aerodynamic losses are incurred by producing the lift required to counteract the insect's weight, termed induced power, and profile power required to overcome the aerodynamic drag on the wings and body. Inertial power is induced by the acceleration and deceleration of the wing. Inertial power includes not only the acceleration of the wing's mass but also the added mass of a volume of air near the wing that is considered to move together with the wing. This added mass of air that must be moved with the wing can be quite significant at small scales like that encountered by a fruit fly.

Previous work by Ellington [84] describes a method of estimating the average power required during a wingstroke, including all four terms: induced, profile, wing inertia, and added mass. Lehmann and Dickinson [85] furthered this approach by considering the efficiency gained by the reciprocal nature of the insect flapping mechanism. They suggested that the excellent power efficiency seen by insects can be a result of two effects: elastic energy storage and recovery of inertial power on the decelerating portions of the wingstroke. The aerodynamic power required is always positive and must be provided by the insect at all times throughout the stroke. But the inertial power changes sign throughout the stroke. When the wings are decelerating during the second half of each halfstroke, the inertial power can be used

to mitigate aerodynamic power requirements – essentially using aerodynamic losses to slow the wing down. Thus, the following equation for average power required is obtained by breaking down the wingstroke into quarter strokes:

$$\bar{P}_{\text{tot}} = \frac{1}{4}\sum_{k=1}^{4}(\bar{P}_{\text{aero}_k} + (-1)^k \eta^* \bar{P}_{\text{inert}_k}) \tag{3.6}$$

where $\bar{P}_{\text{aero}_k}$ is the average aerodynamic power required during the k^{th} quarter stroke, and $\bar{P}_{\text{inert}_k}$ is the magnitude of the mean inertial power required during a quarter stroke to accelerate or decelerate. The increased efficiency due to elasticity is represented by $\eta^* = 1 - \eta$, where η is the power retained due to elasticity of the wings. Lehmann and Dickinson suggest 10%, which is used here. The coefficient $(-1)^k$ will determine the sign change of inertial power depending on whether the wing is accelerating or decelerating; as written, the kinematics are assumed to begin during an accelerating phase.

Because the power required to stretch the flight muscles is insignificant compared to the power required for contraction, any excess inertial power over that required by the aerodynamics on decelerating portions of the stroke is considered negligible. Lehmann and Dickinson use a rectification function $R(x)$ that simply sets all x lower than zero to zero. Assuming the wingstroke begins during an accelerating phase, Equation 3.6 can be broken down into quarter strokes:

$$\bar{P}_{\text{tot}} = \frac{1}{4}[(\bar{P}_{\text{aero}_1} + \eta^* \bar{P}_{\text{inert}_1}) + R(\bar{P}_{\text{aero}_2} - \eta^* \bar{P}_{\text{inert}_2}) \tag{3.7}$$

$$+(\bar{P}_{\text{aero}_3} + \eta^* \bar{P}_{\text{inert}_3}) + R(\bar{P}_{\text{aero}_4} - \eta^* \bar{P}_{\text{inert}_4})] \tag{3.8}$$

Aerodynamic Power

The aerodynamic power throughout the wingstroke is measured directly by IBINS calculations. At each surface facet on an immersed body, the power is calculated by a dot product of the aerodynamic force on that facet with its velocity. The summed power over all the facets of each body gives the aerodynamic power requirement for each instant in time. An estimate of average aerodynamic power required for each quarter stroke is obtained by a simple integration. Calculating the power for individual quarter strokes is critical for the forward flight reference condition considered here – the downstroke will necessarily produce higher loads and also power requirements due to the added effect of the freestream velocity.

Inertial Power

The majority of inertial loading is obtained solely by the flapping in the stroke plane. The inertial power required during a quarter stroke $\bar{P}_{\text{inert}_k}$ is calculated by the change in kinetic energy during a quarter stroke:

$$E_{\text{kin}} = \frac{1}{2} I_{\text{tot}} \omega^2 \tag{3.9}$$

where $I_{\text{tot}} = I_w + I_{\text{add}}$ is the combined moment of inertia of the wing and added mass of air, and ω is the rotational speed of the wing. The wing and added mass inertias are calculated according to Ellington [84]. Assuming inertial effects resulting from the wing moving outside the stroke plane are negligible, the inertial power required will be determined solely by the stroke angle. The magnitude of the inertial power

during each quarter stroke $\bar{P}_{\text{inert}_k}$ becomes constant; the sign changes depending on whether the wing is accelerating or decelerating as indicated in Eq. 3.6.

$$\bar{P}_{\text{inert}} = \frac{4}{T}\int_0^{T/4} I_{\text{tot}}\dot{\phi}\ddot{\phi}d\tau \tag{3.10}$$

Eq. 3.10 together with Eq. 2.5 yields the following expression for mean inertial power required for a single wing during a quarter stroke:

$$\bar{P}_{\text{inert}} = 8\pi^2 I_{\text{tot}} f^3 \phi_{\text{max}}^2 \tag{3.11}$$

3.4 Summary

This chapter outlined the methodology for calculating aerodynamic loading that will be used for modeling flapping wing vehicle dynamics. Three aerodynamic estimation methods are presented: an experimentally-derived quasi-steady model, the IBINS incompressible flow solver, and the RoboFly experimental setup. IBINS and RoboFly are much more rigorous than quasi-steady method, and they will capture the unsteady aerodynamics around the flapping wing. The quasi-steady method will capture some of the unsteady effects due to the experimental basis from which it was derived, but other aerodynamic phenomena will be unmodeled.

The three methods are compared for a set of *Drosophila* wing kinematics, verifying the computational and experimental results. Longitudinal load results showed that the quasi-steady method does capture most of the aerodynamic loading, with some exception particularly at stroke reversal.

A calculation of power is also presented, based on a combination of aerody-

namic calculation from IBINS and biologically-motivated inertial power consumption. These calculations will be used in Chapter 5 for estimating power consumption of flapping wing kinematic control inputs.

Chapter 4: Dynamical Modeling

4.1 Rigid Body Dynamics

Rigid body equations of motion for a flapping wing vehicle or insect in flight are derived from Newton's second law of motion. For vehicles with an xz plane of symmetry the equations reduce to the system of ordinary differential equations

$$X - mg\sin(\theta) = m(\dot{u} + qw - rv) \tag{4.1}$$

$$Y - mg\cos(\theta)\sin(\phi) = m(\dot{v} + ru - pw) \tag{4.2}$$

$$Z + mg\cos(\theta)\cos(\phi) = m(\dot{w} + pv - qu) \tag{4.3}$$

$$L = I_x\dot{p} + qr(I_z - I_y) - I_{xz}pq \tag{4.4}$$

$$M = I_y\dot{q} + rp(I_x - I_z) + I_{xz}(p^2 - r^2) \tag{4.5}$$

$$N = I_z\dot{r} - I_{xz}\dot{p} + pq(I_y - I_x) + I_{xz}qr \tag{4.6}$$

where X, Y, and Z are the aerodynamic forces in the direction of body-fixed axes $\hat{e}_1$, $\hat{e}_2$, $\hat{e}_3$, and L, M, and N are the aerodynamic moments around the same axes. The translation of the body is given by $\mathbf{v_b} = u\hat{e}_1 + v\hat{e}_2 + w\hat{e}_3$ and the rotation rate of the frame is $\omega_\mathbf{b} = p\hat{e}_1 + q\hat{e}_2 + r\hat{e}_3$. The longitudinal equations for X, Z, and M can be decoupled from the lateral-directional dynamics. This allows treatment

of the complexities of modeling each aspect of flapping wings vehicle dynamics independently.

4.1.1 Small Perturbation Theory

The system of ordinary differential equations can be linearized using small disturbance theory, where the motion is assumed to be small deviations in the flight path away from a reference condition. Each variable in Equation 4.6 is replaced by the reference value plus some small deviation. For example, $u = u_0 + \Delta u$, $\theta = \theta_0 + \Delta\theta$, $X = X_0 + \Delta X$, etc. The reference condition could be any flight path, but this work focuses on hovering and forward flight. This assumes that w_0, v_0, p_0, q_0, and r_0 are all set to 0.

Introducing this notation into the first differential equation in Eq. 4.6 and neglecting products of any disturbance (as they are non-linear terms) results in

$$X_0 + \Delta X - mg\sin(\theta_0 + \Delta\theta) = m\dot{u} \tag{4.7}$$

At trim, all perturbations are zero, so the equilibrium equation is

$$X_0 - mg\sin(\theta) = 0 \tag{4.8}$$

By subtracting the equilibrium equation from Equation 4.7, and applying the small angle theorem, the linear equation is reached

$$\Delta\dot{u} = \frac{1}{m}\Delta X - g\Delta\theta \tag{4.9}$$

The aerodynamic term ΔX incorporates any aerodynamic forcing on the system in the $\hat{e}_1$ direction, including changes in X due to state perturbations or due to

control inputs. Taking the linear terms of a Taylor series expansion,

$$\frac{1}{m}\Delta X = X_u\Delta u + X_w\Delta w + X_q\Delta q + X_\theta\Delta\theta + \frac{1}{m}X_\delta\Delta\delta \tag{4.10}$$

where the terms $X_{[\cdot]}$ are aerodynamic stability derivatives, scaled by the mass: $X_{[\cdot]} = \frac{1}{m}\frac{\delta X}{\delta[\cdot]}$. The final term, $\Delta\delta$, incorporates the aerodynamic forcing due to all control inputs. For the biologically-inspired control inputs discussed in Chapter 2, the control term expands to

$$\frac{1}{m}X_\delta\Delta\delta = X_{\phi_{\max}}\Delta\phi_{\max} + X_{\phi_{\text{off}}}\Delta\phi_{\text{off}} + X_\beta\Delta\beta + X_f\Delta f \tag{4.11}$$

Using small perturbation analysis, the nonlinear system is reduced to the following familiar form

$$\dot{\mathbf{x}}(t) = A(t)\mathbf{x}(t) + B(t)\mathbf{u}(t) \tag{4.12}$$

where $A(t)$ is the stability matrix, $B(t)$ is the control matrix, and $\mathbf{x}(t)$ and $\mathbf{u}(t)$ are the vector of vehicle states and control inputs respectively.

For longitudinal flight, $\mathbf{x} = [u,\ w,\ q,\ \theta]^T$, and $\mathbf{u} = [\delta_{\phi_{\max}},\ \delta_{\phi_{\text{off}}},\ \delta_\beta,\ \delta_f]^T$. The corresponding stability and control matrices for longitudinal flight are

$$A(t) = \begin{pmatrix} X_u(t) & X_w(t) & X_q(t) & -g \\ Z_u(t) & Z_w(t) & Z_q(t) + u_0 & 0 \\ M_u(t) & M_w(t) & M_q(t) & 0 \\ 0 & 0 & 1 & 0 \end{pmatrix} \tag{4.13}$$

$$B(t) = \begin{pmatrix} X_{\phi_{\max}}(t) & X_{\phi_{\text{off}}}(t) & X_\beta(t) & M_f(t) \\ Z_{\phi_{\max}}(t) & Z_{\phi_{\text{off}}}(t) & Z_\beta(t) & M_f(t) \\ M_{\phi_{\max}}(t) & M_{\phi_{\text{off}}}(t) & M_\beta(t) & M_f(t) \\ 0 & 0 & 0 & \end{pmatrix} \tag{4.14}$$

Note that the stability derivatives are functions of time, and are periodic in $T = 1/f$. The next section will discuss a further simplification from a linear time periodic system to a linear time invariant system.

4.1.2 Wingstroke Averaging

Vehicle motion from unsteady forcing can be broken into two components, high frequency vibrations and the low frequency flight path of the vehicle. Because the flight path resulting from any forcing is the item of interest for the study of vehicle dynamics, the high frequency content can often be neglected for tractability. Vehicle inertia limits the speed of system response to any inputs, and a "two-timing" assumption gives resulting low frequency flight path from an averaged high frequency forcing. [63]

For flapping wing vehicles, the aerodynamic forcing is often much faster than the resulting vehicle motion, and this approach is often taken if the forcing frequency is more than ten times that of the vehicle motion. [45, 86] For the *Drosophila*-scale insect considered here, the frequency of the wing flapping (200 Hz) is much greater than the speed of rigid body motion (about 6Hz [87]), such that the periodicity of forcing causes a negligible effect on the motion of the vehicle. Wu and Sun [64] showed that for larger insects with lower wingbeat frequencies this approximation was not valid, while for a dronefly the assumption is valid. Here, this approximation is tested by considering first the stroke-averaged forces in a time-invariant model, and comparing the results with a time-periodic model that includes high frequency

aerodynamic forcing.

When using this assumption, the wingstroke-averaged aerodynamic force is used for the calculation of the stability and control derivatives in Equations 4.13 & 4.14. The stroke-averaged forces are simply $\bar{\mathbf{F}} = \frac{1}{T}\int_0^T \mathbf{F}(t)dt$, where $\mathbf{F}(t) = [X(t),\ Y(t),\ Z(t)]^T$ is periodic in T.

4.2 Linear Time Invariant Models

As described in Chapter 2, three reference flight conditions are modeled: hovering flight, slow forward flight, and fast forward flight. Dynamic models resulting from quasi-steady aerodynamic technique are compared to the more rigorous computational and experimental models. The linear time invariant dynamic models result from the changes in stroke-averaged aerodynamic forces and moments due to perturbations in state as estimated by each of the aerodynamic techniques.

4.2.1 Hovering Flight

For hovering flight, the flat stroke plane kinematics shown in Figure 2.8 are used. An example of the change in longitudinal loads is given by Figure 4.1. The quasi-steady and CFD estimates are comparable, and stroke-averaged loads change similarly with perturbations in other states, as shown in Figure 4.2. Note that, with the body axes having $\hat{e}_3$ pointed down, a negative stroke averaged load in Z is countering gravity. In this case, the Z force is higher in magnitude for the CFD results, a result due to the force peaks seen during stroke reversal; similar peaks

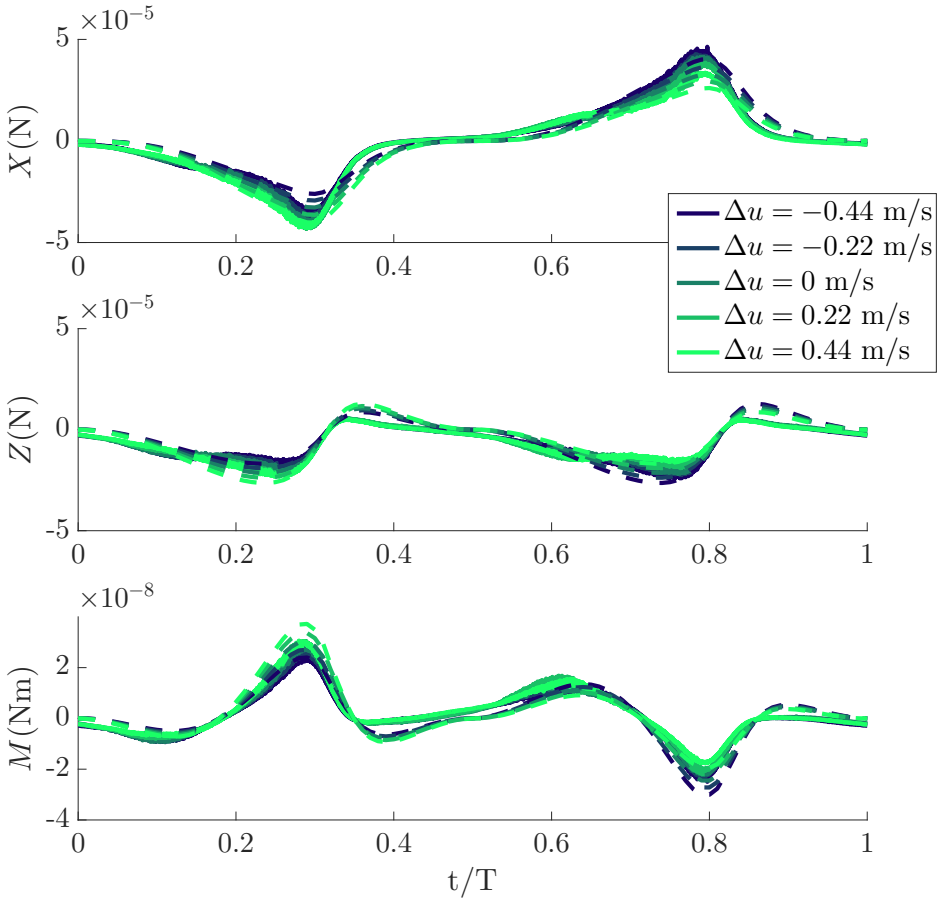


Fig. 4.1: Aerodynamic loads of an idealized hovering *Drosophila* calculated by IBINS with translational perturbations in the x-direction from hover. CFD results are solid lines; Quasi-steady are dashed.

have been seen for these kinematics by Dickinson et al. [54]

The vital feature for dynamical modeling, however, is actually the slope of the linear regression through stroke-averaged points that give the stability derivatives which constitute the stability matrix, A, of the longitudinal linear system model. Thus, an offset in the estimated loads between the two different aerodynamic methods does not affect the dynamical modeling; however, a difference in the way the loads change with state perturbations could have significant effect. In Figure 4.2, the quasi-steady model proves capable of predicting the changes in stroke-averaged loads except due to perturbations in Δu, where the stability derivatives X_u and M_u are under-predicted.

Figures 4.3 & 4.4 show the resulting eigenstructure of the system. Both the quasi-steady model and the CFD model have a fast subsidence mode in the deep left half plane, a slower subsidence mode also in the left half plane, and a pair of oscillatory unstable modes in the right half plane. In Figure 4.4, we can see that the fast subsidence mode (λ_1) is comprised of motion in surge and pitch rate; the slow subsidence mode (λ_2) is the only mode containing heave motion; and the oscillatory modes ($\lambda_{3,4}$) show surge and pitch rate motion that will grow with time. This is also the same form as other previously identified hovering insects, and, in fact, longitudinal poles for helicopters in hover (albeit much faster motion in the insect case). [45, 50, 88]

Faruque & Humbert (2010a) considered the same kinematics when estimating the LTI model of a hovering *Drosophila*-scale insect. That work involved a

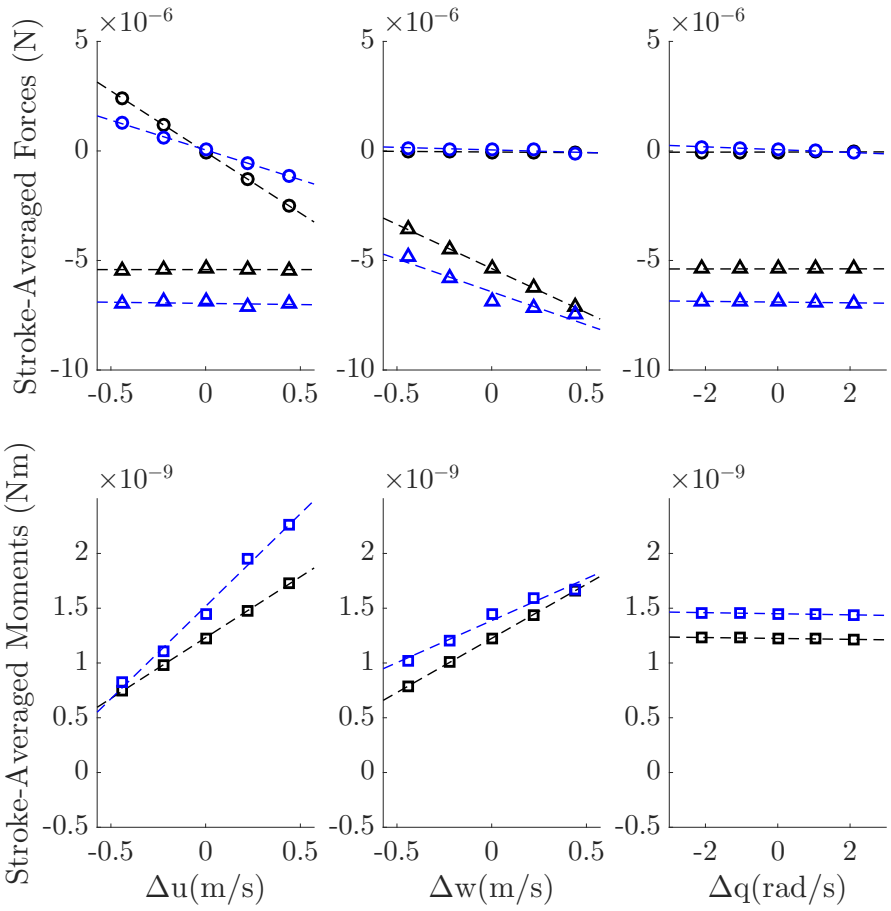


Fig. 4.2: Time-averaged aerodynamic loads of an idealized hovering *Drosophila* with perturbations in longitudinal states. Circles show X, triangles Z, and squares M; results from the quasi-steady model are in black, CFD in blue. The resulting linear regressions are shown as dashed lines of the corresponding color.

frequency-based identification of the linear system from non-linear simulation, and used the quasi-steady aerodynamic method. In order to reduce the inherent instability of motion and make the linearization possible, a degree of q-feedback control was added to that system. After adding the same degree of control on the M_q term to the quasi-steady model, the resulting linearized system approaches the same model.

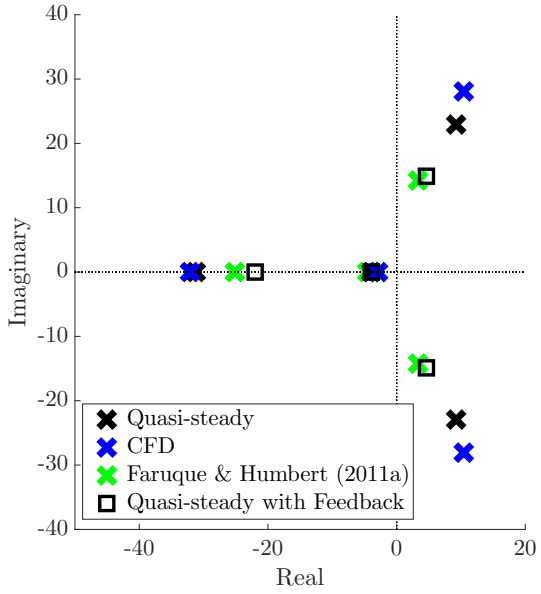


Fig. 4.3: Longitudinal LTI modes of an idealized hovering *Drosophila* in slow forward flight. Adding pitch rate feedback gives similar results to those presented in Faruque and Humbert (2011a).

The modes of that system are included in Figure 4.3 with the results of Faruque et al. (2011a) that considered the same kinematics.

These results allow a first glimpse of the effectiveness of the quasi-steady aerodynamic model in estimating flapping wing vehicle dynamics. The quasi-steady model performs well, and estimates a very similar linear dynamic model to the computationally-derived model. Moreover, a comparison with previous results by Faruque et al. show that the small perturbation method of estimating the linear dynamics aligns with frequency-based modeling.

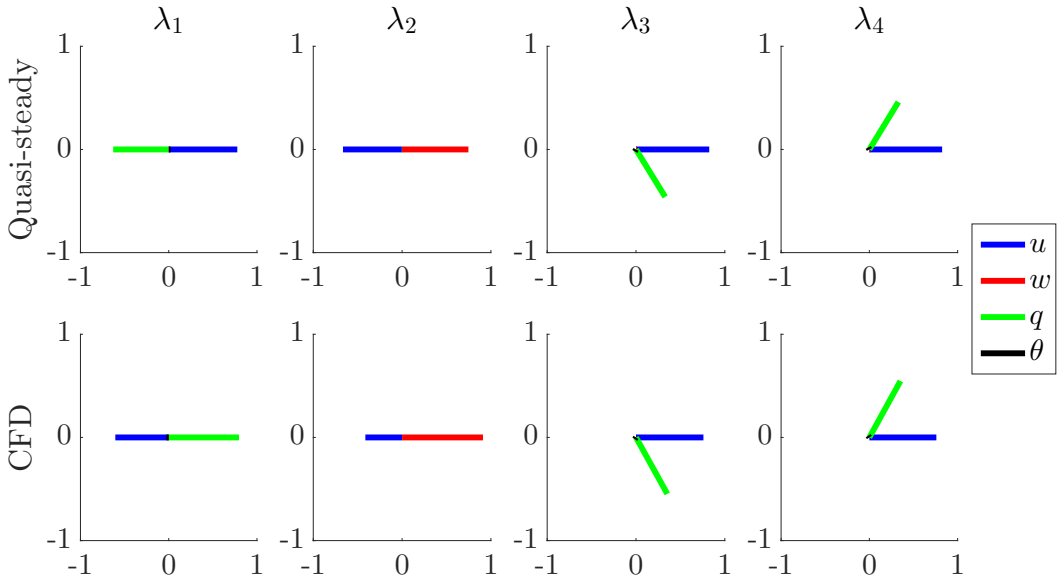


Fig. 4.4: Argand diagrams displaying the variation in eigenstructure for each aerodynamic model. Each plot shows the components of the eigenvector plotted on the complex plane, each component corresponding to an individual state. The first two modes shown are subsidence modes, and eigenvectors exist completely on the real axis. The second two modes are the oscillatory modes; the angle between u and q components shows the lead or lag in phase of the interchange of motion between the two components. Eigenvectors are scaled to unit norm. Note the isolation of vertical motion to the slow subsidence mode, λ_2.

4.2.2 Forward Flight

Longitudinal Flight

In forward flight, RoboFly experiments were available to ensure that the CFD results from IBINS were in fact accurately estimating the flapping wing aerodynamics. The kinematics used in forward flight were determined from freely flying *Drosophila*, as described in Chapter 2; the wing kinematics are provided in Figure 2.6.

The stroke-averaged longitudinal loads are shown in Figure 4.5 for slow forward flight, and the resulting modes are shown in Figure 4.6. In this case, there is remarkable similarity between the results of the two rigorous methods. Notably, the quasi-steady method over-predicts the vertical stroke-averaged force compared to RoboFly and IBINS CFD.

The fast forward flight modes are very similar to the slower reference condition, as shown in Figure 4.7. The resulting linear modes of the system are similar in structure to those of hover, with the exception that much more coupling exists in the heave dynamics, as can be seen by looking at the eigenvector composition of the fast forward flight in Figure 4.9. Increasing the reference speed has a stabilizing effect, moving the oscillatory modes further to the left on the complex plane, in exchange for slowing the rate of decay for the fast subsidence mode.

As in hover, the quasi-steady aerodynamic model provides a longitudinal forward flight model that is verified by both the CFD and RoboFly results. The models

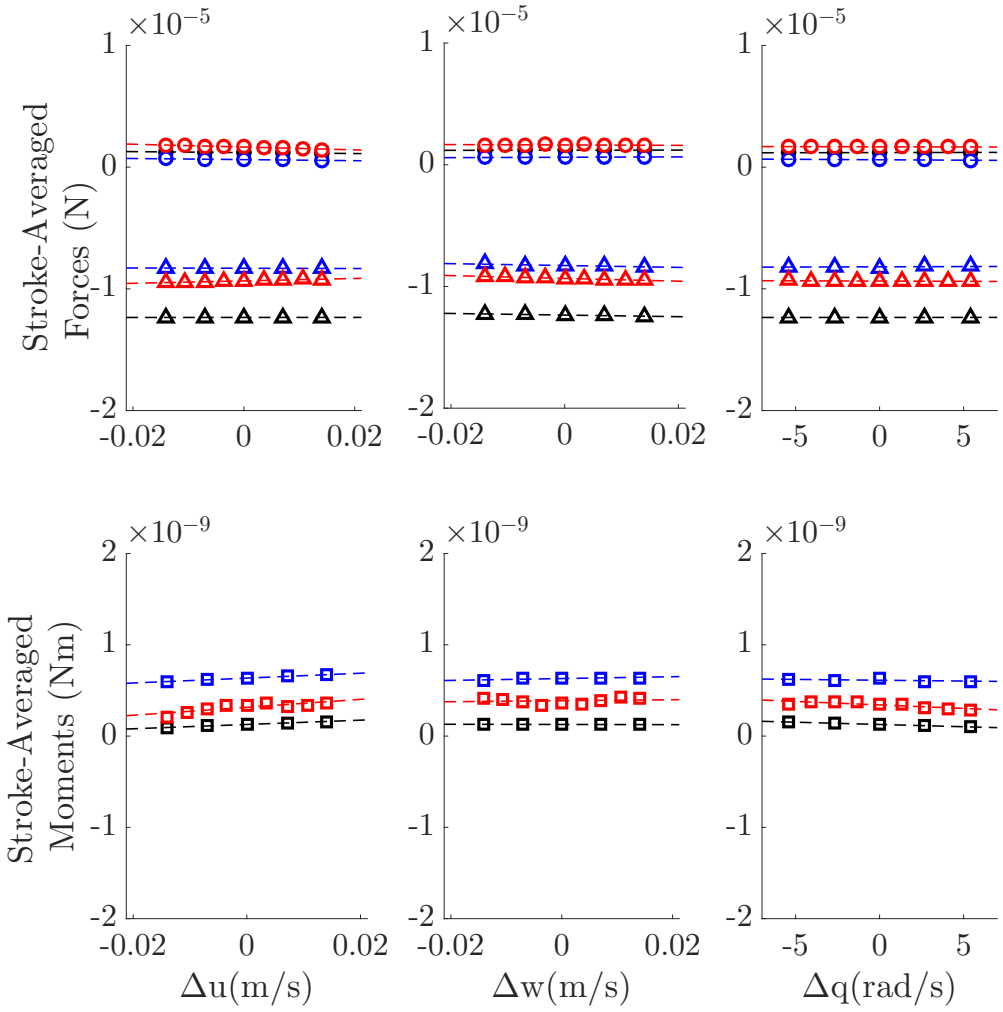


Fig. 4.5: Time-averaged aerodynamic loads of a forward flying *Drosophila* with perturbations in longitudinal states. Circles show X, triangles Z, and squares M; results from the quasi-steady model in black, CFD in blue, RoboFly in red. The resulting linear regressions are shown as dashed lines of the corresponding color.

generated by the more robust aerodynamic estimates via CFD or RoboFly are as close to the quasi-steady dynamics as to each other. While an offset in some of the longitudinal loads exists, the stability derivatives and the resulting linear models

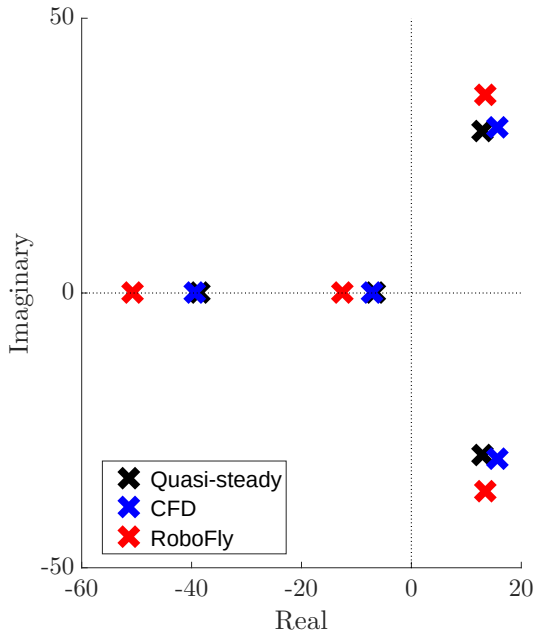


Fig. 4.6: Longitudinal LTI modes of a forward flying *Drosophila* in slow forward flight.

are quite similar. This suggests that high frequency aerodynamic forcing within the wingstroke has minimal effect on the overall longitudinal dynamics of a *Drosophila*-scale flapping wing vehicle.

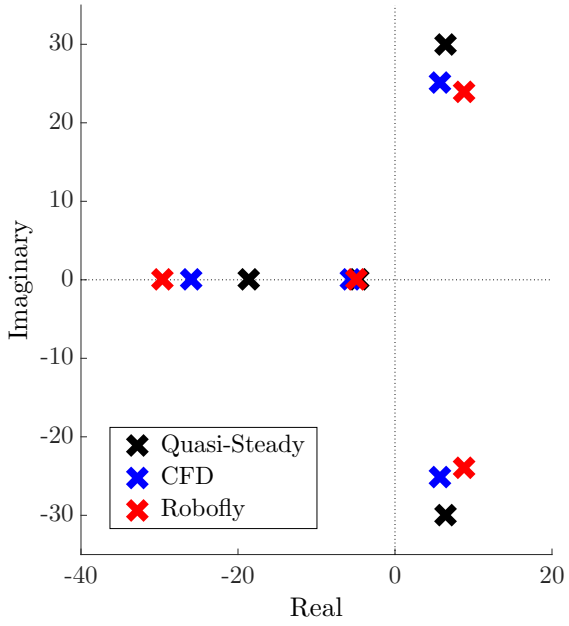


Fig. 4.7: Longitudinal LTI modes of *Drosophila* in fast forward flight.

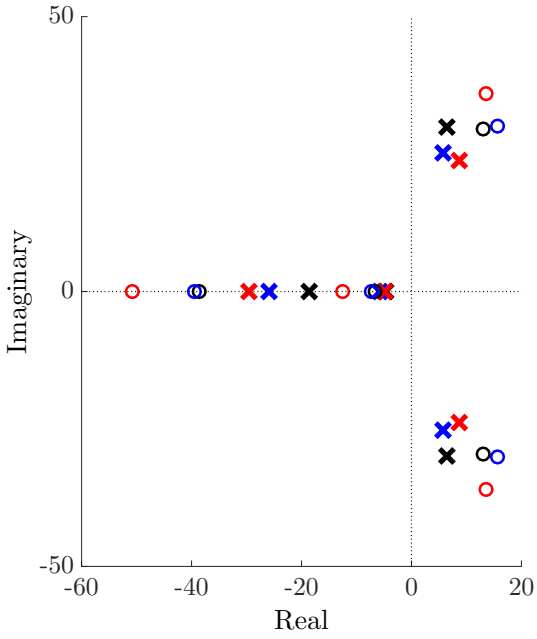


Fig. 4.8: Comparison of longitudinal flight modes of *Drosophila* in fast and slow forward flight. Slow forward flight is shown with circles, fast with x's; as before, quasi-steady results are in black, CFD in blue, and RoboFly in red.

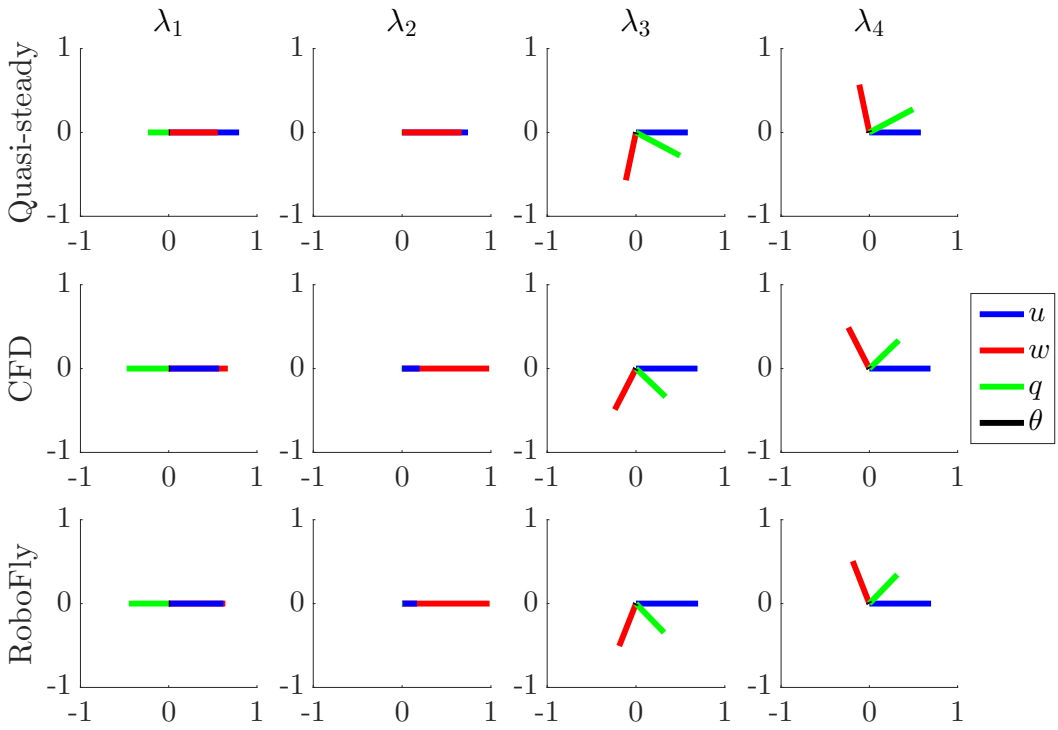


Fig. 4.9: Argand diagrams displaying the variation in eigenstructure for each aerodynamic model. Each plot shows the components of the eigenvector plotted on the complex plane, each component corresponding to an individual state. Note that the heave dynamics are fully coupled to the surge and pitching motion in forward flight.

Lateral-Directional Flight

The above analyses for hovering and forward flight dynamics only considered longitudinal motion of the insect. An equivalent system in the form of Eq. 4.12 can be derived for lateral-directional flight, where the state equation is $\mathbf{x} = [v,\ p,\ \phi,\ r]^T$. The stability matrix for lateral-directional flight is then

$$A(t) = \begin{pmatrix} Y_v & Y_p & g & Y_r - u_0 \\ L_v & L_p & 0 & L_r \\ 0 & 1 & 0 & 0 \\ N_v & N_p & 0 & N_r \end{pmatrix} \tag{4.15}$$

The same methodology as above is used, but with perturbations in the lateral-directional states. Figure 4.10 shows the stroke-averaged load results. Note that the scale is much smaller for many of the deviations in stroke-averaged loads from the reference compared to the longitudinal loads in Figures 4.2 & 4.5.

The case for quasi-steady estimation of lateral-directional flight is not as strong. Many of the stability derivatives from the quasi-steady aerodynamic model do not agree with those given by CFD. This leads to a very different lateral-directional dynamical model, shown in Figure 4.11. RoboFly is not capable of lateral-directional perturbations, and so the computational results cannot be validated with experimental results.

The discrepancy could be a result of high frequency aerodynamics that are not included in the quasi-steady model. Figure 4.12 shows the rolling moment, L throughout the wingstroke with perturbations in sideslip. The quasi-steady model does capture most of the content contained in the CFD results; however, the CFD

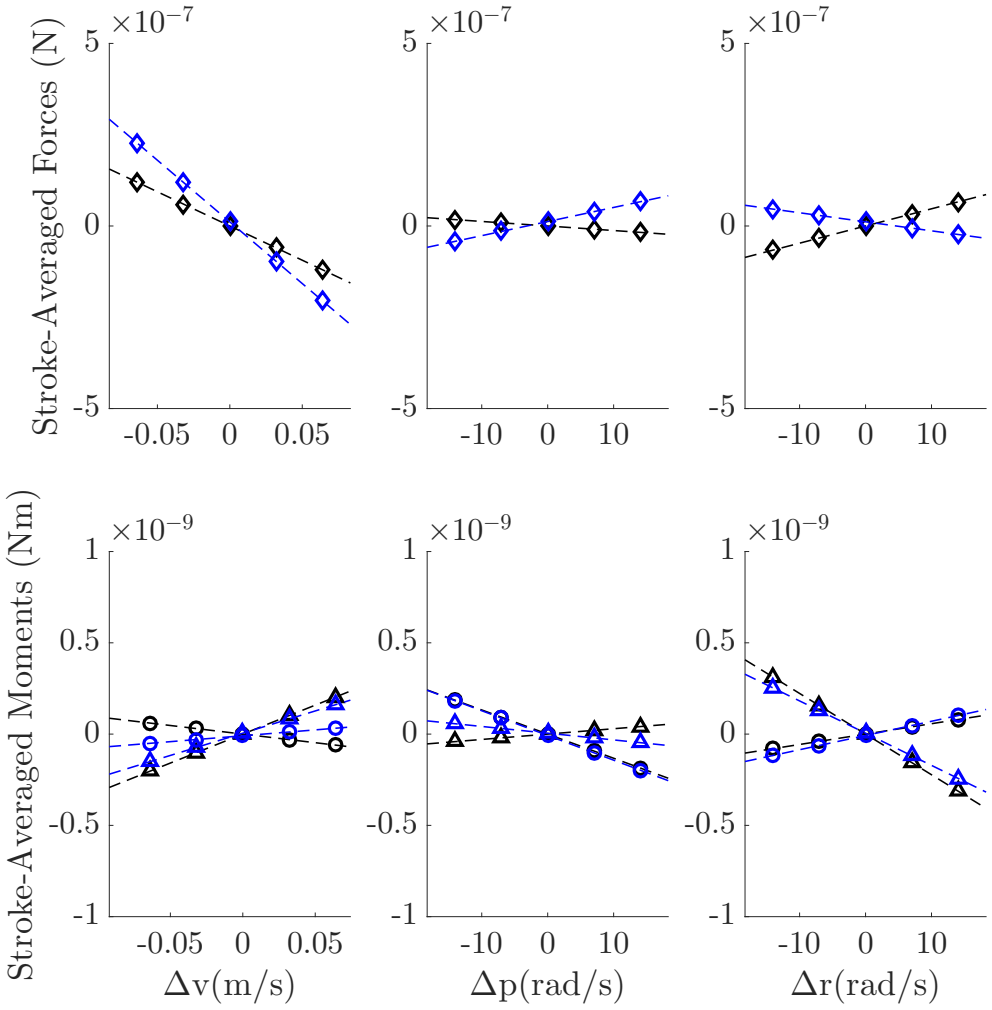


Fig. 4.10: Time-averaged aerodynamic loads of a forward flying *Drosophila* with perturbations in lateral-directional states. Diamonds show Y, circles L, and triangles N; results from the quasi-steady model in black, CFD in blue. The resulting linear regressions are shown as dashed lines of the corresponding color.

results are quite noisy due to the small signal (compare to Fig. 3.5) returned due to these perturbations. The small differences between the quasi-steady rolling moment and CFD rolling moment due to these perturbations cause the stability derivative

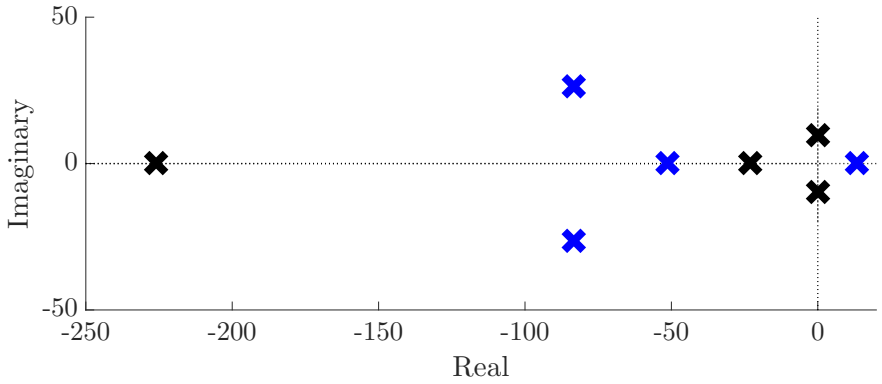


Fig. 4.11: Lateral-directional LTI modes of *Drosophila* in fast forward flight.

(L_v) to be positive in the CFD case, or negative in the quasi-steady case. This sign change in one stability derivative is enough to change the entire structure of the linear model, and make it unstable.

The discrepancy may, however, be due to inaccurate predictions by the quasi-steady aerodynamic method. Faruque & Humbert (2010b), also using the quasi-steady code described stable lateral-directional modes similar to those given by the quasi-steady method here: stable oscillatory roll motion near the imaginary axis, and stable yaw subsidence modes. [72] Xu & Sun (2013), using a Navier-Stokes solver, found a modal structure of bumblebees quite similar to that found in the IBINS case here: stable oscillatory rolling motion, and an unstable yaw motion. [66] Although these are for different insects with different kinematics, the aerodynamic calculation is possibly the major contributing factor for the disparate results. Xu & Sun have proposed that the sideslip motion (v) may cause a loss in axial velocity along one of the wings. This could cause an instability in the LEV on the windward

facing wing, altering the instantaneous lift and drag. A detachment of the LEV on a single wing of the vehicle would cause a substantial rolling moment and could certainly change the sign of L_v as seen in the above results. Such an unsteady effect would not be incorporated into the quasi-steady aerodynamic method, and would severely limit its use in lateral-directional flight estimates. Verification via experiment or more accurate computation is necessary to definitively say whether the quasi-steady method has failed in determining the lateral-directional dynamics.

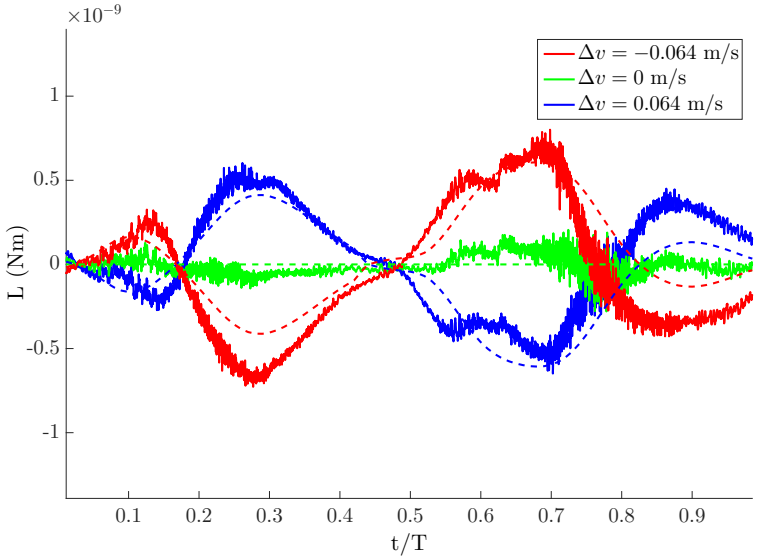


Fig. 4.12: Rolling moment throughout a wingstroke in fast forward flight for varying sideslip. Quasi-steady results are dashed, CFD in solid.

4.3 Linear Time Periodic Model

Small insects such as *Drosophila* and *Caliphora* that have relatively low-mass, rigid wings that flap at high frequency allow assumptions not applicable for larger flapping systems. As the flapping wing system increases in size, the increased inertia

in the wing wing increases the bending in the wing, and the time scale of the wingbeat slows, approaching that of the flapping system. It is of particular interest whether these assumptions of wing rigidity and time-scale invariance are applicable to the hummingbird-scale, as this is the size of many proposed flapping wing MAVs.

In the above analyses we assumed that a "two-timing" approach could be taken to the vehicle dynamics such that only the aerodynamic loads averaged over the wingstroke were important to the overall vehicle dynamics. In this section we test that assumption.

The aerodynamic forcing on a flapping wing platform is periodic in T, and so the linearized equations of motion can be considered on a periodic timeframe, where the stability and control matrices are also periodic with the wingstroke period.

$$\dot{\mathbf{x}}(t) = A(t)\mathbf{x}(t) + B(t)\mathbf{u}(t) \tag{4.16}$$

where $A(t+T) = A(t)$ and $B(t+T) = B(t)$. The LTP characterization can be accomplished using Floquet decomposition, which transforms the current periodic system into a time invariant system. In the transformed coordinate system, common LTI control and modeling techniques can be utilized. To find the transformation between the LTP and LTI systems, the periodic $A(t)$ must first be found. As before, the matrix is composed of stability derivatives that describe changing aerodynamic loads due to perturbations in state, but now those stability derivatives are periodic in time. An example of the periodic loads changing with time and with perturbation in the pitch rate, q, is given in Figure 4.13.

The goal of the Floquet decomposition is to find a linear transformation $P(t)$

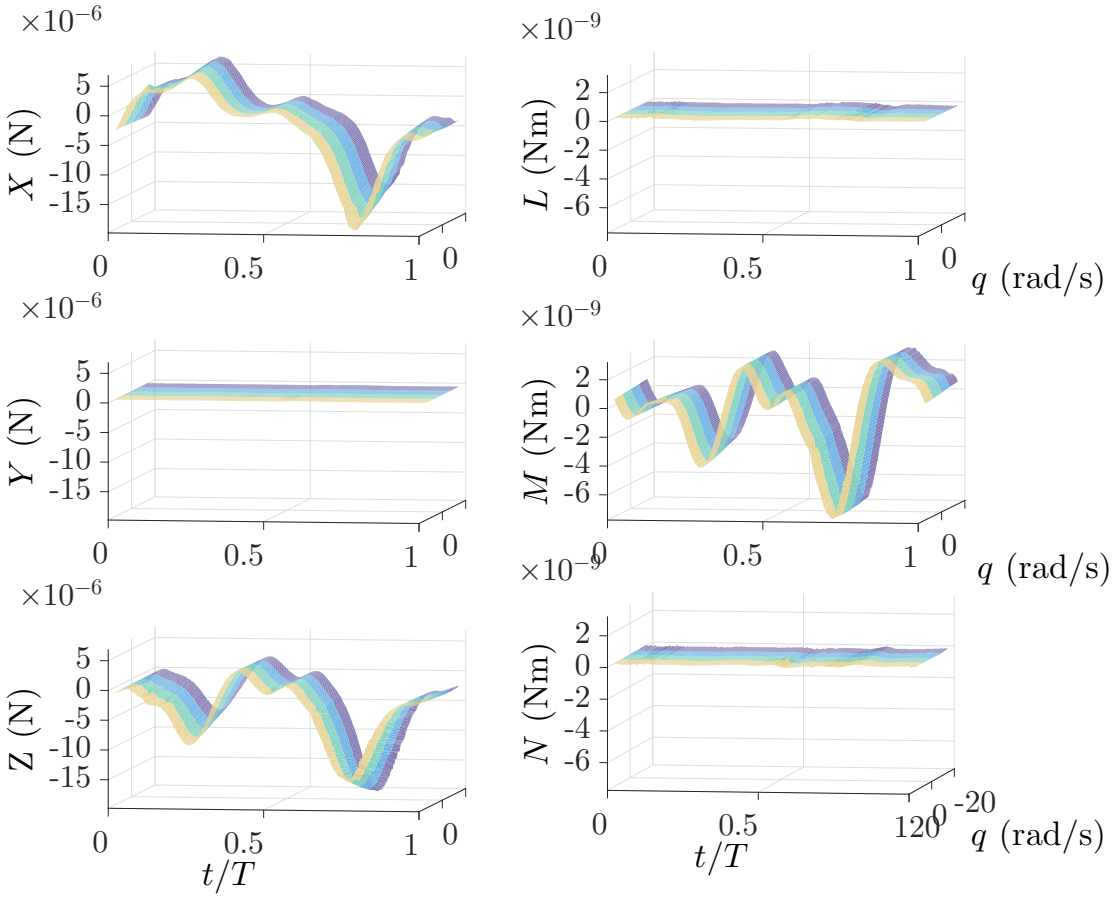


Fig. 4.13: Surface plots of forces and moments as functions of both time and perturbation in pitch rate. The stability and control matrices can be characterized as functions of time by measuring the change in loads with perturbations in state or control input for each instant in time.

between the LTI and LTP coordinates:

$$x(t) = P_z(t)\tilde{x}(t) \tag{4.17}$$

where $\tilde{x}(t)$ is the state vector in the artificial LTI coordinates. This $P_z(t)$ is also periodic. The transformation $P_z(t)$ is found using fundamental solutions $\psi(t)$ of $A(t)$. These fundamental solutions create a basis set for all solutions of the periodic system, and are the solution to the ordinary differential equation, $\dot{\psi}(t) = A(t)\psi(t)$, with any set of linearly independent initial conditions (e.g. $\psi(0) = I$). The fundamental solutions are not periodic and change with every wingstroke; however, the transition of the fundamental solutions from one period to the next, $Q = \psi(t)^{-1}\psi(t+T)$, is constant. This matrix Q is analogous to a state transition matrix, and takes the form $Q = e^{A_z T}$, where the period of the flapping is T, and A_z is the system matrix in the new LTI coordinates ($\dot{\mathbf{z}}(t) = A_z\mathbf{z}(t)$, for zero inputs). Now the transformation at every time can be found via

$$P_z(t) = \psi(t)e^{-A_z t} \tag{4.18}$$

and use Equation 4.17 to transform between the LTP and LTI systems.

The stability of a periodic system can no longer be determined by the eigenstructure of $A(t)$. Instead, the magnitude of the eigenvalues of the Floquet transition matrix, Q, must remain less than one for the system to be stable. A standard example used to illustrate this is the system with

$$A(t) = \begin{pmatrix} -1 + 1.5\cos^2(t) & 1 - 1.5\sin(t)\cos(t) \\ -1 - 1.5\sin(t)\cos(t) & -1 + 1.5\sin^2(t) \end{pmatrix} \tag{4.19}$$

The eigenvalues of this periodic $A(t)$ are constant with negative real components: $\lambda = -0.25 \pm 0.6614j$. The state transition matrix for this system, however, demonstrates that the system is not stable, as it has exponentially growing solutions:

$$x(t,0) = \begin{pmatrix} e^{t/2}\cos(t) & e^{-t}\sin(t) \\ -e^{t/2}\sin(t) & e^{-t}\cos(t) \end{pmatrix} \tag{4.20}$$

The Floquet transition matrix on the other hand has eigenvalues: $\lambda = (0.002,\ 23.008)$. The magnitude of the largest eigenvalue is well over 1, indicating that the system is unstable.

Floquet decomposition was utilized to examine the longitudinal forward flight *Drosophila* dynamics previously characterized using LTI stroke-averaged techniques. Figure 4.14 shows a homogeneous response for a perturbation in heave velocity. The distinction between the LTP and LTI models is evident in the higher definition within wing strokes, especially for pitch rate. The two models are initially close but will begin to diverge as the responses progress. This is not necessarily due to modeling error; the cause is the systems inherent instability due to the pair of oscillatory modes in the right half-plane. The stability as determined by Floquet theory agrees with this result, since $\max_k (\|\lambda_k(Q)\|) = 1.0586 > 1$. Because the system is unstable, small differences between the LTI and LTP models will cause a divergence as time progresses.

The LTI forward flight Drosophila system can be stabilized by closing the loop with state feedback. To model the LTP system, the closed-loop system matrix, A_{CL},

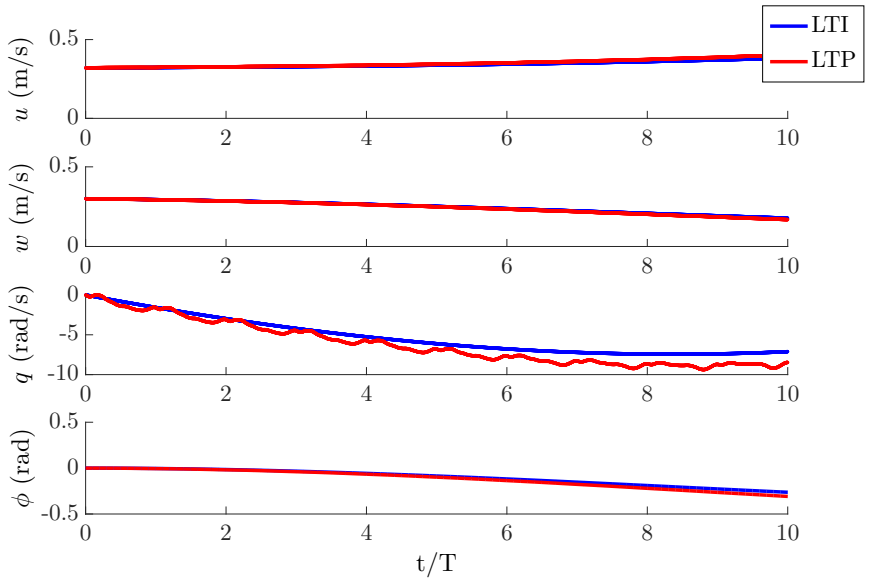


Fig. 4.14: LTI and LTP initial condition responses for fast forward flight *Drosophila* dynamics with an initial vertical velocity, showing 10 wing strokes (about 0.05 seconds). The LTP model contains more information on scales between wing strokes, evident here in the higher definition of the pitch rate response.

is created using the time-varying $A(t)$ and $B(t)$, and constant gain matrix K.

$$A_{\mathrm{CL}}(t) = A(t) - B(t)K \tag{4.21}$$

The gains were determined using LQR methods for full state feedback. The stability of the LTP system is guaranteed, since $\max_k \|\lambda_k(Q_{\mathrm{CL}})\| = 0.9775 < 1$. Figure 4.15 shows the closed loop LTI and LTP systems using the same gains, for the same initial condition in Figure 4.14, but for many more time periods. The LTI response is fairly close to the LTP, with the most variation occurring in pitch and pitch rate. The variation between the LTI and LTP models is expected to more significantly affect the vehicle dynamics for larger flapping wing vehicles with flapping frequencies closer to the speed of the rigid body dynamics, such as those on the avian scale.

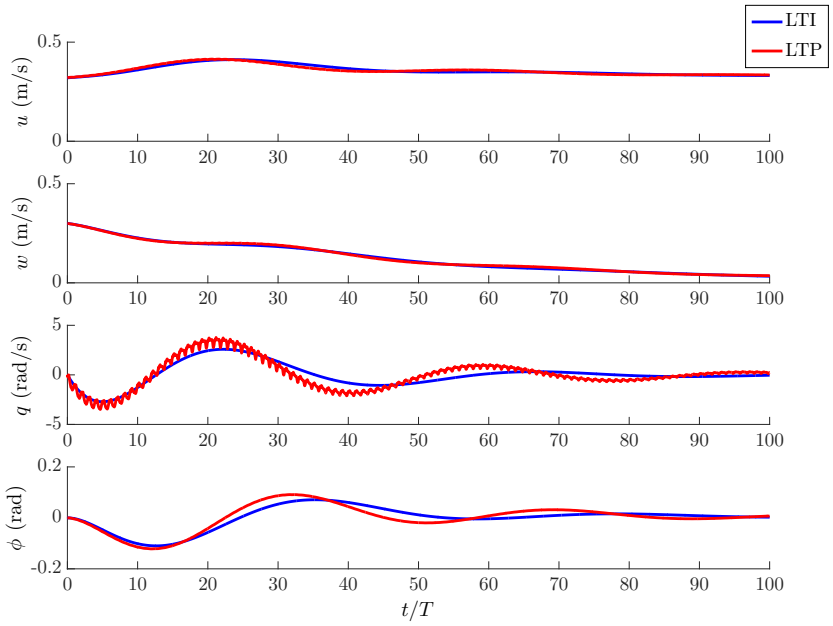


Fig. 4.15: LTI and LTP initial condition responses for closed loop forward flight *Drosophila* dynamics over 100 wingstrokes (about 0.5 seconds). Full state feedback and LQR gains were utilized for closing the loop and stabilizing the system. The LTI characterization is close to the LTP model for this small vehicle with fast flapping frequency.

4.4 Summary

This chapter describes reduced-order modeling of flapping wing vehicle dynamics and applies the methods to hovering and forward flying *Drosophila*. Non-linear rigid body equations are linearized about either reference flight condition using small perturbation theory. By estimating aerodynamic loads with respect to state and control input perturbations from the reference condition, stability and control derivatives are found. The differential equations are periodic in T, the flapping period. They can be made time invariant under the assumption that the forcing frequency from the flapping wing aerodynamic loads is much higher than the frequency of the dynamical motion. In this case, only stroke-averaged loading is important to the dynamics of the vehicle.

A linear time invariant (LTI) model is presented for hovering and forward flight *Drosophila* using multiple aerodynamic methods. A validated quasi-steady aerodynamic model would save vast amount of computational and experimental expense for dynamical modeling of flapping wing flight. In longitudinal flight, the system modal structure is similar to other hover-capable vehicles, in that slow subsidence heave motion is largely decoupled from unstable pitching-surging motion. The quasi-steady model is able to accurately model the longitudinal flight dynamics in all cases, against computational results from the IBINS CFD solver, and experimental results from RoboFly.

Quasi-steady estimates of lateral-directional flight model are inconclusive how-

ever, as they do not match the computational results and RoboFly is not currently capable of all lateral-directional motion required for dynamical modeling. This may suggest that the changes in spanwise flow due to lateral-directional state perturbations must be more accurately modeled by a quasi-steady technique. Alternatively, the inconsistency could result from numerical issues: the stability derivatives in question are very close to zero, and the eigenstructure changes dramatically when the sign on the derivative is changed.

The time-invariant assumption is tested against a time-periodic model using Floquet decomposition. The stability and control derivatives in this case are periodic functions of time. Stability requirements are defined for time-periodic systems and verified for the flapping wing case. The LTP model gives more resolution on the within-wingstroke dynamics, but follows the LTI model closely. A full-state feedback model-based control scheme based off the LTI system was shown to be effective for the LTP dynamics as well.

An assumption is made during this linearization that the vehicle is in equilibrium flight; that it is trimmed for that particular flight condition around which the linearization occurs. This can be difficult to simulate for an insect, as the mass properties are difficult to ascertain. Each insect has a variable mass, and the flight capture of kinematics discussed in the previous section does not give knowledge of which insect in the flight arena was captured, and therefore the mass properties remain unknown. Moreover, the methodology utilized here to compare aerodynamic methodologies does not allow a trimmed flight to be used across all the

linearized models. The aerodynamic load estimate changes between the method, and a trimmed vehicle would be forced to change the baseline wing kinematics, thus preventing a proper comparison of the aerodynamic models. Given the goal for this work is comparison of the flight dynamic models between the three aerodynamic estimates, the choice was made to disregard the trim requirement for equilibrium flight to focus on the differences in the flight models due to aerodynamics.

Chapter 5: Control Input Modeling

The previous chapter described reduced-order modeling efforts of homogeneous flapping wing flight. This chapter focuses on efforts to model flapping wing control inputs. Small perturbation theory is again used to describe linear deviations in aerodynamic forcing from forward flight reference flight conditions. Biologically-motivated control inputs are discussed first, followed by analysis on their effectiveness using reachability metrics, and then a discussion of a more general framework for selecting flapping wing control inputs that maximize the platform performance.

5.1 Biologically-Motivated Input Modeling

Perturbation in the reference wing kinematics yield changes to the aerodynamic loads from the reference condition similar to perturbations in state from the previous chapter. The control derivatives that constitute the control matrix, B, in Equation 4.12 are the linear regressions of stroke-averaged changes to these loads.

For the biologically-motivated control inputs described in Chapter 2, the input vector for longitudinal flight is $\mathbf{u} = [\delta_{\phi_{\max}},\ \delta_{\phi_{\text{off}}},\ \delta_\beta,\ \delta_f]^T$, giving the control matrix

for the LTI system:

$$B = \begin{pmatrix} X_{\phi_{\max}} & X_{\phi_{\text{off}}} & X_\beta & M_f \\ Z_{\phi_{\max}} & Z_{\phi_{\text{off}}} & Z_\beta & M_f \\ M_{\phi_{\max}} & M_{\phi_{\text{off}}} & M_\beta & M_f \\ 0 & 0 & 0 & 0 \end{pmatrix} \tag{5.1}$$

Figure 5.1 shows the variation of loads due to stroke amplitude throughout the wingstroke. The stroke-averaged loads due to perturbation in each control input are shown in Figure 5.2. As with the longitudinal stability derivatives for forward flight, the quasi-steady loads are offset from the CFD estimates, but the linear change due to perturbation from the reference condition matches well.

The system identified in the previous chapter (see Figures 4.7 & 4.9) shows that the longitudinal dynamics are pitch-dominated, due to the unstable oscillatory modes in the right half plane. It can be inferred that the control inputs that impact the pitching moment, M, will greatly influence this unstable motion, and thus the longitudinal motion of the vehicle as a whole. The stroke offset input, $\delta_{\phi_{\text{off}}}$, shows the most promise in Figure 5.2, due to the high magnitude of $M_{\phi_{\text{off}}}$. Both the stroke amplitude, $\delta_{\phi_{\max}}$, and frequency, δ_f, contribute to the heave motion.

Evaluating the stability derivatives directly gives some intuition for the effect of each control input, but a better metric would take the vehicle dynamics into account. For example, forcing a flight mode that is heavily damped will lead to less impact than forcing a less damped or unstable flight mode. The following section will describe a metric for evaluation of control inputs that includes the vehicle dynamics.

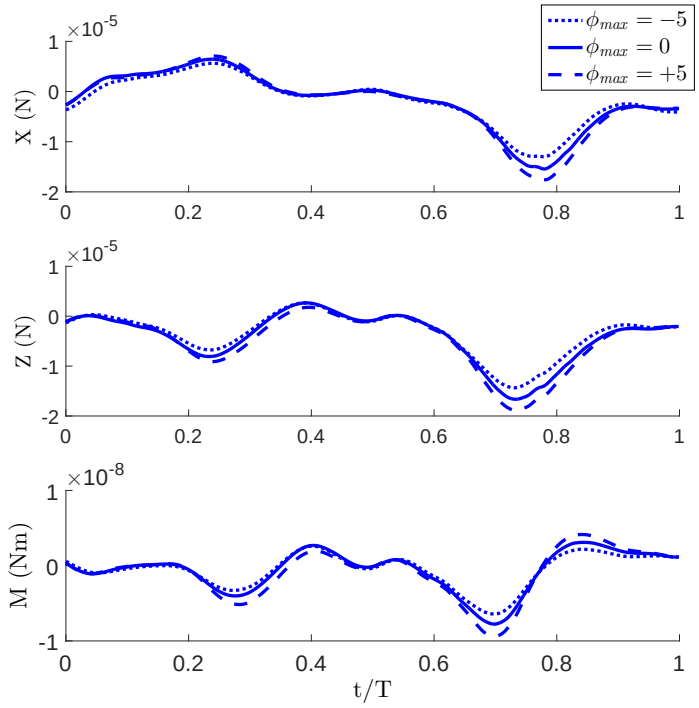


Fig. 5.1: Aerodynamic loads for several perturbations of $\delta_{\phi_{\max}}$ during a wingstroke of forward flying *Drosophila* estimated via IBINS CFD. The wing stroke begins with the upstroke followed by the downstroke. The wing encounters higher local velocity on the downstroke than the upstroke due to incoming flow, leading to larger aerodynamic loading during the downstroke. Increasing $\delta_{\phi_{\max}}$ amplifies loads throughout the stroke.

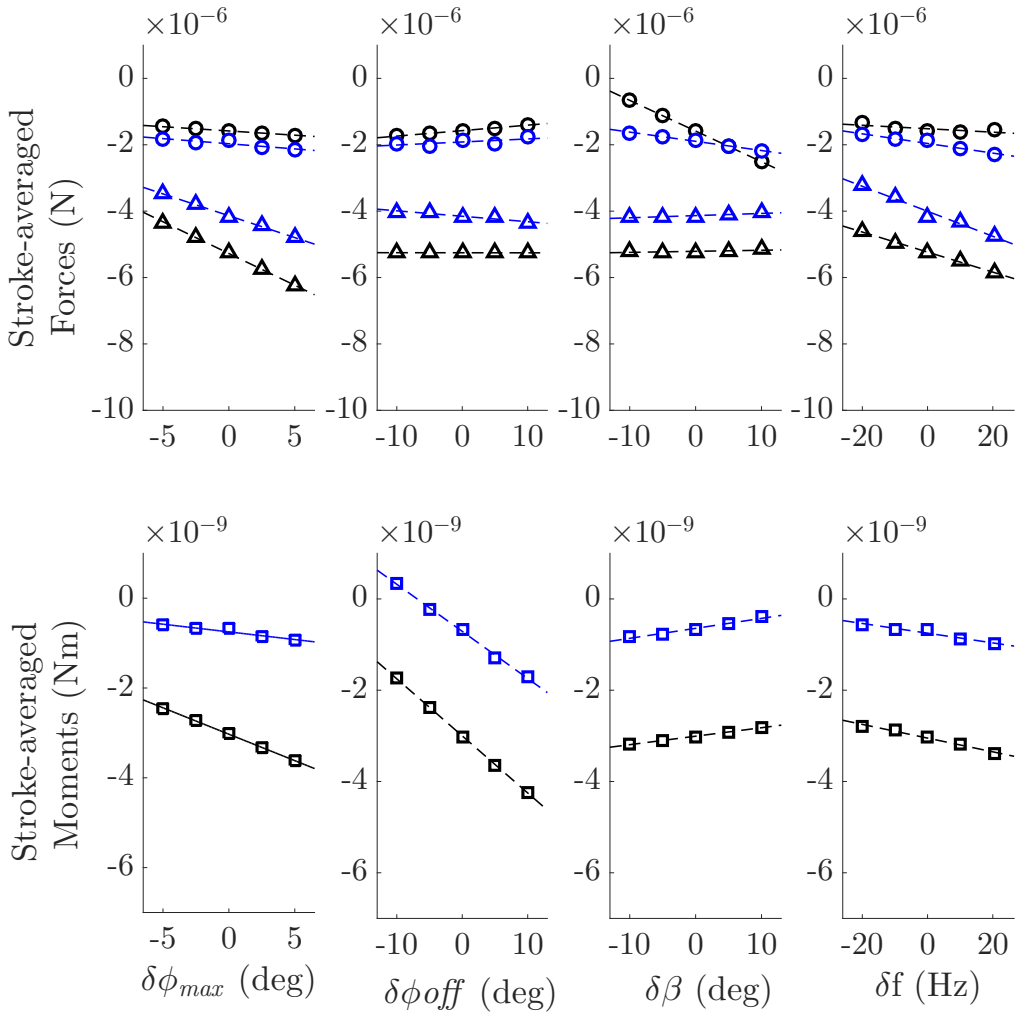


Fig. 5.2: Stroke-averaged longitudinal loads due to perturbations in control inputs from the forward flight reference condition. Circles show X, triangles Z, and squares M; results from the quasi-steady model in black, CFD in blue. The resulting linear regressions are shown as dashed lines of the corresponding color.

5.2 Reachability Analysis

5.2.1 The Reachability Gramian

To evaluate the effectiveness of control inputs, we use the flight dynamics model developed in Sections 2.1 and 2.2 to consider the effect of the all unit norm control inputs on the resulting motion of the insect. To do so, the control theoretic framework of [76] is applied to quantify the reachable states for a given set of inputs and analyze the fruit fly forward flight dynamics model developed in Section 3. Controllability as an application of operator theory is the basis for determining the reachable configurations under a class of inputs. The expressions for reachable states may then be used to solve a least-squares optimization problem over all possible function inputs. As a consequence of the cross coupling and rotational dominance of the forward flight model, the controllability rank test indicates that the system is controllable with any of the control inputs previously defined. Given the stringent size, weight, and power demands on small air vehicles, a more refined analysis of the relative controllability of each input is justified.

To do accomplish this, a controllability operator Ψ_c is introduced, which operates on input $u(t) \in \mathcal{U} = \mathcal{L}_2^p[0, \infty)$to $\mathcal{X}$. The operator takes a time history in $\mathcal{U}$ and outputs a final state in $\mathcal{X}$ as

$$\Psi_c u = \int_{-\infty}^{0} e^{-A\tau} B u(\tau)\, \mathrm{d}\tau. \tag{5.2}$$

We define the reachable configuration space as the reachable states under a unit

norm input, as

$$\{\Psi_c u : u \in \mathcal{L}_2^p[0,\infty) \text{ and } \|u(t)\| \leq 1\}, \tag{5.3}$$

where unit norm is measured in total power required (inertial and aerodynamic). This reachable configuration space is equivalent to the ellipsoid described by

$$\mathcal{E}_c = \left\{ W_c^{\frac{1}{2}} x_c : x_c \in \mathcal{X} \text{ and } ||x_c|| \leq 1 \right\}. \tag{5.4}$$

$\mathcal{E}_c$ defines an ellipse in $\mathbb{C}^n$ whose geometric properties are determined by the infinite-time reachability gramian W_c for the LTI system,

$$W_c \;=\; \Psi_c \Psi_c^* \;=\; \int_0^\infty e^{A\tau} B B^* e^{A^*\tau}\, d\tau \;\geq 0 \tag{5.5}$$

for stable systems. For unstable systems, the generalized gramian [89,90] must be used, defined as

$$W_c = \frac{1}{2\pi} \int_{-\infty}^{\infty} (j\omega - A)^{-1} B B^T (j\omega - A^T)^{-1}\, \mathrm{d}\omega. \tag{5.6}$$

The gramian W_c defined in Equation 5.6 collapses to the form in Equation 5.5 if A is stable.

A suitable metric for reachable space in $\mathcal{E}_c$ is given by the Frobenius norm of $W_c^{\frac{1}{2}}$.

$$||W_c^{\frac{1}{2}}||_F = \sqrt{\text{trace}\left[(W_c^{\frac{1}{2}})^* W_c^{\frac{1}{2}}\right]}. \tag{5.7}$$

Additionally, directionality of the gramian can be beneficial in determining the state directions most impacted by a particular control input. The principle axes of the reachability ellipsoid $\mathcal{E}_c$ represent the directions in the state space that take the

least control energy and are easiest to reach for the system. These axes are given by the eigenvectors of the reachability gramian W_c and their lengths are given by its eigenvalues.

5.2.2 Reachability Analysis of Biologically-Motivated Control Inputs

The gramian metric allows quantification of the effect of each control input over time, resulting from the effect of the control input on the system dynamics. The Frobenius norms of the reachability gramian for each control input is shown in Figure 5.3. The unstable oscillatory motion does in fact dominate the effectiveness of each control input. Stroke offset provides the most reachability for this *Drosophila* system. The stroke plane tilt also provides significant response, while the effect of amplitude and frequency is minimal.

By examining the reachable space defined by the reachability ellipsoid $\mathcal{E}_c$, we can also gain intuition for state space directionality of each control input. The ellipsoid exists in the four-dimensional longitudinal state space ($\mathbf{x} = [u, w, q, \theta]$), but can be projected onto two dimensions, and shown as an ellipse for legibility. The projected ellipse is given by transformation $\tilde{W}_c = MW_cM^T$, where M is a matrix composed of the desired basis vectors.

Figure 5.4 shows reachability ellipsoid projected onto $[u, w]$ and $[q, \theta]$ planes for each of the four example control inputs. Each ellipse represents the maximum reachable states given by a unit norm control input composed exclusively of that input. The reachable space given by a unit norm control input generated by a

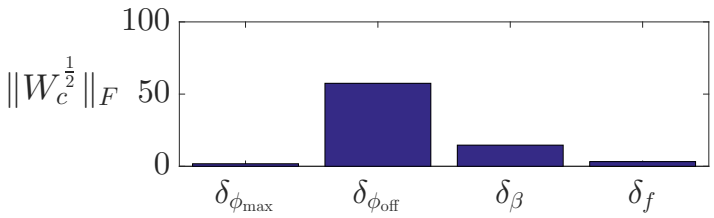


Fig. 5.3: Frobenius norm of the reachability gramian for each of the example control inputs.

combination of those control inputs is shown as a dotted black line. Figure 5.4 suggests that the majority of the reachable space is due to the influence of the stroke offset control input ($\delta_{\phi_{\text{off}}}$); adding the other three inputs allows only slightly more reachable states.

Each control input aligns with the dominating unstable motion in u and q, with the notable exception of stroke amplitude ($\delta_{\phi_{\max}}$). Amplitude offers far less reachable space than the stroke offset, or even stroke plane tilt; however, its alignment along heave motion gives the system ability to operate vertically independent of the unstable pitching/surging motion. Frequency modulation (δ_f) activates the pitching/surging motion along with heave. Thus alterations to amplitude, rather than frequency, would be more effective in generating heave motion independent of any other motion. Previous works have shown that free flying *Drosophila* in fact use a combination of amplitude and frequency modulations to follow vertical trajectories. [91–93]

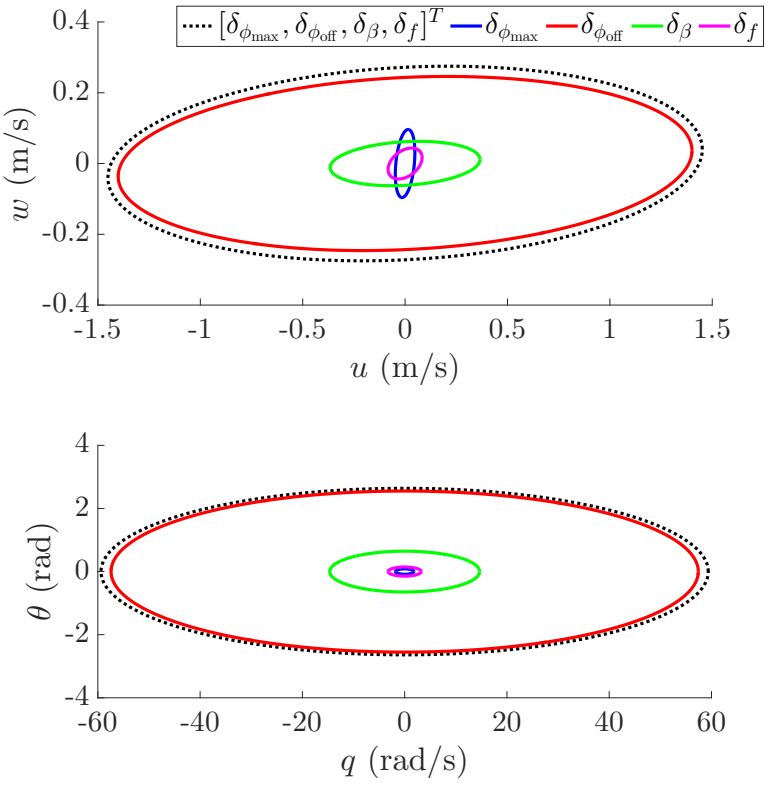


Fig. 5.4: Example control input reachability ellipsoids projected onto the $[u, w]$ and $[q, \theta]$ planes. Each ellipsoid corresponds to system reachability given unit energy of that input ($\|\mathbf{u}(t)\| = 1$).

5.2.3 Power-Normalized Reachability

The reachability metric describes the reachable state space for a vehicle given unit control energy. The metric is useful when considering which control input is most effective at driving a system in various state directions. By augmenting the metric with the power consumed by each control input, the most power-efficient control inputs can be determined.

A description of the estimation for power consumed as a function of both inertial and aerodynamic power is given in Chapter 3. The aerodynamic power as it varies over a wing stroke is shown in Fig. 5.5. Note that the stroke presented here begins with the upstroke, followed by the downstroke, where the power required is much greater due to the effect of the freestream velocity. The total power required is a combination of this aerodynamic power and the inertial loading calculated according to Eq. 3.7 and Eq. 3.11. Consulting Eq. 3.7, the asymmetry in the aerodynamic power required between the two half strokes means the inertial loading contributes the majority of the power required during the decelerating portion of the upstroke. The decelerating portion of the downstroke will require much more inertial power to completely mitigate the aerodynamic power.

The stroke-averaged total power required is linearized in the same method as the aerodynamic loading to find the linear change in total power required, shown in Fig. 5.6. We define the power matrix as the diagonal matrix comprised of the power derivatives, $E = diag\{P_{\delta_{\phi_{\max}}}, P_{\delta_{\text{off}}}, P_{\delta_\beta}, P_{\delta_f}\}$. The control load available with a single

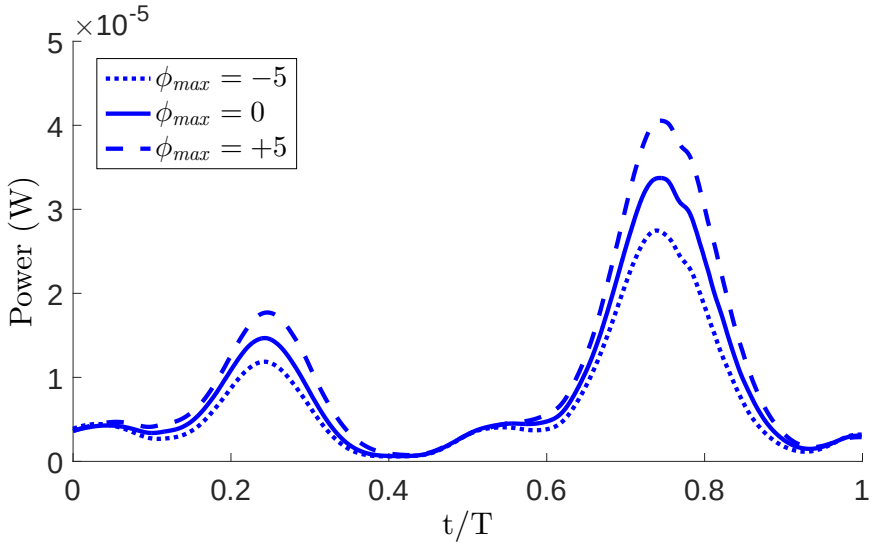


Fig. 5.5: Aerodynamic power required during a single wingstroke with varying stroke amplitude. The wing stroke begins with the upstroke followed by the downstroke. The wing encounters higher local velocity on the downstroke than the upstroke due to incoming flow, resulting in larger aerodynamic power required during the downstroke.

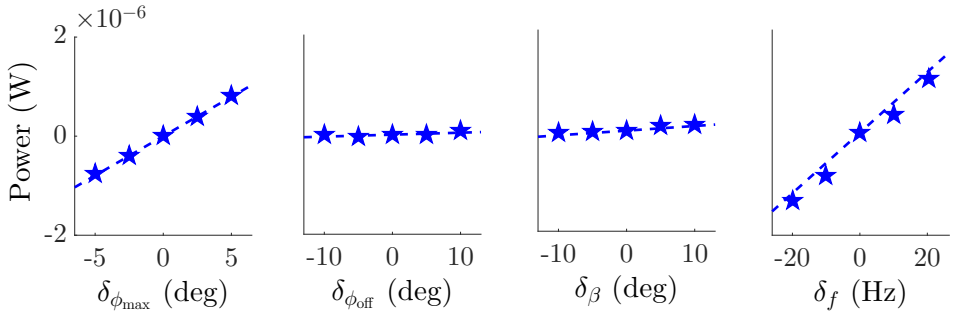


Fig. 5.6: Stroke-averaged power required with perturbations to control inputs. This average power is a combination of both aerodynamic and inertial power; see Equation 3.7.

$X^*_{\delta_{\phi_{\max}}}$	$X^*_{\delta_{\phi_{\text{off}}}}$	$X^*_{\delta_\beta}$	$X^*_{\delta_f}$
-0.198	2.30	-3.05	-0.245
$Z^*_{\delta_{\phi_{\max}}}$	$Z^*_{\delta_{\phi_{\text{off}}}}$	$Z^*_{\delta_\beta}$	$Z^*_{\delta_f}$
-0.830	-4.18	0.708	-0.640
$M^*_{\delta_{\phi_{\max}}}$	$M^*_{\delta_{\phi_{\text{off}}}}$	$M^*_{\delta_\beta}$	$M^*_{\delta_f}$
-370	-4.54e4	4.12e3	-315

Tab. 5.1: Power normalized control derivatives. Each derivative is scaled to show the control force or moment obtainable with $1\mu J$.

unit of power is easily obtained by evaluating a power normalized control matrix, $B^* = BE^{-1}$. For example, the first element of B^* is $X^*_{\delta_{\phi_{\max}}} = X_{\delta_{\phi_{\max}}} P^{-1}_{\delta_{\phi_{\max}}}$ which describes the x-direction load that the stroke amplitude control input is capable of producing with $1W$ of power. The power normalized control inputs are listed in Table 5.1.

The power normalized derivatives allow an evaluation between the power effectiveness of control inputs in generating direct aerodynamic loads. At least for the forward flight kinematics presented here, the results in Table 5.1 suggest that kinematic changes to stroke offset and stroke plane tilt will be preferred by an insect interested in conserving power. Changes to stroke plane tilt are the most power-effective for direct forcing fore-aft translation, while stroke offset is the most effective input for heave translation and pitching moment production.

Although the above results suggest that stroke amplitude and frequency changes to wing kinematics consume a much greater amount of power than stroke offset or stroke plane tilt, these results do not preclude the utility of changes in stroke am-

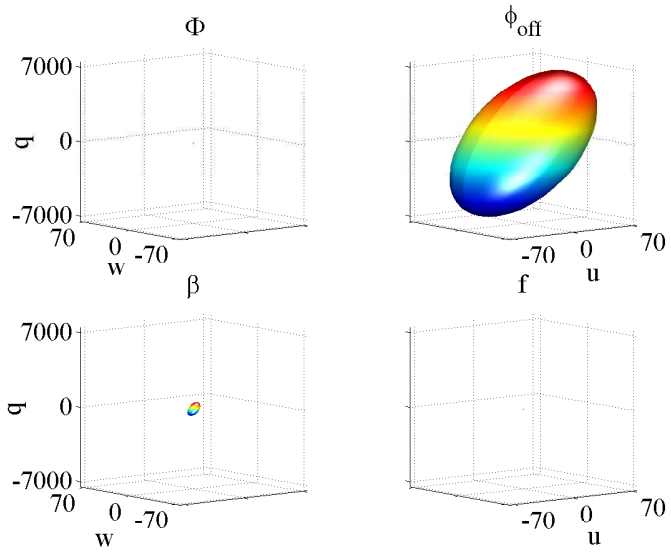


Fig. 5.7: Power normalized reachability ellipsoids for each control input show that stroke offset is an effective control term with lowest energetic cost.

plitude or frequency in insect control. Kinematic changes to stroke amplitude and frequency may not be effective in terms of power regulation, but could remain an integral part of the control input ensemble because the maximum load generated by these inputs may be greater than the load generated by less power hungry kinematic changes. For example, stroke offset may require much less power than stroke amplitude to produce a small amount of heave force, but changes to stroke amplitude is capable of generating much greater force. Lehmann and Dickinson (1997) [85] noted stroke amplitude changes by *Drosophila* responding to vertical motion, and later found that frequency in particular is varied by species of *Drosophila* to account for changes in weight among species [74].

Consideration of the direct control authority given by each control input gives some intuition for the effectiveness of each input over individual states. However,

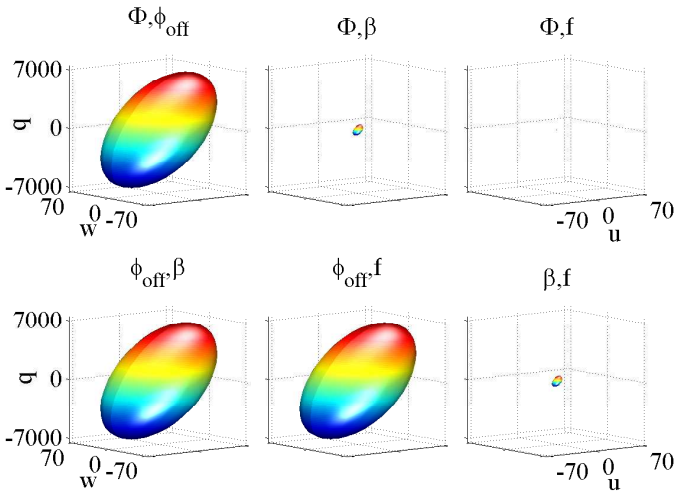


Fig. 5.8: Power normalized reachability ellipsoids for pairs of control inputs again show the great effectiveness of the stroke offset term.

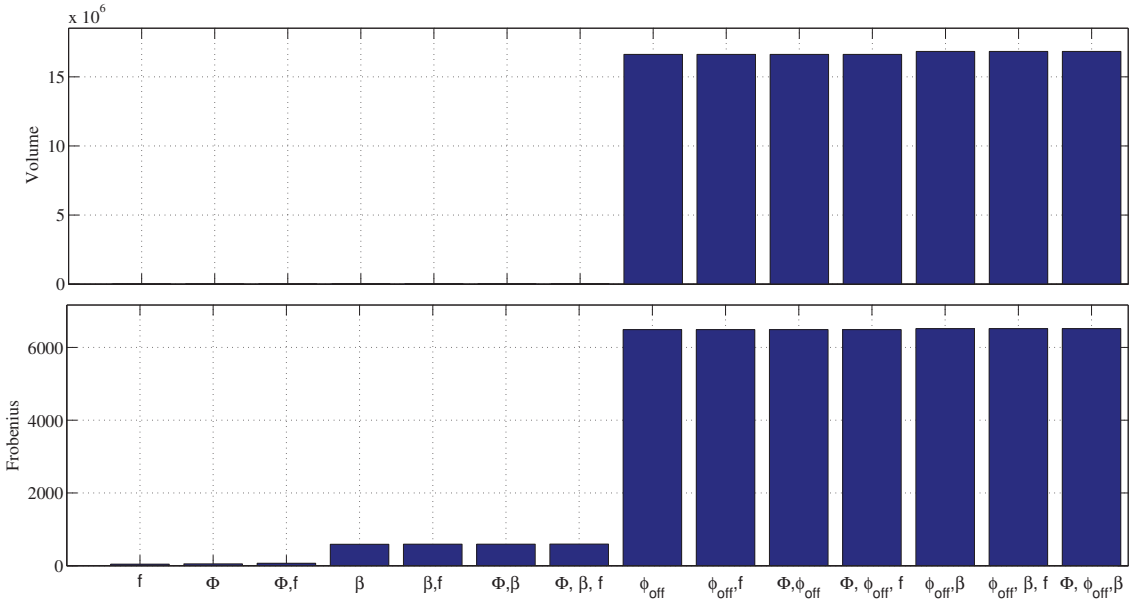


Fig. 5.9: The determinant and Froebinius norms of the reachability ellipsoid quantify the reachable space for each individual control term or set thereof.

given the coupled nature of these equations in forward flight, this process does not paint the whole picture. The reachability analysis considers input time histories corresponding to energy cost. This is a measure of the agility or maneuverability of the aircraft in the general sense: we ask how many vehicle states are reachable, with a specific amount of control energy.

The current analysis considers the reachable state-space for input energy not exceeding 1μJ. The reachability ellipsoids for each input are shown in Figure 5.7, which shows the comparatively low energetic cost of using stroke offset. In practice, more than one input is used to actuate an insect or micro aerial vehicle, thus the consideration of combinations of inputs has a physical motivation. Figure 5.8 shows the reachability ellipsoids under the same 1 μJ energetic contours but with pairs of inputs. Again, the value of including a stroke offset term is evident.

These size measures are shown in Fig 5.9. Again, the much higher power efficiency of stroke offset as a control input is indicated. The Frobenius norm shows that the reachable configuration space is with stroke offset and stroke plane inclination (the two most power efficient controls) is 93 times larger than a feedback strategy using amplitude and frequency (the least power efficient controls).

Previous research [85, 94–96] has provided experimental evidence for the use of stroke amplitude and frequency for insect control of flight forces. There are a number of competing objectives that could provide a compelling reason to choose power-hungry control inputs in spite of the inputs' power normalized effectiveness. Nonlinearities resulting from control input saturation could be driving the choice.

A power hungry control input could be chosen over an efficient input if the load required for a maneuver exceeds the capabilities of the efficient input.

5.3 Control Input Reduction

5.3.1 Defining a More General Set of Flapping Wing Control Inputs

The previous section considered a set of four biologically motivated wing kinematic control inputs for a flapping wing system. A wide array of choices exist beyond these four, however. Studies of free flight *Drosophila* suggest that they are capable of enacting impressive maneuvers even with small kinematic changes in a combination of the three wing kinematic angles. [97] Some studies of insects in flight have in fact shown that insects may use a "paddling" motion to generate forward acceleration. [39] Additionally, biological flyers may have structural and evolutionary limitations to kinematic inputs. So there may exist kinematic inputs that are superior to the motions seen in insects or birds.

A general set of kinematic inputs can be defined using a Fourier series of transcendental functions for each of the three wing Euler angles.

$$\delta_\phi(t) = a_0^\phi + \sum_{n=1}^{N} a_n^\phi \cos(2\pi n f t + b_n^\phi) \tag{5.8}$$

$$\delta_\zeta(t) = a_0^\zeta + \sum_{n=1}^{N} a_n^\zeta \cos(2\pi n f t + b_n^\zeta) \tag{5.9}$$

$$\delta_\alpha(t) = a_0^\alpha + \sum_{n=1}^{N} a_n^\alpha \cos(2\pi n f t + b_n^\alpha) \tag{5.10}$$

An individual control input would be defined as an individual amplitude, $a_n^{[\cdot]}$, with

a set harmonic order, n, and phase shift, $b_n^{[\cdot]}$. However, even considering just the first harmonic of the three kinematic angles with a 10 degree discretization in phase leads to a massive array of 60 control inputs. For the simple case with $N = 1$, the control vector is

$$u = \left[a_0^{\phi}, a_1^{\phi}\Big|_{b_1^{\phi}=-\pi}, ..., a_1^{\phi}\Big|_{b_1^{\phi}=\pi}, a_0^{\zeta}, a_1^{\zeta}\Big|_{b_1^{\zeta}=-\pi}, ..., a_1^{\zeta}\Big|_{b_1^{\zeta}=\pi}, a_0^{\alpha}, a_1^{\alpha}\Big|_{b_1^{\alpha}=-\pi}, ..., a_1^{\alpha}\Big|_{b_1^{\alpha}=\pi} \right]^T \tag{5.11}$$

Implementation of this many inputs on a flapping wing platform would mechanically formidable, and so gaining intuition for the intelligent selection of these kinematic control inputs could be utilized to maximize the performance of a flapping wing platform. Rigorous modeling of the control derivatives for each input is currently computationally intractable due to the large amount of inputs and the computational expense for each run. The quasi-steady aerodynamic method provides a feasible modeling option to estimate the individual control derivatives for each control input. Based on the previous modeling efforts for both perturbations in state and the biologically-motivated control inputs, confidence is given for quasi-steady method estimation of this wide array of control derivatives.

Before applying the reachability maximization to a more general set of wing kinematic control inputs, those inputs effect on the system must be identified. Three different general inputs in the form of Equation 5.11 are identified: one including only first order Fourier terms on each of the three kinematic angles, another with first and second order Fourier terms, and finally an input with first through third order fourier terms. First order terms occur at the same frequency as the wing

stroke, second order at twice the frequency, and third order at triple. The inputs also include zeroth order terms – offsets in the average position of each kinematic angle. The phase angles are discretized at 10 degrees for each of the inputs. Thus, the first input vector (defined here $\mathbf{u}_{\mathrm{n=1}}$) contains 3 zeroth order terms and 57 first order terms, for a total of 60 individual kinematic inputs. Including the second order Fourier terms makes the second input ($\mathbf{u}_{\mathrm{n=2}}$) a vector of 117 inputs. The third-order input vector ($\mathbf{u}_{\mathrm{n=3}}$) contains 154 inputs.

5.3.2 Energy-Optimizing Input Reduction

After estimating the wide control matrix, a reduction to fewer kinematic inputs is desirable. A simple reduction of a wide matrix is possible using singular value decomposition (SVD). However, an SVD reduction does not consider the homogeneous dynamics of the flapping wing system, and as discussed in the previous sections, the effectiveness of control inputs is dependent on these inherent dynamics. The gramian metric provides an opportunity to develop a control input reduction methodology that maximizes the reachability of the vehicle.

Define the problem as follows. Beginning with the system of equations

$$\dot{\mathbf{x}}(t) = A\mathbf{x}(t) + B\mathbf{u}(t) \;\; , \;\; A \in \mathbb{R}^{n\times n} \;\; , \;\; B \in \mathbb{R}^{n\times m} \tag{5.12}$$

where $m >> n$.

We would like to choose a single input, $\tilde{u}(t)$ that consists of a linear combination of inputs $\mathbf{u}(t)$. This can be accomplished by introducing the unit norm vector

$\mathbf{q}$ into the set of equations as follows

$$\dot{\mathbf{x}}(t) = A\mathbf{x}(t) + B\mathbf{q}\tilde{u}(t) \ \ , \ \ \|\mathbf{q}\| = 1 \ \ ; \ \ \mathbf{q} : \mathbb{R} \rightarrow \mathbb{R}^m \tag{5.13}$$

To maximize the system state energy, while minimizing the input energy, define the following cost function as follows

$$J = \max_{q} \sup_{\tilde{u} \neq 0} \frac{\|\mathbf{x}\|^2_{\mathcal{R}^n}}{\|\tilde{u}\|^2_{L_2(-\infty,0]}} \tag{5.14}$$

The Lebesgue 2-space, L_2, defines the space of signals with finite bounded energy. The norm $\|\mathbf{x}\|^2_{\mathcal{R}^n}$ is the energy of states (in the system state space $\mathcal{R}^n$), while the norm $\|\mathbf{u}\|^2_{L_2(-\infty,0]}$ is the energy of past inputs (on the L_2 space before $t = 0$). Thus, the cost function J in Eq. 5.14 minimizes the past control energy required while maximizing the state energy of the system.

The minimum input energy required to reach a given state at time $t = 0$ ($\mathbf{x}_0$) can be described using the reachability gramian defined in equation 5.5. [98]

$$\inf_{u} \|\mathbf{u}\|^2_{L_2(-\infty,0]} = \mathbf{x}_0^T W_c^{-1} \mathbf{x}_0 \tag{5.15}$$

The cost function then reduces to the following

$$\begin{aligned} J &= \max_{q} \max_{\mathbf{x}_0} \frac{\mathbf{x_0}^T \mathbf{x_0}}{\mathbf{x_0}^T W_c^{-1} \mathbf{x_0}} \\ &= \max_{q} \max_{\mathbf{x}_0} \mathbf{x_0}^T W_c \mathbf{x_0} \ \ ; \ \ \|\mathbf{x_0}\| = 1 \end{aligned} \tag{5.16}$$

Douglas et al. (2004) describe a methodology to find $\mathbf{q}$ using a pair of eigenvalue problems. [99] This process is outlined as follows:

Step 1: Find maximizing $\mathbf{x_0}$ for the full input system by solving

$$W_c \mathbf{x_0} = \lambda_{\max} \mathbf{x_0}.$$

Step 2: Find the maximizing $\mathbf{q}$ for the initial state direction $\mathbf{x_0}$

$$B^T X B \mathbf{q} = \lambda_{\max} \mathbf{q} \qquad \text{where } X = \int_{-\infty}^{0} e^{-A^T \tau} \mathbf{x_0} \mathbf{x_0}^T e^{-A\tau} d\tau.$$

Step 3: Find the reduced input reachability gramian for this $\mathbf{q}$,

$$\tilde{W}_c = \int_{-\infty}^{0} e^{-A\tau} B \mathbf{q} \mathbf{q}^T B^T e^{-A^T \tau} d\tau.$$

Step 4: Find norm of the reduced input reachability gramian,

$$\|\tilde{W}_c\| = \sqrt{\lambda_{\max}\left(\tilde{W}_c\right)}\,.$$

Step 5: Return to Step 2 and repeat until $\|\tilde{W}_c\|$ converges.

The resulting vector $\mathbf{q}$ is the optimal linear combination of control inputs according to the cost function in Eq. 5.14. This allows use of a single scalar input $\tilde{u}$ that combines m inputs from the original control vector $\mathbf{u}$. The second, third, etc. most effective linear combinations can be found by repeating the process with a reduced control matrix, $B_{\text{red}} = B(I - \mathbf{q}\mathbf{q}^T)$, which is a subtraction of the projection of $\mathbf{q}$ on the control matrix.

The method is only applicable for a stable system. An unstable system's output energy would grow unbounded, and so the problem outlined above is ill-defined for such systems. Because flapping wing dynamics are unstable, the method will not work unless some feedback is applied to stabilize the system.

5.3.3 Results for Forward Flying Insect

The above method for reducing the number control inputs with minimal loss in system reachability is applied to the forward flying *Drosophila* longitudinal model. A reduced input from the four biologically-motivated control inputs is discussed first as a proof of concept, then followed by application to the general control inputs, where an input reduction is shown to be useful for input selection.

Before optimal control input strategies can be investigated, the inherent system dynamics must be stabilized. Pitch rate feedback is added to the longitudinal system. The closed loop stability matrix is written as $A_{\mathrm{CL}} = A - BK$, with

$$K = \begin{pmatrix} 0 & 0 & 0 & 0 \\ 0 & 0 & 0 & 0 \\ 0 & 0 & k_q & 0 \end{pmatrix} \tag{5.17}$$

where k_q is the gain on the pitch rate feedback. Pitch rate feedback control is biologically motivated, as *Dipteran* insects utilize underdeveloped hind-wings, called halteres, to quickly sense rotation rates. [100] It is suspected that this rate information is quickly fed to the wing hinge actuation system to provide high frequency pitch rate feedback. [45]

Biologically-Motivated Inputs

The optimal energy technique is used first for the biologically-motivated control inputs ($\mathbf{u} = [\delta_{\phi_{\max}}, \delta_{\phi_{\mathrm{off}}}, \delta_\beta, \delta_f]^T$). A combination of the four kinematic inputs is chosen that is energy-optimal, such that it maximizes the reachable state space per unit of control energy. The quasi-steady model is used for these results.

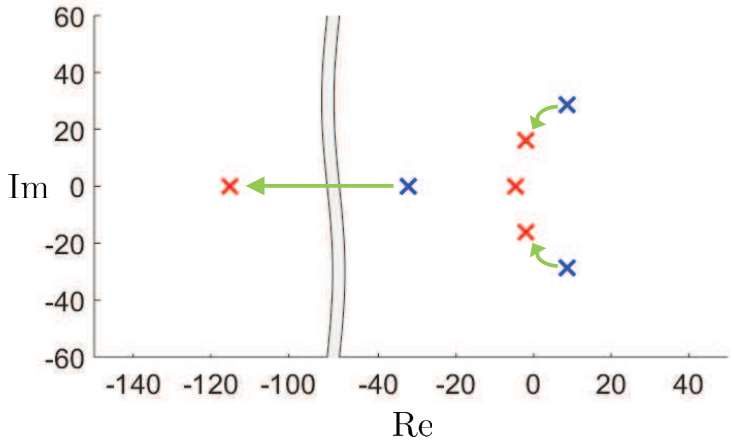


Fig. 5.10: Pitch rate feedback is added to stabilize the longitudinal modes for the fast forward flying *Drosophila*.

For ease of presentation, the state space can be scaled by a scaling matrix. In this case, the system is scaled such that the lengths in the state space are in centimeters instead of meters. The scaled matrix is $A_{\text{scl}} = S_x^{-1} A S_x$, where

$$S_x = \begin{pmatrix} 1e^{-2} & 0 & 0 & 0 \\ 0 & 1e^{-2} & 0 & 0 \\ 0 & 0 & 1 & 0 \\ 0 & 0 & 0 & 1 \end{pmatrix} \tag{5.18}$$

The control matrix should also be scaled, in this case by the largest expected value of the individual control input. Then, $B_{\text{scl}} = S_x^{-1} B S_u$, where

$$S_u = \begin{pmatrix} 5 & 0 & 0 & 0 \\ 0 & 10 & 0 & 0 \\ 0 & 0 & 10 & 0 \\ 0 & 0 & 0 & 20 \end{pmatrix} \tag{5.19}$$

Note that these scaling parameters are the same as the maximum deviation in each parameter from Figure 5.2. The amplitude maximum was selected as half of the offset because the peak to peak changes if $\delta_{\phi_{\text{max}}} = 5°$ are the same as if $\delta_{\phi_{\text{off}}} = 10°$.

Figures 5.3 & 5.4 show that stroke offset contributes most of the reachable space for the biologically-motivated inputs (the Frobenius norm of the reachability gramian using just $\delta_{\phi_{\text{off}}}$ is 96.8% of the norm from the set of all four inputs). A reachability-maximizing combination of inputs should be expected to contain a large stroke offset.

The input combination $\mathbf{q}_1$ resulting from the reachability-maximization is shown in Figure 5.11. Stroke offset is the dominant control input in the combination, which attains a Frobenius norm that is 99.9% of the possible using all inputs. The second linear combination, $\mathbf{q}_2$, shows the next most effective input after $\mathbf{q}_1$ is removed from B, and provides only 6.1% of the maximum Frobenius norm. The reachability ellipsoids for each of the linear combinations is provided in Figure 5.12.

This example suggests that the reachability-maximizing algorithm is working as expected. The optimal linear combination includes a large amount of the most effective control input ($\delta_{\phi_{\text{off}}}$), but provides more reachable space than that input alone. Note that the reachable space is largely aligned along the u and q directions; neither $\mathbf{q}_1$ or $\mathbf{q}_2$ provide input primarily along the w direction. A weakness of the reachability-maximization is that some flight modes can be neglected due to damped response in those state directions or dominant responses in other directions. In this case, heave is much less responsive than the unstable pitching/surging response. By maximizing reachability, the algorithm neglects to generate control inputs that primarily effect heave motion.

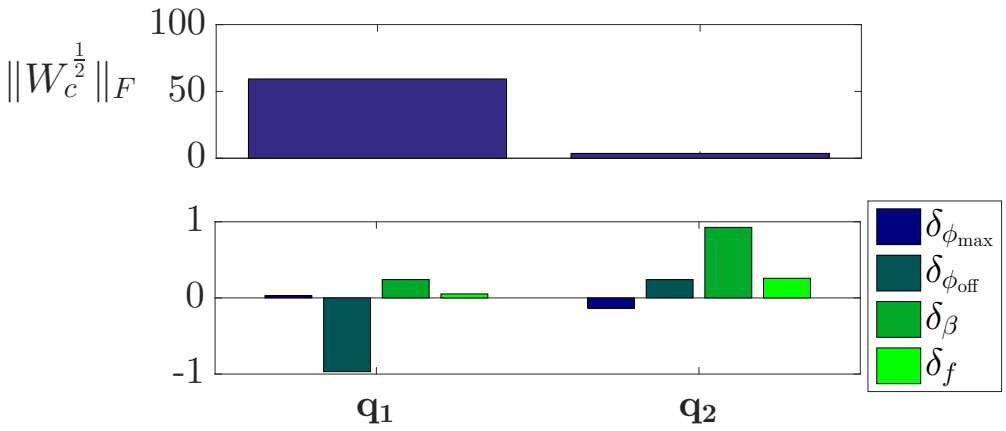


Fig. 5.11: Frobenius norm of the reachability gramian for the first two reachability-maximizing combinations of the example control inputs. The linear combination of these inputs is given below.

General Kinematic Inputs

By defining the wing kinematic control inputs in a general sense, a single control input containing many individual inputs of varying effectiveness can be combined. If the inputs are set as a 1st order Fourier series as described in Equation 5.10, and the phase is discretized by 10 degree increments, there will be a control input $\mathbf{u}(t) \in \mathbb{R}^{60\times 1}$ and the control matrix will be extremely wide, $B \in \mathbb{R}^{4\times 60}$. Three inputs are considered, each including increasing Fourier harmonics. The first input vector (defined here $\mathbf{u}_{\text{n=1}}$) contains 3 zeroth order terms and 57 first order terms, for a total of 60 individual kinematic inputs. Including the second order Fourier terms makes the second input ($\mathbf{u}_{\text{n=2}}$) a vector of 117 inputs. The third-order input vector ($\mathbf{u}_{\text{n=3}}$) contains 154 inputs. The control matrix is calculated by varying each input between -5 and 5 degrees, and calculating a linear regression through the stroke

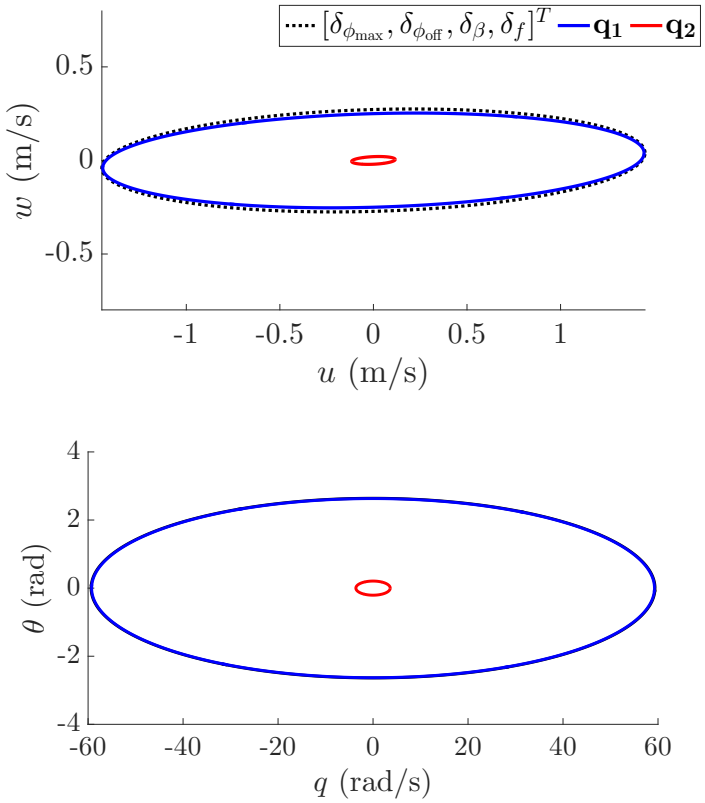


Fig. 5.12: Reachability ellipsoids for optimized example control inputs projected onto the $[u, w]$ and $[q, \theta]$ planes. Each ellipsoid corresponds to system reachability given unit energy of that input ($\|\mathbf{u}(t)\| = 1$).

averaged points, as described in Section 5.1.

The reachability-maximizing algorithm is applied to the control matrix generated by each of the three input vectors: $\mathbf{u}_{n=1}$, $\mathbf{u}_{n=2}$, and $\mathbf{u}_{n=3}$. The reachability for the most effective input combination from each of the three vectors is shown in Figure 5.13. As before, motion in u and q directions are dominant due to the underlying system dynamics, but the reachable space is dramatically larger than for the set of four biologically-motivated inputs (compare to Figure 5.12). In addition, the control inputs continue to grow in effectiveness as control options from higher frequencies are added, but state-space directionality is unchanged. This result suggests that higher degrees of maneuverability can be achieved with the inclusion of higher frequency kinematic control within the wingstroke.

Reachability-maximizing control inputs are shown in Figure 5.14. Each of the control inputs relies on large deviations in the elevation angle, along with changes to the stroke offset. Changes to amplitude are minimal, as are those to the angle of attack. Including higher frequency content changes the preferred elevation angle. When elevation is locked to the stroke frequency the elevation angle forms an oval-shape in the stroke plane. Once second order components are added the reachability-maximizing input amplifies the baseline elevation angle, resulting in kinematics that resemble a U-shape. The third order input creates a complex, double figure-8 motion in the stroke plane, while altering remarkably little in the wing pitch throughout the stroke.

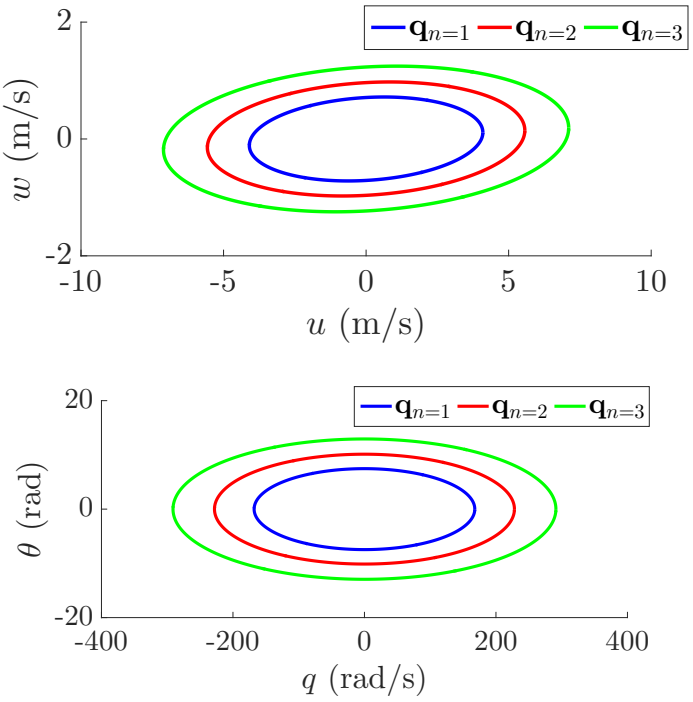


Fig. 5.13: Reachability ellipsoids for optimized general control inputs from projected onto the $[u, w]$ and $[q, \theta]$ planes.

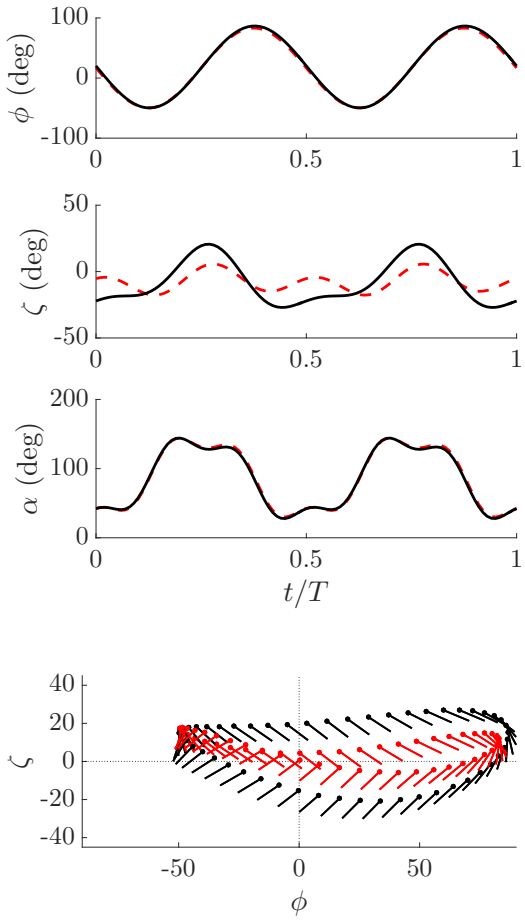


Fig. 5.14: Kinematics resulting from the reachability-maximizing linear combination of the first harmonic, $\mathbf{u}_{n=1}$. Baseline kinematics are in red, reachability-maximizing control input ($\mathbf{q}$) in black.

5.3.4 Discussion

Maneuverability may be key to survival for insects such as *Drosophila* for predator evasion or reproductive success. Other insects such as Dragonflies rely on high maneuverability for predatory behavior. A significant amount of research has been devoted to observation of dipteran kinematic inputs to effect flight maneu-

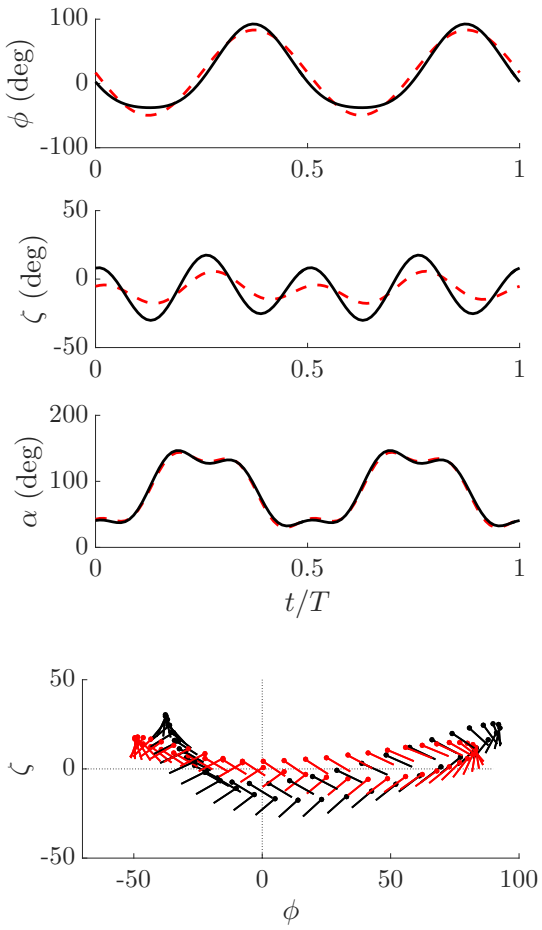


Fig. 5.15: Kinematics resulting from the reachability-maximizing linear combination of the first and second harmonic $\mathbf{u}_{n=2}$. Baseline kinematics are in red, reachability-maximizing control input ($\mathbf{q}$) in black.

vers, and improvements in visual tracking systems have allowed accurate motion capture within the wingstroke. Dickinson et al. (1993) suggests that small wing kinematic modifications at stroke-reversal can impart sufficient maneuvering loads for insect flight. [96] And Fry et al. (2005) suggest U-shape wing kinematics can benefit dipteran flight maneuvers. High drag on the wings near stroke reversal can generate increased vertical force to assist in keeping the insect aloft. [91] The in-

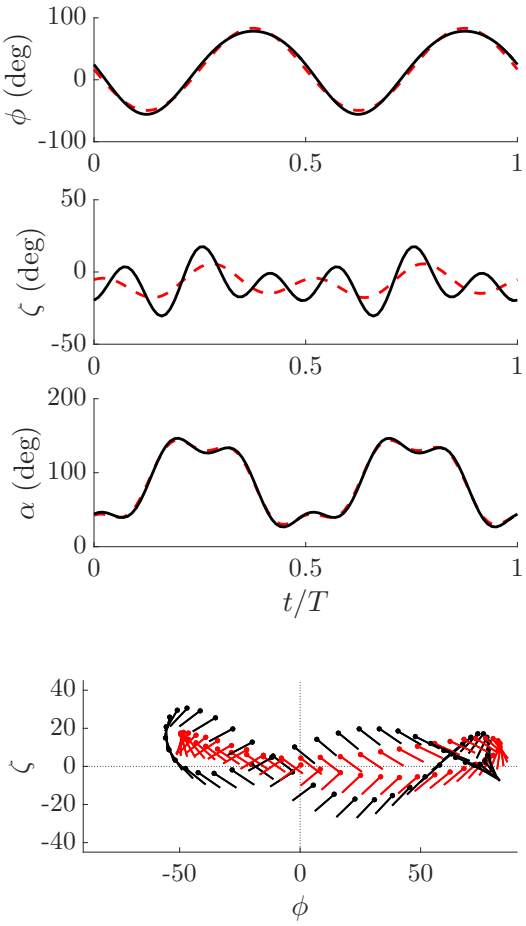


Fig. 5.16: Kinematics resulting from the reachability-maximizing linear combination of the first through third harmonic kinematic control inputs, $\mathbf{u}_{n=3}$. Baseline kinematics are in red, reachability-maximizing control input ($\mathbf{q}$) in black.

creased drag at stroke-reversal due to the U-shape also occurs at the largest moment arm away from the insect's pitching axis; kinematic changes at stroke-reversal would impart more pitching moment.

The analysis presented here supports this. In each of the three sets of general inputs, the elevation angle is the dominant mode for generation of pitching motion, and the largest changes in elevation angle occur during stroke reversals. The U-shape

given by the second Fourier harmonic in Figure 5.15b, in particular, is similar to kinematic inputs seen by Fry et al. (2005). Balint and Dickinson (2001) measured elevation angle modulations for maneuvering blowflies, discovering both the oval shape given by the first Fourier harmonic and the U-shape given by the second harmonic. It is not currently clear why insects would select the first harmonic over the second, if both are possible, when the latter would impart greater agility.

Most previous work, like that above of of Fry et al. and Balin & Dickinson have focused on the study of equilibrium flight kinematics; however, the current work presents options for control by deviation away from this equilibrium. Chen & Sun present the control of *Drosophila* during takeoff. Their conclusion, that a pitching moment is necessary during takeoff for flight stabilization, presents the best available experimental example of wing kinematic control inputs for longitudinal flight. Their measurements of wing kinematics to counter this pitching motion shows direct evidence of large changes to the elevation angle to counter a pitching motion.

The results presented here show little benefit to modulation of wing pitch in imparting dynamical motion; however, several studies have demonstrated the benefit of small pitch changes in generation of maneuvering loads. [54, 75] Motion capture of *Drosophila* by Fontaine et al. (2009) reveal high frequency changes in wing pitch, often at or near stroke reversals. Additionally, Ristroph et al. (2011) demonstrate *Drosophila* generating forward flight motion via a "paddling" motion that is dependent on large changes in pitch. One possibility that wing pitch is not

captured by the reachability-maximizing method is that the changes in pitch are not intended to generate maximum maneuverability; instead they are stabilizing inputs that moderate the insect's flight path. Alternatively, this is due to the quasi-steady aerodynamic modeling, which cannot capture high frequency flow changes around the flapping wing that are more dynamic at stroke-reversals.

Insect wing kinematics are certainly not selected for maneuverability alone. In particular, the methodology discussed here takes no structural requirements into account. The mechanisms in the *Drosophila* wing hinge constrain the wing motion, and are unlikely to allow full range of motion. Muscle and nerve linkages contain couplings that limit available kinematic options. [101, 102] The third Fourier harmonic reaches greater state space than the first or second harmonics (see Figure 5.13), but features kinematic variations not seen in most recordings of insect flight. This suggests that such higher frequency kinematic inputs may not be feasible, possibly due to mechanical constraints.

5.4 Summary

This chapter discussed linear modeling of control inputs for hovering and forward flying *Drosophila*. Four biologically-motivated control inputs were evaluated for effectiveness in driving the model insect dynamics: stroke amplitude, stroke offset, stroke plane tilt, and flapping frequency. A reachability metric was defined to determine the capability of each input in driving the vehicle to the most states. Because the longitudinal dynamics are dominated by pitching-surging motion, the

inputs that drove these motions were most effective. Stroke offset and stroke plane tilt were most effective at driving these modes, and therefore add the most to the vehicle agility. Stroke amplitude and frequency are not as effective at driving the pitching-surging motion, but amplitude especially gives greater control over heave dynamics.

Aerodynamic and inertial power consumption were integrated into the reachability analysis by normalizing control inputs with power consumption. Deviations in stroke offset consume almost no power, and so the offset input becomes more favored than it already was in the reachability metric. This would suggest that barring structural or evolutionary restrictions on the kinematic inputs, the offset would be displayed often by insects in free-flight.

A plethora of possibilities exist for wing kinematic inputs, and intelligently reducing the number would be advantageous to study of insect flight as well as flapping wing vehicle design. A novel technique was described to determine the most effective wing kinematic control input for a given set of reference kinematics. An input-to-output energy maximizing algorithm by Douglas et al. [99] is applied to a Fourier series approximation of individual control inputs, whose effect on the linear dynamics is estimated by the quasi-steady aerodynamic model. The two most effective inputs were given by first harmonic changes to the deviation angle combined with some stroke offset, and second harmonic changes to stroke amplitude combined with offset.

The energy-optimizing control input is shown to contain some stroke-offset

and amplitude changes, but is dominated by changes of the deviation angle away from the equilibrium. Experimental evidence of insect control via deviation angle exists via study of *Drosophila* and others in free flight. Multiple researchers have questioned the purpose of the U-shape or figure-8 shape exhibited by the wingstroke of these insects. Balint & Dickinson (2001) showed that blowflies use an oval-shaped wingstroke and the U-shaped wingstroke at various times, while Fry et al. (2005) discovered U-shape wingstrokes for *Drosophila* . Chen & Sun's (2014) work on *Drosophila* takeoff also demonstrates stark changes to the deviation angle away from the equilibrium to counter pitching motion at the start of flight. These works seem to validate the utility of deviation angle changes to the control of insect flight.

The reachability-maximizing work shown here does not predict wing pitch as a useful control input for longitudinal flapping wing flight. Wing pitch alteration, specifically in the motion of paddling – having higher pitch on one half stroke than the other – has been shown by Fontaine et al. (2009) and Ristroph et al. (2011) to be utilized by *Drosophila* to modulate forward flight speeds. A possible explanation is that the insects are not perturbing the wing pitch with the purpose of maximizing maneuverability, as the reachability-maximizing technique presented here presupposes. Alternatively, it is possible that the quick changes to pitch have an effect on the stability of the LEV or other unsteady features that will not be modeled by the quasi-steady aerodynamics.

In order to select the most effective kinematic input, it is necessary to model a large array of kinematic variables. This is intractable with a Navier-Stokes solver

with today's computational speeds. Validation of the quasi-steady method for aerodynamic load estimation in longitudinal flight is key, as this allows the characterization of a wide variety of kinematic control inputs. Application to lateral-directional kinematic control must wait until a reduced-order aerodynamic method is validated for a full 6DoF model.

Chapter 6: Application to Flapping Wing Micro Air Vehicle

6.1 Motivation

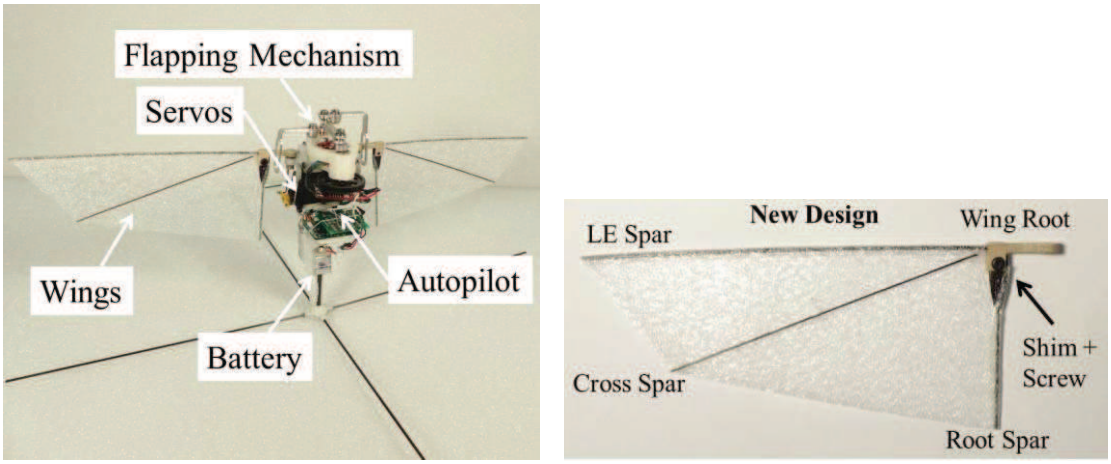
Flapping wing micro air vehicles offer a new platform paradigm for small-scale flight, but size weight and power constraints limit the availability of powerful onboard processors or actuators. Additionally, smaller scale vehicles are subject to the same environmental gusts that larger vehicles encounter. As the vehicle scale decreases, the effect of these disturbances on the vehicle dynamics can be expected to grow. Thus, the flapping wing platform's agility and robustness to disturbance is critical to their design. Understanding the inherent dynamics of flapping wing flight at this scale can assist in the development of new inherently agile and robust flapping wing vehicle designs.

The reduced modeling efforts of previous chapters are not limited in scope to insect flight. In this chapter many of the same modeling techniques that have been previously applied to insects are applied again to a flapping wing micro air vehicle (MAV). The MAV dynamical system is reduced to an LTI model by comparing stroke-averaged aerodynamic loads to perturbations in state and control input. An time-periodic model is developed by And reachability analysis provides a technique

to evaluating the flapping wing kinematic control inputs. The goal is the same: to assess a vehicle's inherent dynamical properties at the MAV-scale and to evaluate the effectiveness of a variety of wing kinematic control inputs on the system.

Modeling at this larger scale does bring new challenges, particularly in estimating the aerodynamic loading. Unlike the linear modeling techniques, the aerodynamic modeling methods are no longer valid. The quasi-steady model, IBINS CFD, and RoboFly aerodynamic methods discussed in Chapter 4 will not properly scale to an MAV-sized flapping wing.

This chapter will read as a return to each previous chapter of the dissertation in miniature, as each aspect of modeling the MAV is taken into account. First is a description of the specific vehicle that will be modeled along with a discussion of the wing kinematics and kinematic inputs on the platform. This is followed by a section on aerodynamic modeling with a CFD solver, OVERTURNS, that is capable of providing estimates of flapping wing loads at these MAV-scales. The LTI longitudinal model is found by using the stroke-averaged loads, and then compared to a time-periodic model that accounts for high-frequency aerodynamic loading. Finally, a selection of wing kinematic control inputs are evaluated using the reachability analysis, and an energy-optimal combination of these inputs is found using the methods of the previous chapter.



(a) *(b)*

Fig. 6.1: The flapping wing MAV platform.

6.2 Flapping Wing Platform

The flapping wing design has been developed by researchers at University of Maryland and University of Texas, Austin. Figure 6.1 shows the design of the robotic flapper and the wing planform. The 62g vehicle has a 12 inch wingspan and aspect ratio of 4.2. It flaps near 22 Hz, making the Reynolds number about 5.2×10^4. The vehicle is similar to a hummingbird in scale. [103]

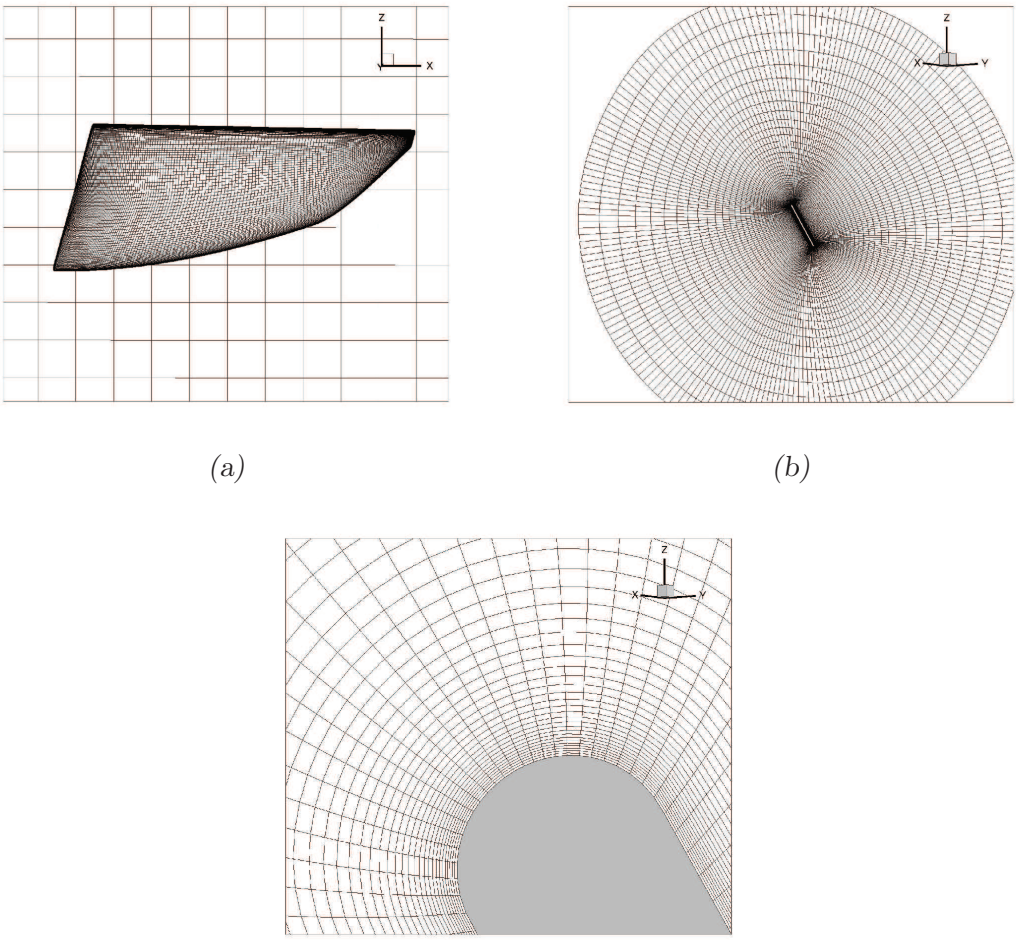
The vehicle uses a novel 5-bar mechanism to amplify the output of a crank-rocker mechanism driven by a brushless motor. Two kinematic inputs are available for vehicle control: amplitude and stroke plane tilt. The vehicle is capable of lifting its weight, and currently is undergoing testing for the onboard controller to extend hover to forward flight.

6.3 OVERTURNS Computational Solver

The OVERTURNS CFD solver was developed in-house at the University of Maryland, and has been used for MAV-scale aerodynamic modeling of multiple platforms, including flapping wing. [104–106] OVERTURNS is a compressible structured overset Reynolds-averaged Navier Stokes (RANS) solver. A MUSCL (Monotonic Upstream-Centered Scheme for Conservation Laws) scheme with Roe flux differencing computes the inviscid terms of the RANS equations, while viscous terms are calculated using a second order central differencing scheme. Low Mach preconditioning is used to improve accuracy and convergence for flows well below the speed of sound. [107, 108] Turbulent flow is handled by the Spalart-Allmaras model. [109]

A single wing was modeled with a plane of symmetry in the xz plane. This reduced computational cost while maintaining the flow conditions for longitudinal flight. A two mesh overset system was designed for this study, consisting of an O-O conformal mesh for a flapping wing and a rectalinear background mesh. Chimera interpolations exchange information between the wing and background meshes, using implicit hole cutting. [104]

The O-O wing mesh was generated with the same morphology as the robotic flapper, with a single wing span of 14 cm, and surface area of 63 cm^2. Figure 6.2 shows the blade mesh used for this study. A background mesh to calculate the aerodynamics in the wake was designed alongside the wing mesh. The mesh design must be focused at the leading edge of the wing, where the leading edge vortex



(a) *(b)*

(c)

Fig. 6.2: The overset mesh system used for this study. (a) The wing mesh surface with the backround mesh behind, (b) a chordwise view of the O-O wing mesh extending from the surface of the wing, and (c) a close-up view of the curvilinear O-O mesh around the leading edge of the wing.

formation takes place.

6.4 Linear Dynamical Modeling

The longitudinal dynamics of the flapping wing MAV are linearized using the small perturbation method outlined in Chapter 4 from the rigid body equations of motion in equation 4.6. The objective is to generate the stability matrix $A(t)$ as in Equation 4.12. OVERTURNS is used to calculate forces and moments on the flapping wing at perturbations in state from the hover reference condition. When modeling a time-invariant system, the stability matrix is constant, and stability derivatives that make up its individual elements are linear regressions of wingstroke-averaged loads. For a time-periodic system the stability matrix is periodic with period T; the stability derivatives are the periodic linear regressions at each moment throughout the wingstroke.

6.4.1 Linear Time Invariant System

The linear model for the hovering flapper is similar in structure to the *Drosophila* in hover, described in Chapter 4, but on slower time scale. Stroke-averaged longitudinal loads are shown in Figure 6.4, and the resulting eigenstructure is given in Figures 6.5 & 6.6. The dynamics are again dominated by a pair of unstable oscillatory modes in the right half plane that couple the fore-aft motion with the pitch rate. This motion is coupled with a fast subsidence mode in the far left half plane that will have little impact on the dynamics. As with the hovering *Drosophila*, heave

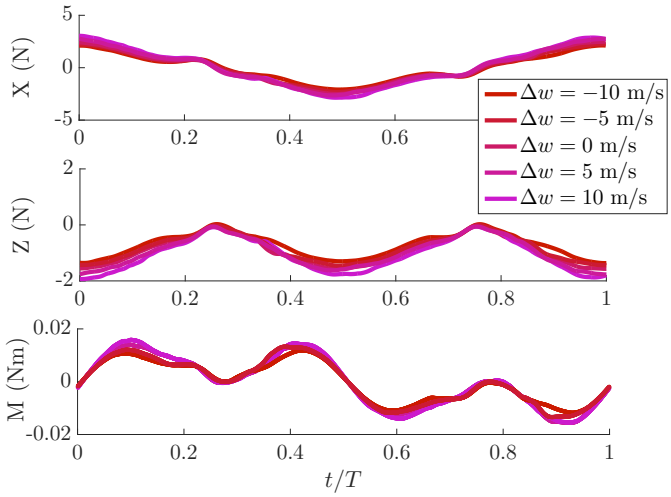


Fig. 6.3: Longitudinal loads on the flapping wing MAV throughout the wingstroke for variation in vertical motion, w, as estimated by OVERTURNS. Stroke reversals occur at $t/T = 0.25$ and $t/T = 0.75$.

dynamics are uncoupled from the pitching-surging motion, and act according to a slow subsidence mode.

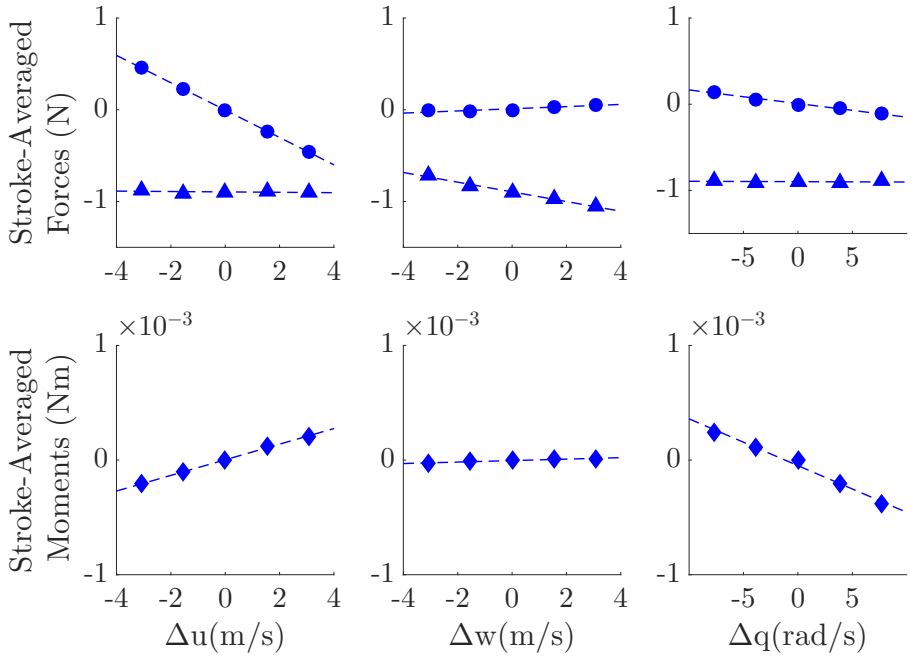


Fig. 6.4: Stroke-averaged longitudinal loads for the flapping wing MAV in perturbations away from the hovering flight condition.

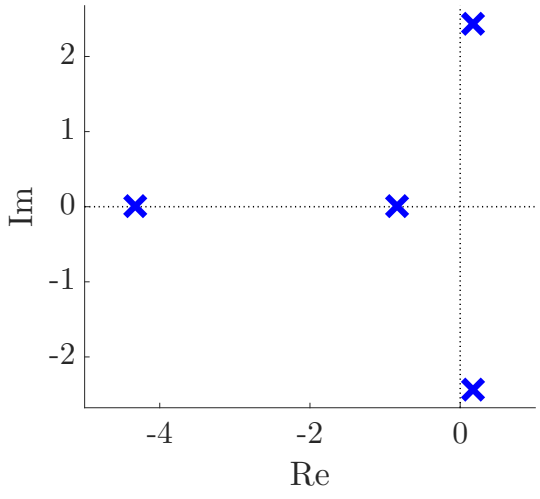


Fig. 6.5: Longitudinal linear modes for the flapping wing MAV.

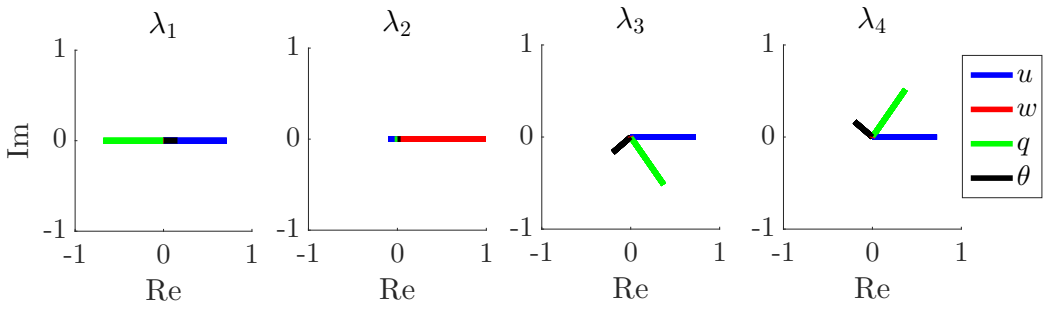


Fig. 6.6: Eigenstructure of the linear modes for the hovering flapping wing MAV. Each eigenvector (scaled to norm 1) is plotted on the Real-Imaginary plane. Note the complete decoupling of the heave motion in the slow subsidence mode λ_2.

6.4.2 Linear Time Periodic System

The two-timing assumption that enables LTI modeling via stroke-averaged loads presumes a forcing frequency much higher than the speed of the vehicle motion. This is not true for the flapping wing MAV that has a flapping frequency of only 22 Hz. The Floquet decomposition described in Chapter 4 gives a test of this assumption to see if the LTI system given in Figures 6.5 & 6.6 are accurately modeling the dynamics. Using the same aerodynamic measurements from OVERTURNS, the linearization of the loads can take place at every instant in time throughout the wingstroke. Figure 6.7 shows the forces throughout the wingstroke, with perturbations in heave velocity.

A comparison of the dynamic responses to a forward velocity for the two models suggest that the two-timing assumption is not valid for the flapping wing MAV. The LTP model displays better resolution of within-wingstroke dynamics, as it did for the *Drosophila* in Figure 4.14; however, in this case, those within-

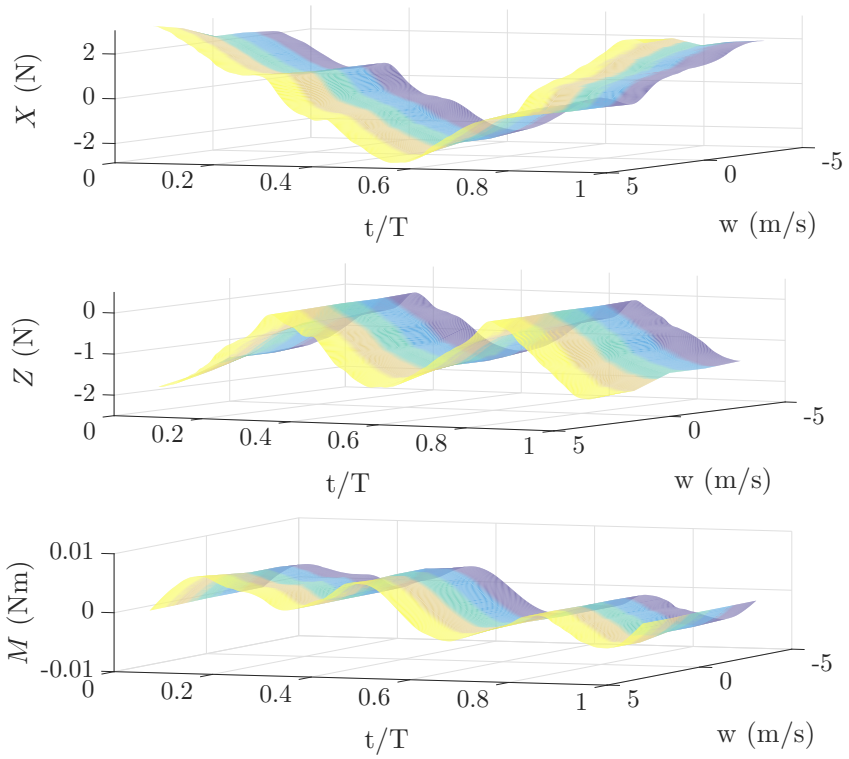


Fig. 6.7: Surface plots of longitudinal forces and moments as functions of both time and perturbation in heave velocity. Each of the five perturbation in Δw are shown in varying color bands.

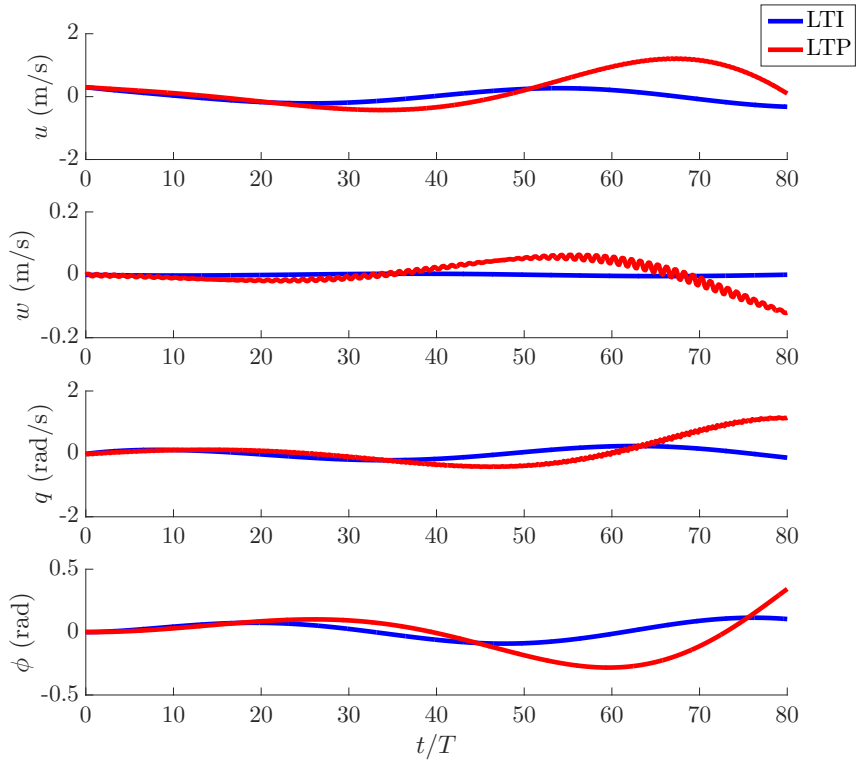


Fig. 6.8: LTI and LTP initial condition responses for the hovering flapper MAV with an initial forward velocity, showing 80 wing strokes (about 3.6 seconds). The LTP model contains more information on scales between wing strokes, evident here in the higher definition of the heave response. Both responses are unstable, but the LTP builds instability more quickly. Also note the decoupling of the heave response is an artifact of the LTI system.

wingstroke loads have a much greater effect on the vehicle dynamics. The LTP system predicts much faster growth of instability, leading to loss of hover within about 80 wingstrokes, or less than 4 seconds of flight time. Initial flight tests with the vehicle show similar results, hovering for about 5 seconds of flight time. [103] Additionally, decoupling of heave motion predicted by the LTI model is not apparent in the LTP version.

This reasserts assumptions of previous researchers that the time-invariance is not likely applicable to mechanical flapping wing systems at the hummingbird scale. Wu & Sun (2012) show that the time periodic solutions for the dronefly (88 mg) are nearly identical to that of the time-invariant model. The larger hawkmoth (1.5 g) showed significant quantitative deviation (although not enough to alter the overall modal structure). [64] The dronefly has a particularly high flapping frequency for its mass, and so the LTI model could be expected to perform well for that system. The hawkmoth is closer to the scale of a hummingbird, and so deviation between the two models is expected. The *Drosophila* discussed in this work is significantly less massive than even the dronefly, but with higher flapping frequency (200 Hz vs 160 Hz for the dronefly).

The need for a time-periodic model for the flapping wing MAV is crucial for controller design. In Section 4.3 a LQR controller designed from the forward flying *Drosophila* LTI model, works well on the LTP model. A similar LQR controller is designed to stabilize the LTI model of the hovering MAV, and is not successful when used on the LTP model. The eigenvalues of the LTI model sug-

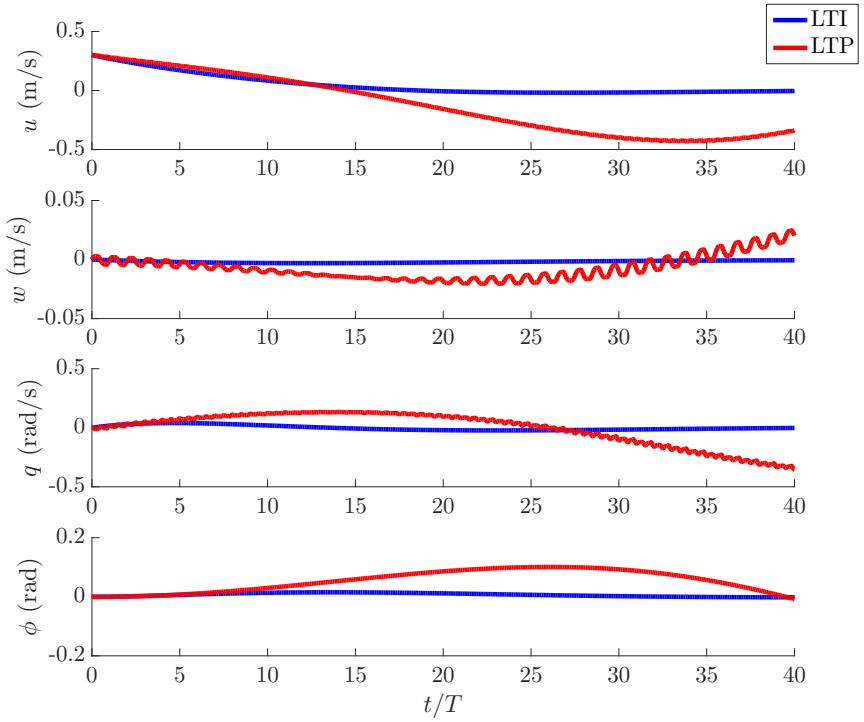


Fig. 6.9: LTI and LTP initial condition responses for closed loop longitudinal dynamics over 40 wingstrokes (about 1.8 seconds). Full state feedback and LQR gains were utilized for closing the loop and stabilizing the system. The LTI characterization fails to accurately predict the instability in the closed loop system.

gest that it will be stabilized by the LQR controller: $\lambda_{\mathrm{CL}} = [-4.2748, -1.6329 + 2.5675j, -1.6329 - 2.5675j, -0.8936]$ However, the maximum eigenvalue of the periodic transition matrix remains unchanged with the addition of the closed loop control: $\max_k(\|\lambda_k(Q)\|) = \max_k(\|\lambda_k(Q_{\mathrm{CL}})\|) = 1.0314$. Figure 6.9 shows the LTI model is successfully controlled, and the disturbance in u is easily sent to zero. The LTP model, with the same LQR gains, fails to stabilize, and begins to oscillate just as in the open loop case.

6.5 Reachability Analysis for Kinematic Control Inputs

The effectiveness of the individual control inputs can be expressed by the reachability gramian, as discussed in Section 5.2. Only two kinematic control inputs for longitudinal flight are currently available on the flapper: amplitude, $\delta_{\phi_{\max}}$; and stroke plane tilt, δ_β. [103] Here, the stroke offset input ($\delta_{\phi_{\mathrm{off}}}$) is evaluated as well, due to its effectiveness for the *Drosophila* models.

Stroke-averaged loads are calculated with perturbation in control input by the OVERTURNS flow solver. According to the linear modeling above, we can assume that the model will be dominated by the pitching-surging motion as with the *Drosophila* Figure 6.11 shows that the direct effect of both the amplitude and offset inputs is relatively uncoupled, with the amplitude driving heave motion, and the offset providing control over the pitching moment, without affecting the vehicle translation. Tilting the stroke plane gives both fore-aft motion and pitching moment simultaneously.

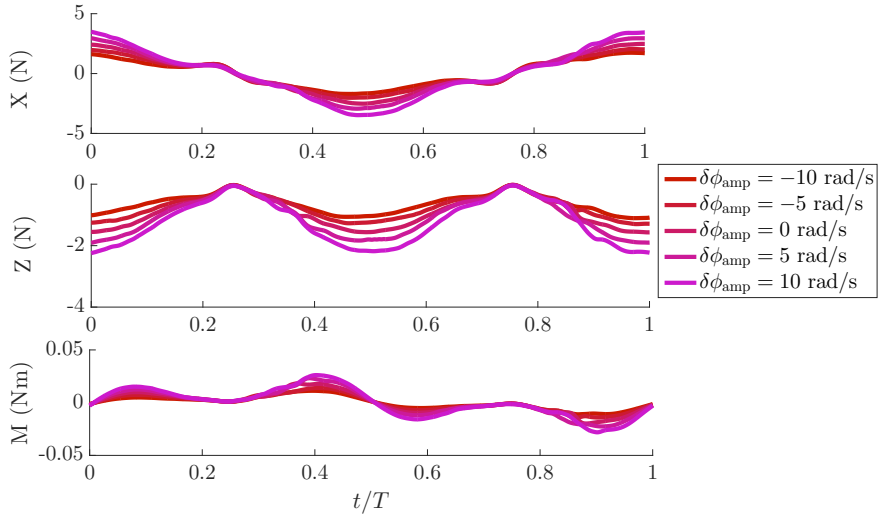


Fig. 6.10: CFD-estimated longitudinal loads on the flapping wing MAV throughout the wingstroke for variation in the amplitude control input, $\delta_{\phi_{\max}}$.

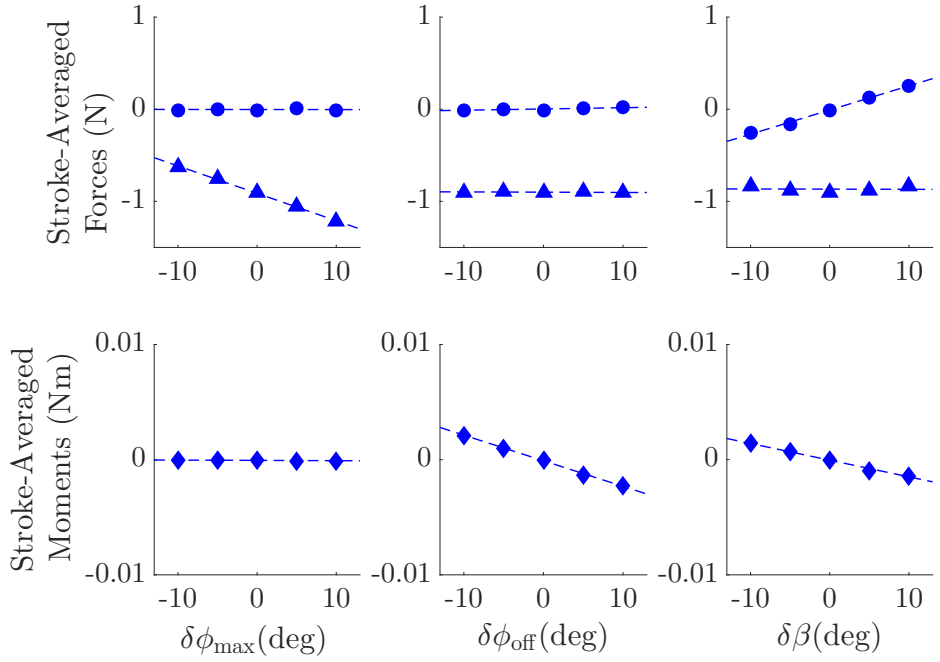


Fig. 6.11: Stroke-averaged longitudinal loads for the flapping wing MAV in control input perturbations away from the hovering flight condition.

	$[\delta\phi_{\max}, \delta\phi_{\text{off}}, \delta\beta]^T$	$\delta\phi_{\max}$	$\delta\phi_{\text{off}}$	$\delta\beta$	$\mathbf{q_1}$	$\mathbf{q_2}$
$\|\Gamma_{\tilde{G}}\|$	9.53	0.30	8.08	5.06	9.53	0.29

Tab. 6.1: Hankel operator norms of the system for a variety of control input options. The offset control input contributes most of the input-output energy for the system, but a linear combination of inputs $\mathbf{q_1}$ can get even closer to the maximal value that is given by a full range of the control inputs.

Because the oscillatory modes drive the linear dynamics of the flapper, the control input that drives this mode most effectively will have the greatest Hankel norm. Figure 6.12 shows that stroke offset control would give the greatest of the three considered here. As with the *Drosophila* model, the amplitude does not contribute much to the unstable oscillatory pitching-surging motion, and so the Hankel norm is much lower than for the other two inputs. Amplitude does, however, directly drive the heave motion, which is evident in the projection of the Hankel norm on the states.

The input reduction technique described in Section 5.3 is applied to the three flapper control inputs. The optimal combination of the control inputs $\mathbf{q_1}$ is given by a offset combined with tilting the stroke plane. Because of the heave decoupling in the LTI model, the heave dynamics are unaffected. The second combination, $\mathbf{q_2}$ contributes much less output energy, but drives the heave dynamics with predominantly amplitude.

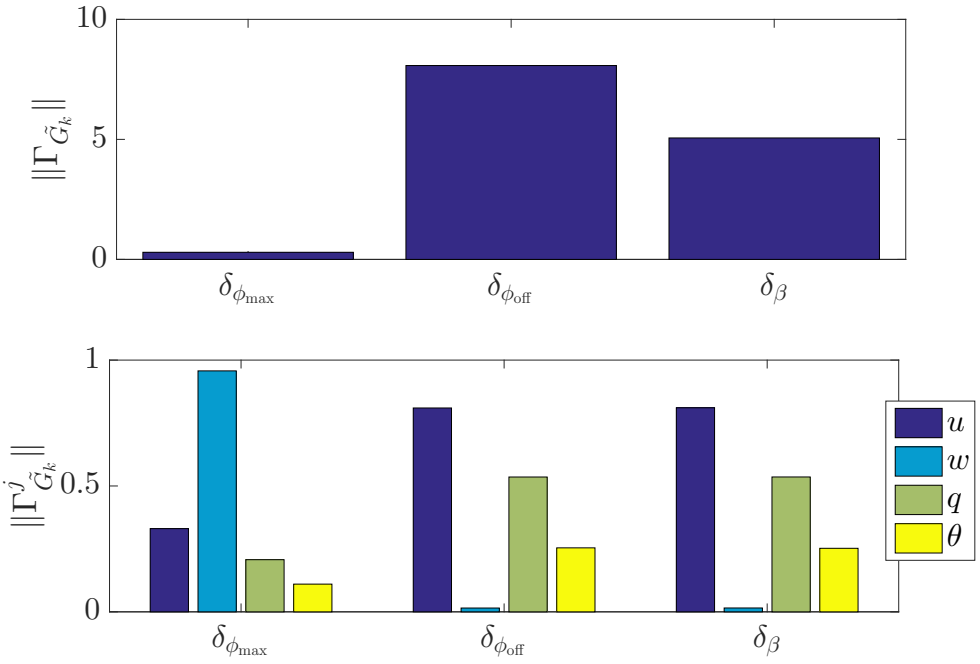


Fig. 6.12: Above, the Hankel norm of system for individual control inputs. Below, the projection of the Hankel norm onto the state-space for each input. Again, the stroke offset, $\delta_{\phi_{\text{off}}}$, contributes the most output energy. Like the forward flying *Drosophila*, the amplitude does not contribute high energy in the system statespace, but does project onto the heave state substantially more than the other control inputs.

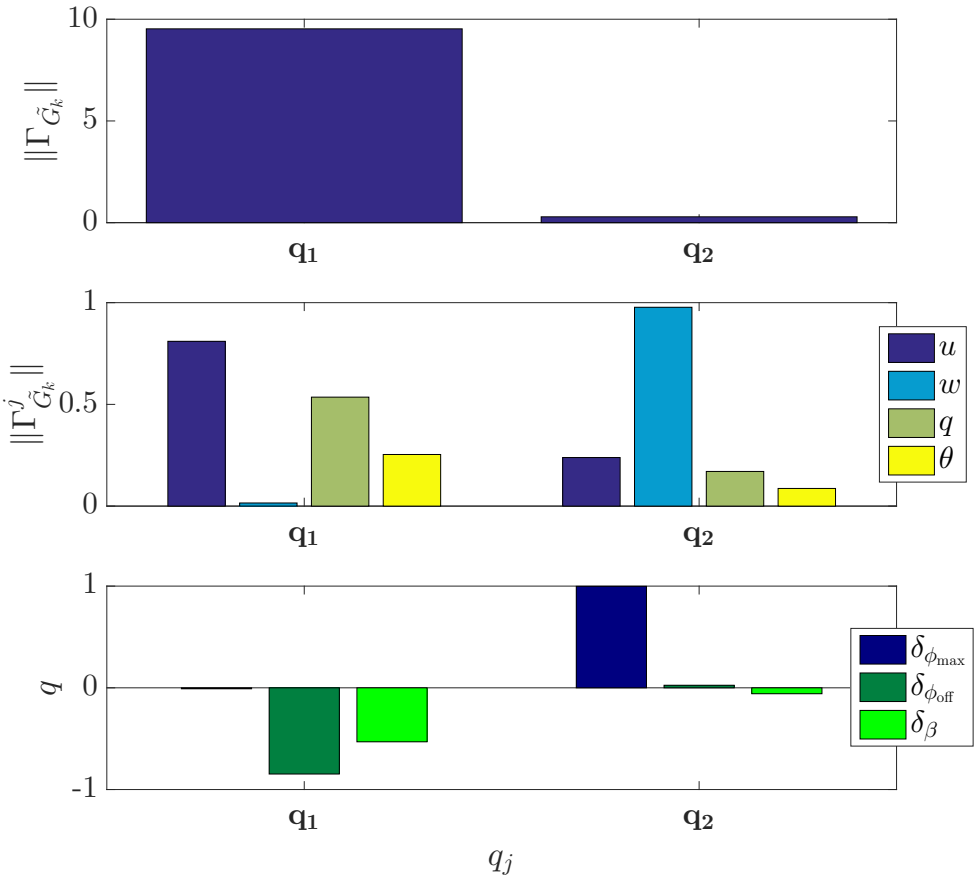


Fig. 6.13: Components of the reducing input vector $\mathbf{q}$ and the resulting Hankel operator norms for the flapper control inputs for a hovering reference condition. On the left are the results for the first, and most optimal, linear combination ($\mathbf{q_1}$); on the right is the second most optimal ($\mathbf{q_2}$).

6.6 Summary

This chapter applied the modeling techniques developed in previous chapters on a hummingbird-sized flapping wing micro air vehicle. Kinematic measurements of flapping wing motion is not currently available, so the similar hovering kinematics to the idealized *Drosophila* hover kinematics were used, with a flat stroke plane and wing pitch approximated by a square wave. The OVERTURNS compressible flow solver calculated aerodynamic loads around a rigid flapping wing. LTI models showed similar dynamical model structure to the *Drosophila* but with slower dynamical speeds of motion. A decoupled heave slow subsidence mode is driven by stroke amplitude. Unstable pitching-surging motion from a pair of unstable oscillatory modes dominates the dynamics and can be driven by either a stroke plane tilt or stroke offset control input.

Reachability analysis suggests that the MAV may benefit from the addition of the stroke offset control input, as it is more effective in driving the pitching-surging motion than the stroke plane tilt. Similar to the *Drosophila* , the MAV control that is most effective of the four studied here is the stroke offest. Even at a different scale, with different wing planform, and a different Navier-Stokes solver, the result was that the stroke-offset control term was most valuable for generating pitch moments, and governing the unstable pitch motion inherent to flapping wing flight. The current platform in development has control solely via amplitude and stroke plane tilt. This work suggests that these control inputs will be able to stabilize

and control the system if capable of performing at the bandwidth required by the instability. However, the platform may be more easily controlled by a stroke-offset control mechanism.

Floquet decomposition for a periodic dynamical model shows that the LTI results may be suspect, however. The flapping frequency is slow enough that the "two-timing" assumption that worked for the *Drosophila* is not applicable to the much larger flapping wing MAV. The time-periodic model displayed instability away from the hover reference condition in about 4 seconds, which is similar to experimental results. A model-based controller developed for the LTI vehicle model with stroke-averaging assumptions failed to stabilize the LTP vehicle model, suggesting that model-based controller design must take the within-wingstroke loading into account.

The result of this work suggests that the time invariance assumption is useful for biological studies of small insects, but not for larger insect or avian flight like that of hawkmoths and hummingbirds, and even less so for engineers designing flapping wing MAVs at larger scales. Standard discussions of helicopter control are typically considered using an average model of flight. [88] This allows the engineer a tractable set of linear equations useful for study of vehicle control. For flapping wing flight, at least at the scale currently of interest to the MAV designer, time-periodicity cannot simply be averaged away and remains yet another difficulty to overcome.

Chapter 7: Conclusions and Future Work

Hover-capable MAVs are ideal for search and rescue missions in buildings too dangerous to enter for emergency responders, or for military reconnaissance in areas suspected to hide dangerous devices or personnel. Their small size leads to an agility unmatched by larger aircraft, but also results in susceptibility to environmental disturbances. Wind gusts that are insignificant on a human scale, such as a strong exhaust from a vent or a gust through a window, could be disastrous on the scale of the MAV. As hover-capable flapping wing vehicles are becoming available due to the same technologies, they offer unique challenges in control design – unlike many other MAV designs there is neither swashplate or tail rotor to provide control over the vehicle motion. Moreover, although there are examples of impressive agility and robustness to disturbance in the biological world, it is not yet clear how the MAV equivalent will compare to similarly sized rotorcraft. Flapping wings hold potential in terms of energy storage, maneuverability, and response to wind gusts, but they also offer a unique challenge in both design, construction, and control.

Sensing and control design for flapping wing systems begins with an understanding of the dynamics of the platform. A model for the flight dynamics of a system can describe the speed and direction of motion incurred by control inputs

and environmental disturbances. Understanding the natural motion of a flight vehicle is vital for vehicle design, sensor selection, and implementation of vehicle control. For the flapping wing vehicle, the complexity of the aerodynamic flows, time periodic dynamics, and the variety of control inputs requires a reduced-order model for the flight behavior.

7.1 Conclusions

This dissertation has presented reduced order models for both the insect system (*Drosophila*), and a larger hummingbird-scale flapping wing MAV. These models are relevant to better understanding sensing and control of both biological and mechanical systems. The following are specific conclusions from this work:

7.1.1 Verification of a reduced-order aerodynamic method for dynamical modeling at insect scale

The first goal of this dissertation is a verification of an experimentally-derived quasi-steady aerodynamic method for estimating flight dynamics. This was accomplished by identifying a model of the dynamics for *Drosophila* in both hovering and forward flight using the quasi-steady aerodynamic model, the IBINS computational solver, and the Robofly apparatus for verification. A linear time invariant (LTI) model was given for hovering and forward flight *Drosophila* based on insect motion captured in free-flight. The longitudinal LTI model structure was similar for all three

aerodynamic estimation methods: quasi-steady, computational, and experimental. Each of the models generated in this work agreed with previous research that the longitudinal motion is dominated by unstable oscillatory motion in pitch and fore-aft motion that is largely decoupled from heave motion. Moreover, the quasi-steady aerodynamic model was no further from the more rigorous computationally-derived model than it was from the experimental verification given via Robofly.

A reduced-order aerodynamic model that can correctly predict every aspect of flapping wing flight for any specified set of wing kinematics is almost certainly impossible. However, the question remains whether such an aerodynamic model can be good enough to estimate the dynamics, regardless of some inaccuracies in the within-wingstroke estimate. If so, the sensing and control design of flapping wing vehicles can be informed by an estimate of the dynamical behavior of the flapping system. Vehicle designers can arrange sensors to observe a particularly sensitive dynamical motion, and selected sensor bandwidth to match expected speed of vehicle motion. They can select actuators that counter specific instabilities, again with knowledge of the necessary direction and speed of motion. Without a simpler aerodynamic model, the estimate of the dynamics is unlikely except for the best funded and longest term projects.

(i) **Kinematics** Extraction of *Drosophila* forward flight wing kinematics from a high speed flight capture setup. In addition to a set of idealized hover kinematics, two sets of forward flight kinematics were identified: a slow forward flight at 7.07 cm/s, and a fast forward flight at 32 cm/s.

(ii) **CFD verification** Verification of an immersed boundary incompressible flow solver against experimental data for *Drosophila*-scale insect flight. The IBINS code agreed with experimental RoboFly setup, and showed differences in lift throughout the wingstroke of less than 3%.

(iii) **Longitudinal flight modeling** A verification of previous flapping wing longitudinal dynamical modeling that is dominated by an unstable pitching-surging motion, relatively uncoupled from stable heave motion. Similarity between the different aerodynamic methods suggests that while the quasi-steady aerodynamic estimate does not give the most accurate aerodynamic loading within a wingstroke, the resulting dynamical motion remains consistent. In fact, the time to double of the quasi-steady method is between the CFD and experimental estimates for both the slow and fast forward flight cases. The quasi-steady estimate gives a doubling time of 53.6 ms for the slow forward flight, while CFD gives 43.1 ms, and Robofly 50.3 ms. In fast forward flight, the times to double are 100.7 ms, 105.8 ms, and 79.1 ms respectively. The heave-dominated subsidence modes are even closer in agreement. This suggests that the experimentally-derived reduced-order aerodynamic model would be useful to a flapping wing vehicle designer at this scale, or to a interested biologist studying wing kinematics for such an insect. This suggests no complicated aerodynamic phenomena resulting from longitudinal motion that substantially changes the flapping wing vehicle dynamics.

(iv) **Lateral-Directional flight modeling** Indication that the experimentally-derived quasi-steady aerodynamic estimate is inappropriate for modeling lateral-directional dynamics of *Drosophila*-scale insect flight. Here, the quasi-steady and computational models disagreed substantially (the Robofly apparatus did not have the range of motion to provide the lateral-directional model). Both models show a system dominated by yaw motion in each of the four modes; the similarities end here, however. The quasi-steady model provides a pair of stable oscillatory modes with rolling-yawing motion, and two yaw subsidence modes. The computational model is unstable with a yaw-dominated mode in the right half-plane. A roll-yaw oscillatory motion similar to that found by the quasi-steady method appears far more stable. This may suggest that the quasi-steady model shown here, which does not accurately model changes in spanwise flow due to lateral-directional state perturbations, should not be utilized in such dynamical modeling. Alternatively, the inconsistency could result from numerical issues, and the linearization is not appropriate.

7.1.2 Time-invariance assumptions

The second goal of this work is an investigation of the importance of time periodicity in flapping wing flight. The dynamics of a flapping wing system are inherently periodic; however, a linear time invariant (LTI) model of the system is often preferable for its simplicity in control scheme implementation. For vehicles with much slower dynamics than the unsteady forcing, a time-scale separation via

stroke-averaging yields an LTI system model. This assumption was tested in this work for two model systems: the *Drosophila*-scale model, and a hummingbird-scale flapping wing MAV in development.

(i) ***Drosophila*-scale time invariance** The concept of separating time scales was tested on the *Drosophila* model by comparing the time-invariant model with a time-periodic model. This resulted in confirmation that the time-invariant assumption is appropriate for *Drosophila*-scale modeling. By considering within-wingstroke aerodynamic loading, the LTP model shows better resolution in between wingstrokes, but gives comparable results in simulation to the LTI model. A feedback control strategy based on the LTI model is shown to work well with the more accurate LTP model.

(ii) **Hummingbird-scale MAV longitudinal model** A longitudinal model was identified using the OVERTURNS computational solver for a hummingbird-sized flapping wing MAV. Linear modeling techniques applied to a hummingbird-scale flapping wing MAV suggest similar modal structure to the *Drosophila*, but at slower dynamical speeds – loss of hover occurs after 4 seconds. This is similar to initial testing that shows loss of hover after about 5 seconds.

(iii) **Hummingbird-scale MAV time invariance** An assumption of time-invariance is shown to be ineffective in accurately modeling dynamics of a hummingbird-scale flapping wing MAV due to within-wingstroke aerodynamic loading. For this larger scale vehicle, with slower wing beat frequency, the periodic model

does not follow with the time-invariant, and it is evident that within-wingstroke forcing is important to the overall vehicle dynamics. The LTI model showed a heave mode decoupled from the unstable pitch-surge motion, but the actual time-periodic longitudinal system is completely coupled. A closed loop controller designed using the LTI model was unable to stabilize the LTP system, indicating that the LTI system would not be useful for control modeling. A designer of the control for such a vehicle should be aware of the coupling between all longitudinal motions and the LTI system would be misleading.

7.1.3 Control input selection for flapping wing flight

The third objective of this work is a methodology to select control inputs for flapping wing flight from a general set. A wide variety of available wing kinematic options for flight control, and the appropriate selection of appropriate control for feedback is not obvious. Previous researchers that have estimated the effects of control inputs on the vehicle dynamics have had to select kinematic perturbations to the baseline based on intuition or imitation of insect flight. However multiple studies suggest that insects utilize a wide range of kinematic inputs to control flight, including amplitude, frequency, wing pitch, and deviation from the stroke plane. It is not apparent whether insects and birds select wing kinematic inputs to maximize control authority or minimize power consumed, nor is it clear what limitations exist in terms of mechanical or structural stress in the wing hinge or wing itself. In is work a reachability metric is utilized for evaluation of specific control inputs to flight

dynamic models.

(i) **Reachability metric** To verify the effects of this maximization, reachability is maximized using a linear combination of a set of four biologically-motivated wing kinematic inputs. Because the longitudinal dynamics are dominated by pitching-surging motion, the inputs that drove these motions are most effective. The pitch-offset term was the most effective of the four in inciting pitching motion (the fore-aft change in center of pressure generates a large pitching moment). These results suggest that stroke offset is among the most power-effective control for both the *Drosophila* and MAV models. Evaluation of four biologically-motivated wing kinematic inputs using power-normalized reachability analysis suggests that stroke offset is also the most power-effective control of those four.

(ii) **Reachability-maximizing control input selection** An extension of reachability analysis is presented that provides the most energy-optimal control inputs from a general set. The reachability of the platform can be maximized by a linear combination of an array of control inputs; this maximizes the agility of the linear model.

(iii) ***Drosophila* control input selection** A general set of kinematic control inputs were defined using Fourier harmonics and their effect on reaching longitudinal states was identified using quasi-steady aerodynamic calculations. Both the first and second order kinematic inputs activate the pitch-surge mode of

the vehicle dynamics. Indeed, activation of this mode is what makes these inputs more energy-optimizing. The most energy-effective linear combination of biologically-motivated control inputs for *Drosophila* in forward flight are given. Identification of a wide array of control inputs is possible due to the ability of the quasi-steady method to model *Drosophila* in longitudinal flight. The energy-optimizing control input is shown to contain some stroke-offset and amplitude changes, but is dominated by changes of the deviation angle away from the equilibrium.

(iv) **Hummingbird-scale MAV control input selection** Stroke offset is most effective input (of the four inputs studied) at driving the hummingbird-scale MAV according to reachability metrics. The current platform in development has control solely via amplitude and stroke plane tilt. This work suggests that these control inputs will be able to stabilize and control the system if capable of performing at the bandwidth required by the instability. However, the platform may be more easily controlled by a stroke-offset control mechanism.

7.2 Future Work

This dissertation leads to several possibilities for continuation in studying reduced order flapping wing models. First, and most obviously, the contributions are mostly aligned along the longitudinal dynamics. Because small changes in the results lead to such large dynamic changes, this suggests that the LTI model may not be appropriate to model the dynamics. However, the lateral directional dynamics were

difficult to verify due to experimental limitations on RoboFly. With additional degrees of freedom to that apparatus (or another similar setup), the lateral-directional motion can be better characterized.

Another assumption made throughout this work is that the wings remain rigid throughout the wingstroke. While the rigid assumption was required to make the computations and experiments tractable, flexibility of the wings is noted and likely important to the aerodynamic forcing, especially as the scale increases and the inertia of the wing grows. Previous work has shown that hoverflies exhibit significant wing twist variation throughout the stroke, ostensibly with the goal of decreasing drag in forward flight. [110] At larger scales, such as for the hummingbird MAV, we can expect these effects to increase in effect. One method would be to couple the wing's structural dynamics with the CFD, but this is quite computationally expensive when multiple CFD-CSD runs are needed for each stability or control derivative. This has been done previously using OVERTURNS for the avian scale. [106] Another possibility is prescribing known kinematics on a wing mesh from known kinematics measured from a insect, bird, or MAV in flight. This eliminates some of the computational cost, but requires accurate a priori kinematic extraction.

The dynamics of a hummingbird-scale flapping wing MAV were found using a time-periodic model forced from CFD calculations. Experimental verification would be useful to show that the dynamics are accurately modeled. Flexing of the flapping wing during flight is documented by the designers of the MAV and will undeniably have an effect on the aerodynamic forcing and therefore the vehicle dynamics. [103]

Augmentation of the OVERTURNS flow solver to address wing flexibility is ongoing, and will account for these issues.

Additionally, no applicable quasi-steady routine is available for comparison at the flapping wing MAV scale. A quasi-steady aerodynamic model would be useful for quickly testing alternative kinematics and for suggesting optimal control inputs. However, the effect of within-wingstroke forcing on the overall dynamics may indicate that such a quasi-steady model will not be effective without capturing all the aerodynamic loading during stroke reversals and wake capture. Moreover the unsteady effects at these Reynolds numbers tend to become more difficult to predict, particularly because the LEV is not as stable at smaller scales and tends to burst or detach during the stroke. [111]

The energy-optimizing control input routine would benefit from experimental validation. The algorithm suggests some non-intuitive and quite interesting possibilities as the most effective. Although many of the previous kinematic modeling efforts have focused on the kinematics required for maximum or most efficient lift, some have noted that a change in elevation angle out of the stroke plane could be quite beneficial for control purposes. [75] If the dynamical model is valid, there is no reason to immediately discount the suggested kinematic inputs, but an example of an insect in flight or validation via experiment would lend more credence to the methodology. Additionally, in an actual flight control design, it is necessary to have inputs that activate multiple state-directions, thereby decoupling the motion in the states, so the pilot has control in more than one direction. It would be advanta-

geous to mold the energy-optimizing technique described in this chapter to prefer user-defined directions in state, giving the designer more ability to set the resulting state directions given by the energy-optimal control.

The energy-optimizing kinematic inputs are currently based on an infinite-time horizon state reachability. Due to the time horizon, unstable and undamped linear modes will always dominate the optimal inputs. This may not always be in the vehicle design's best interest, as it is often more important to know what states you can reach in a limited time. An augmentation of the technique to limit the time-horizon could lead to an interesting and perhaps more useful set of inputs. Additionally, an extension to a time-periodic formulation could allow development of high frequency kinematic inputs within a single wingstroke period.

APPENDIX

Appendix A: Compilation of Stability and Control Derivatives

A.1 *Drosophila*

		Quasi-Steady			CFD			RoboFly		
		u	w	q	u	w	q	u	w	q
Hover	$X_{[.]}$	-5.5	-0.10	0.0	-2.7	-0.20	-0.1	–	–	–
	$Z_{[.]}$	0.0	-3.9	0.0	-0.1	-2.9	0.0	–	–	–
	$M_{[.]}$	1930	1720	-7.2	2940	1335	-8.7	–	–	–
FF1	$X_{[.]}$	-3.9	0.5	0.0	-4.4	1.5	0	-11.5	-1.6	0
	$Z_{[.]}$	0.1	-6.6	0.10	-1.1	-7.6	0.1	10.0	-11.5	0.1
	$M_{[.]}$	4103	-174	-8.6	4667	1758	-3.2	7593	944	-13.3
FF2	$X_{[.]}$	-2.8	-0.29	0.001	-4.83	1.48	-0.034	-3.69	-1.63	0.003
	$Z_{[.]}$	-0.70	-3.6	0.330	-2.18	-3.95	0.323	-1.37	-4.97	0.332
	$M_{[.]}$	1893	-2096	-3.92	1897	-387	-11.5	1873	-317	0-8.45

Tab. A.1: Longitudinal stability derivatives for the *Drosophila* in the three flight conditions studied in this work: hover, slow forward flight (FF1), and fast forward flight (FF2). The estimates based on each of the three aerodynamic methods are given here. Robofly results were not available for the hover condition. See discussion of these results in Chapter 4.

		Quasi-Steady			CFD		
		v	p	r	v	p	r
FF2	$Y_{[\cdot]}$	-1.90	0	0	-3.4	0	-0.3
	$L_{[\cdot]}$	-1640	-23	9.9	1122	13.6	-23.6
	$N_{[\cdot]}$	31860	30	-224	24480	-37	-177

Tab. A.2: Lateral-Directional stability derivatives in the fast forward flight condition (FF2). The estimates based on the quasi-steady aerodynamic method and IBINS CFD solver are given here. Robofly results were not available for lateral-directional perturbations. See discussion of these results in Chapter 4.

		Quasi-Steady				CFD			
		$\delta_{\phi_{\max}}$	$\delta_{\phi_{\text{off}}}$	δ_β	δ_f	$\delta_{\phi_{\max}}$	$\delta_{\phi_{\text{off}}}$	δ_β	δ_f
FF1	$X_{[\cdot]}$	0.018	0.011	-0.214	-0.063	–	–	–	–
	$Z_{[\cdot]}$	-0.351	0.0	-0.027	-0.151	–	–	–	–
	$M_{[\cdot]}$	15.6	-596.1	153.6	33.0	–	–	–	–
FF2	$X_{[\cdot]}$	-0.026	0.017	-0.093	-0.005	-0.031	0.009	-0.028	-0.015
	$Z_{[\cdot]}$	-0.191	0.0	0.003	-0.030	-0.132	-0.016	0.007	-0.0377
	$M_{[\cdot]}$	-204.7	-217.5	32.3	-26.2	-59.4	-179.6	38.04	-18.5

Tab. A.3: Longitudinal control derivatives in the two flight conditions considered in this work: slow forward flight (FF1), and fast forward flight (FF2). The estimates based on the quasi-steady aerodynamic method and IBINS CFD solver are given here (CFD results are not available for control perturbations in FF1). See discussion of these results in Chapter 5.

A.2 Flapping Wing MAV

		CFD		
		u	w	q
Hover	$X_{[\cdot]}$	-2.4047	0.1903	-0.2553
	$Z_{[\cdot]}$	-0.0339	-0.8517	-0.0071
	$M_{[\cdot]}$	2.6200	0.2472	-1.5701

Tab. A.4: Longitudinal stability derivatives for the flapping wing MAV in hover. See discussion of these results in Chapter 6.

		CFD		
		$\delta_{\phi_{\max}}$	$\delta_{\phi_{\text{off}}}$	δ_{β}
Hover	$X_{[\cdot]}$	-0.0011	0.0221	0.4231
	$Z_{[\cdot]}$	-0.4801	-0.0048	-0.0029
	$M_{[\cdot]}$	-0.0958	-8.5505	-5.5670

Tab. A.5: Longitudinal control derivatives for the flapping wing MAV in hover. See discussion of these results in Chapter 6.

Appendix B: Compilation of Linear Dynamical Systems

		Quasi-Steady			CFD			RoboFly		
		λ_1	λ_2	λ_3	λ_1	λ_2	λ_3	λ_1	λ_2	λ_3
Hover	λ	$9.1796 \pm 22.9250i$	-3.9000	-31.0591	$9.8087 \pm 28.8250i$	-2.8546	-31.0629	–	–	–
	u	$0.0085 \pm 0.0119i$	-0.6162	0.0123	$0.0063 \pm 0.0098i$	-0.4121	0.0076	–	–	–
	w	0.0000	0.6917	0.0000	0.0	0.9078	0.0000	–	–	–
	q	0.9991	-0.3648	-0.9994	0.9994	0.0736	-0.9995	–	–	–
	θ	$0.0150 \mp 0.0376i$	0.0935	0.0322	$0.0106 \mp 0.0311i$	-0.0258	0.0322	–	–	–
FF1	λ	$12.9358 \pm 29.5812i$	-6.6375	-38.3341	$16.0955 \pm 29.5674i$	-7.2183	-40.1727	$13.7717 \pm 35.8609i$	-12.5201	-51.3233
	u	$-0.0053 \mp 0.0071i$	-0.0388	0.0074	$0.0036 \pm 0.0071i$	0.3369	0.0067	$0.0032 \pm 0.0049i$	0.0510	-0.0048
	w	$-0.0016 \pm 0.0024i$	-0.9208	0.0031	$0.0014 \mp 0.0021i$	-0.8950	0.0033	$0.0027 \mp 0.0018i$	-0.4113	-0.0013
	q	-0.9995	0.3837	-0.9996	0.9995	0.2896	-0.9997	0.9996	-0.9072	0.9998
	θ	$-0.0124 \pm 0.0284i$	-0.0578	0.0261	$0.0142 \mp 0.0261i$	-0.0401	0.0249	$0.0093 \mp 0.0243i$	0.0725	-0.0195
FF2	λ	$6.4625 \pm 29.9637i$	-4.6400	-18.5995	$6.5488 \pm 23.9468i$	-4.6136	-28.7748	$8.7612 \pm 23.9157i$	-4.9637	-29.6658
	u	$0.0090 \pm 0.0050i$	-0.6460	-0.0338	$0.0103 \pm 0.0104i$	-0.1626	0.0120	$0.0101 \pm 0.0110i$	-0.1365	0.0137
	w	$0.0032 \mp 0.0098i$	-0.5832	-0.0235	$0.0038 \mp 0.0109i$	-0.8071	0.0140	$0.0053 \mp 0.0103i$	-0.8004	0.0142
	q	0.9994	0.4815	0.9977	0.9990	0.5547	-0.9992	0.9991	-0.5723	-0.9992
	θ	$0.0069 \mp 0.0319i$	-0.1038	-0.0536	$0.0106 \mp 0.0388i$	-0.1202	0.0347	$0.0135 \mp 0.0368i$	0.1153	0.0337

Tab. B.1: Longitudinal modes for the *Drosophila* in the three flight conditions studied in this work: hover, slow forward flight (FF1), and fast forward flight (FF2). Robofly results were not available for the hover condition. See discussion of these results in Chapter 4.

		Quasi-Steady			CFD		
		λ_1	λ_2	λ_3	λ_1	λ_2	λ_3
	λ	$-10.6 \pm 4.94i$	-54.1	-190.6	13.3	-51.25	-83.2 ± 26.5
FF2	v	-0.0077	-0.0062	-0.002	-0.0074	-0.0035	0.0036
	p	$-0.272 \pm 0.0772i$	-0.0447	0.045	0.53	-0.55	-0.23 ∓ 0.12
	ϕ	$-0.0239 \pm 0.004i$	0.0	0.0	0.04	-0.107	0.002 ∓ 0.021
	r	-0.959	-0.999	-0.999	0.844	-0.835	0.966

Tab. B.2: Lateral-directional modes for the *Drosophila* in the fast forward flight condition (FF2). Robofly results are not available for lateral-directional perturbations. See discussion of these results in Chapter 4.

		CFD		
		$\lambda_1 = 0.1719 \pm 2.4332i$	$\lambda_2 = -0.8480$	$\lambda_3 = -4.3223$
Hover	u	0.7264	-0.1022	0.7150
	w	$-0.0027 \pm 0.0101i$	0.9936	0.0056
	q	$0.3708 \mp 0.5165i$	-0.0308	-0.6811
	θ	$-0.2005 \mp 0.1665i$	0.0363	0.1576

Tab. B.3: Longitudinal modes of the flapping wing MAV in hover. See discussion of these results in Chapter 6.

Appendix C: Flapping wing aerodynamic loads

C.1 *Drosophila*

C.1.1 Stability Derivatives

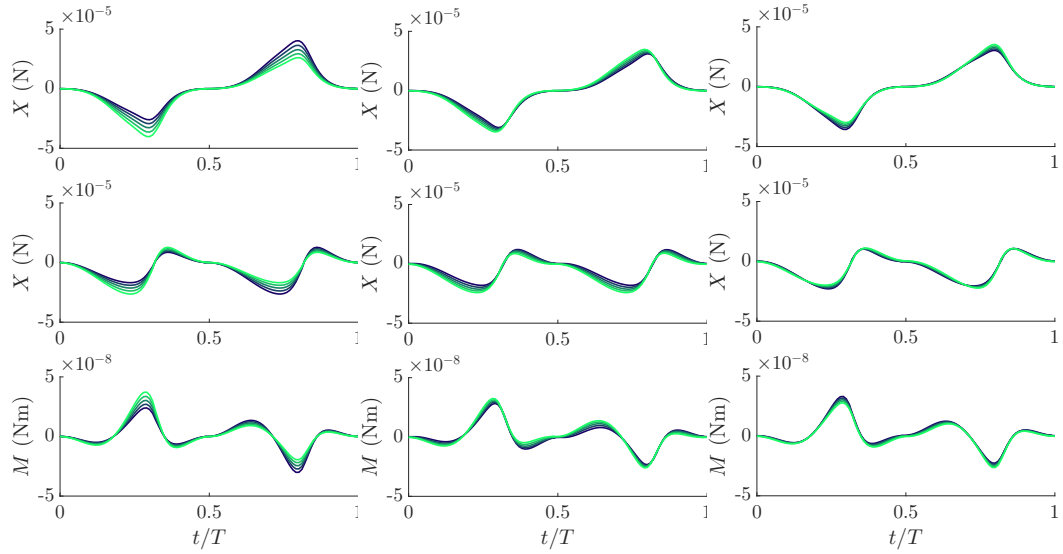


Fig. C.1: Longitudinal loads calculated by the quasi-steady method over a single wingstroke for the *Drosophila* in hover. Left three plots show loads for varying Δu, center 3 show loads for varying Δw, right 3 show loads for varying Δq.

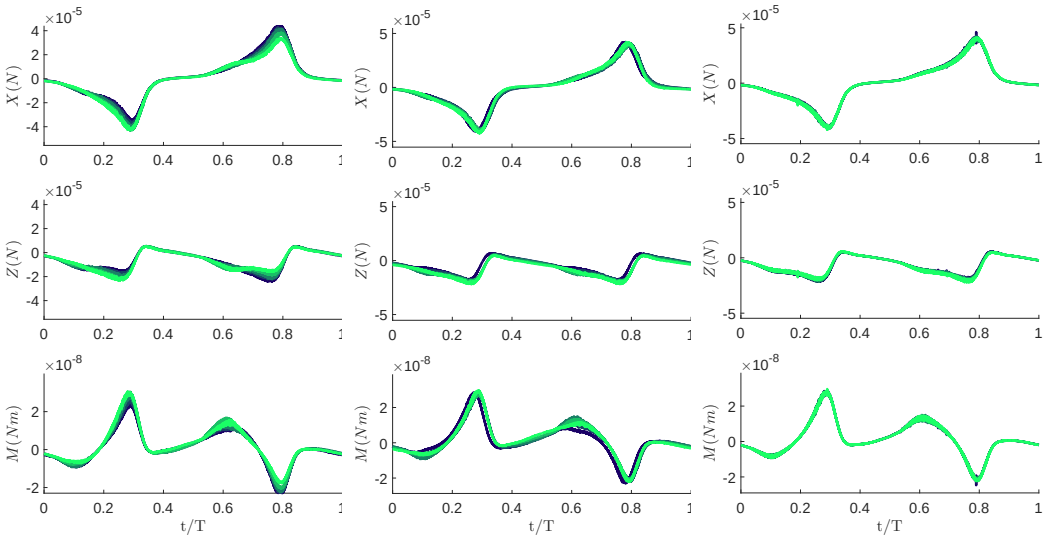


Fig. C.2: Longitudinal loads calculated by IBINS CFD over a single wingstroke for the *Drosophila* in hover. Left three plots show loads for varying Δu, center 3 show loads for varying Δw, right 3 show loads for varying Δq.

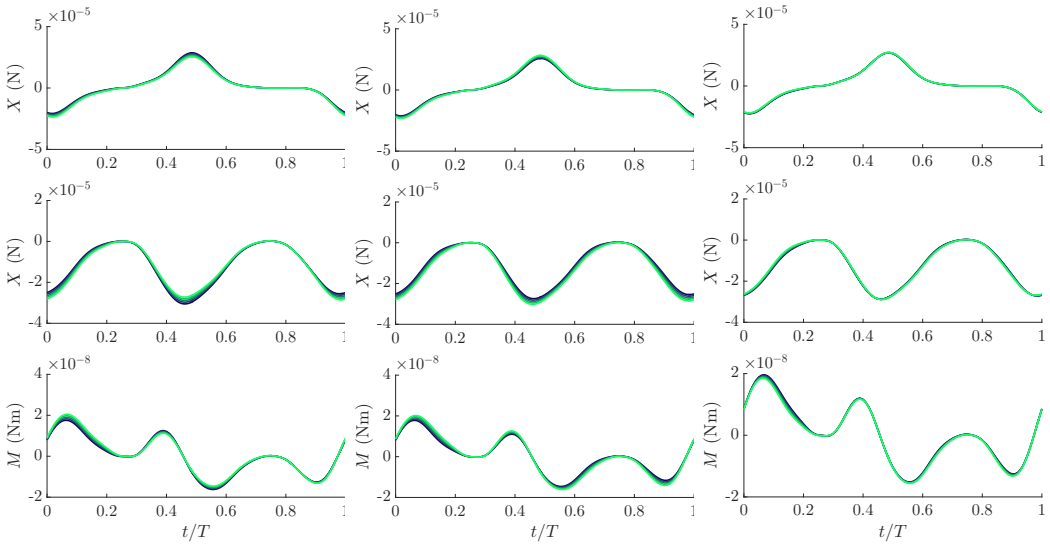


Fig. C.3: Longitudinal loads calculated by quasi-steady method over a single wingstroke for the *Drosophila* in slow forward flight. Left three plots show loads for varying Δu, center 3 show loads for varying Δw, right 3 show loads for varying Δq.

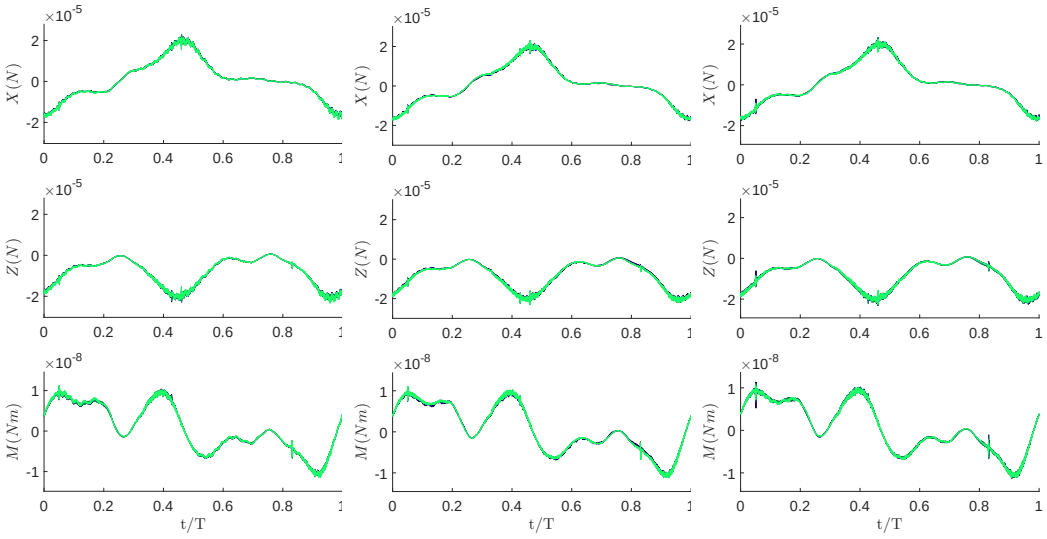


Fig. C.4: Longitudinal loads calculated by IBINS CFD over a single wingstroke for the *Drosophila* in slow forward flight. Left three plots show loads for varying Δu, center 3 show loads for varying Δw, right 3 show loads for varying Δq.

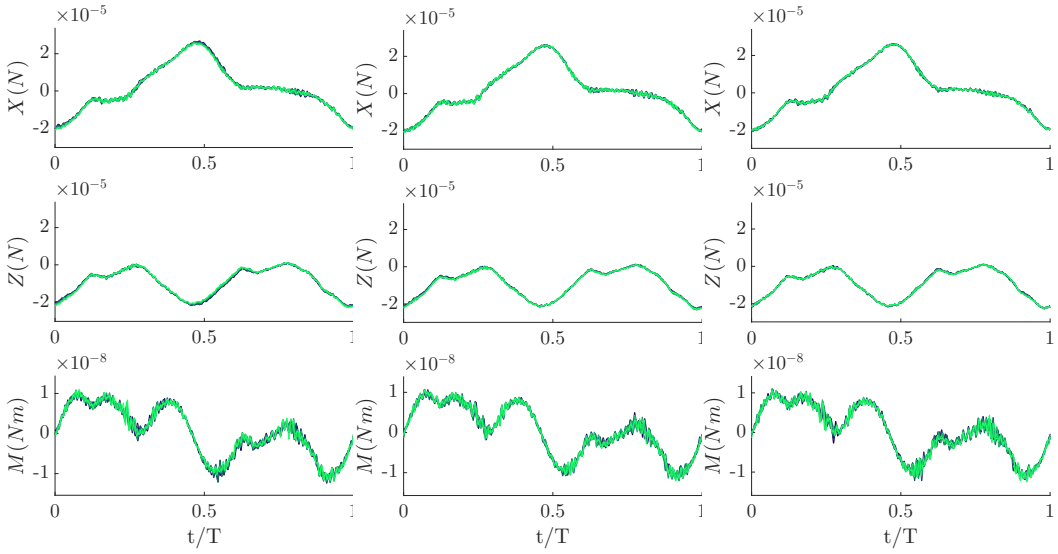


Fig. C.5: Longitudinal loads measured using Robofly over a single wingstroke for the *Drosophila* in slow forward flight. Left three plots show loads for varying Δu, center 3 show loads for varying Δw, right 3 show loads for varying Δq.

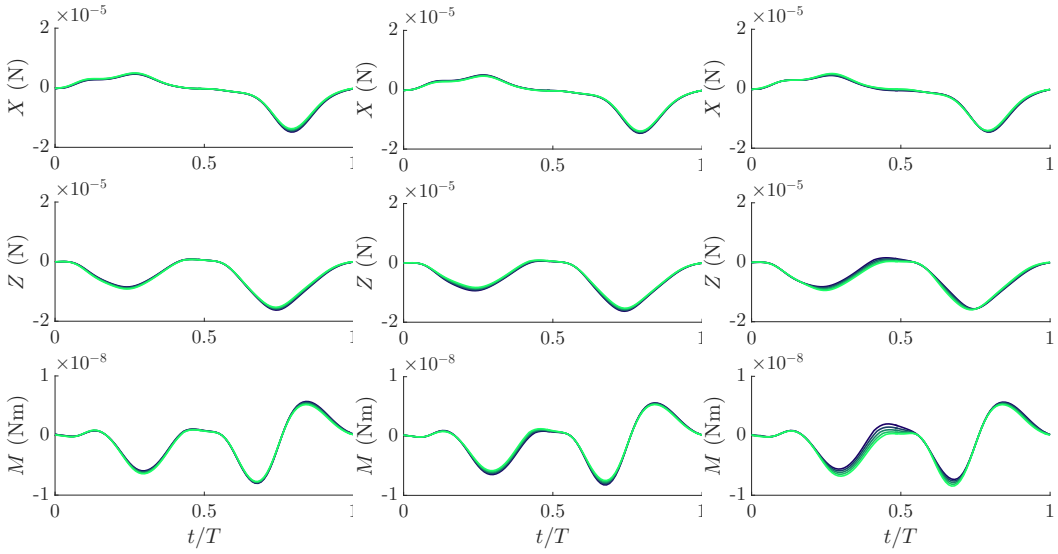


Fig. C.6: Longitudinal loads calculated using the quasi-steady method over a single wingstroke for the *Drosophila* in fast forward flight. Left three plots show loads for varying Δu, center 3 show loads for varying Δw, right 3 show loads for varying Δq.

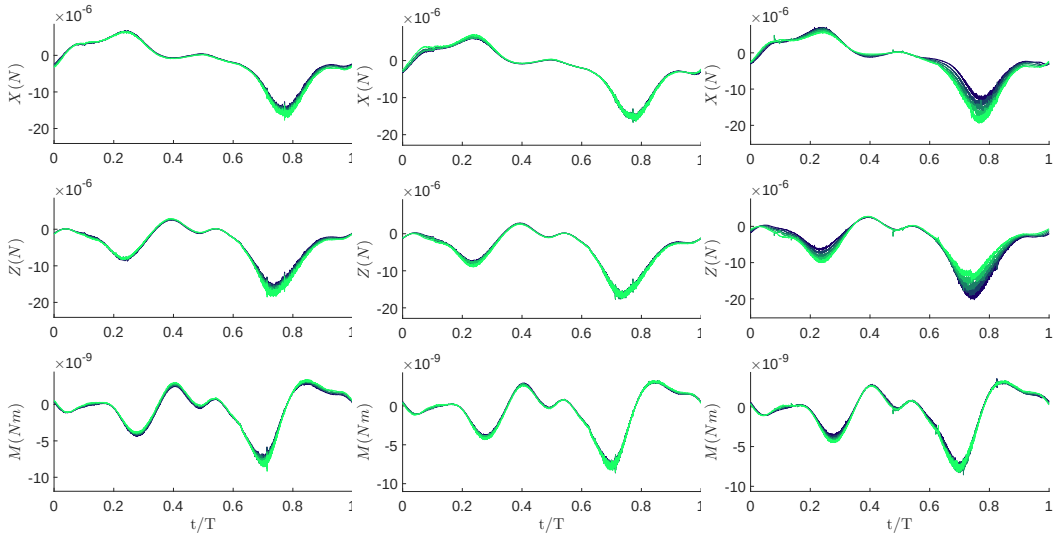


Fig. C.7: Longitudinal loads calculated by IBINS CFD over a single wingstroke for the *Drosophila* in fast forward flight. Left three plots show loads for varying Δu, center 3 show loads for varying Δw, right 3 show loads for varying Δq.

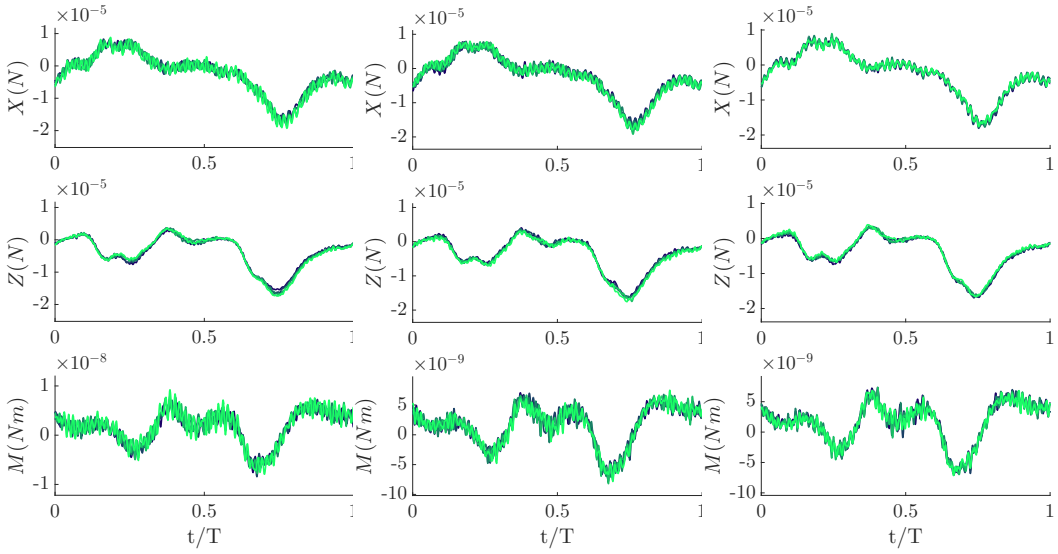


Fig. C.8: Longitudinal loads measured using Robofly over a single wingstroke for the *Drosophila* in fast forward flight. Left three plots show loads for varying Δu, center 3 show loads for varying Δw, right 3 show loads for varying Δq.

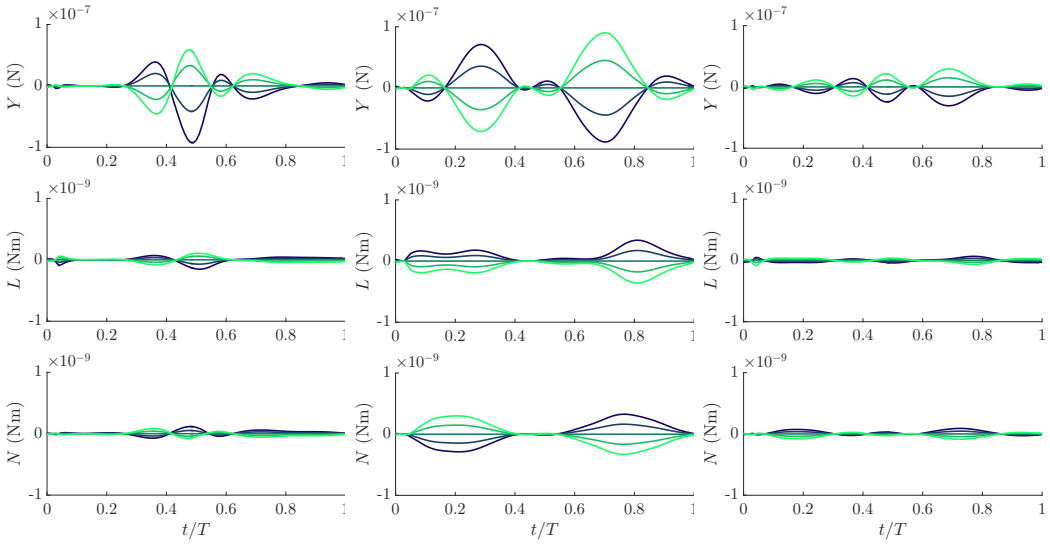


Fig. C.9: Lateral-directional loads calculated by the quasi-steady method over a single wingstroke for the *Drosophila* in fast forward flight. Left three plots show loads for varying Δv, center 3 show loads for varying Δp, right 3 show loads for varying Δr.

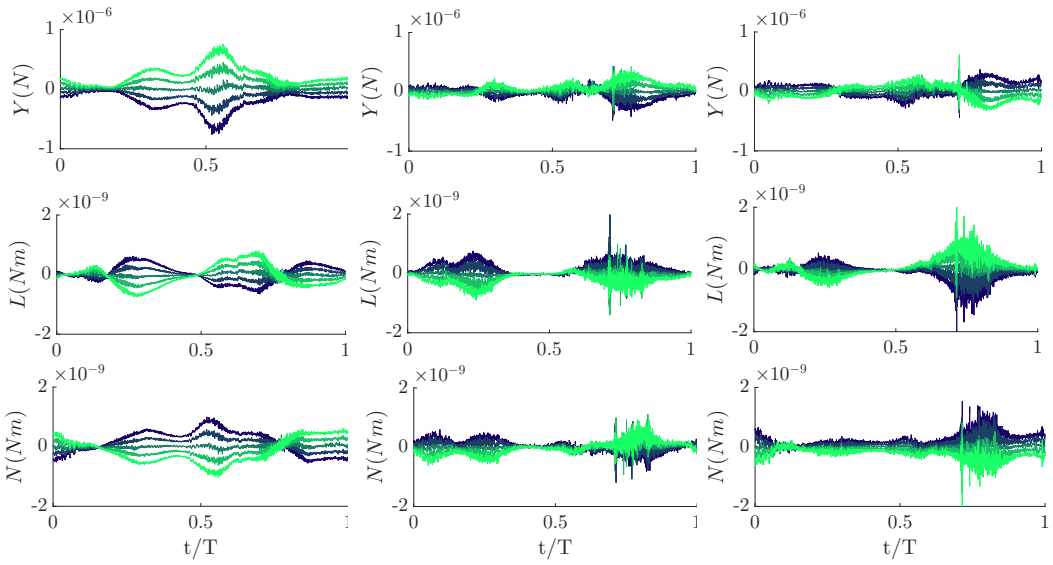


Fig. C.10: Lateral-directional loads calculated by IBINS CFD over a single wingstroke for the *Drosophila* in fast forward flight. Left three plots show loads for varying Δv, center 3 show loads for varying Δp, right 3 show loads for varying Δr.

C.2 Flapping wing MAV

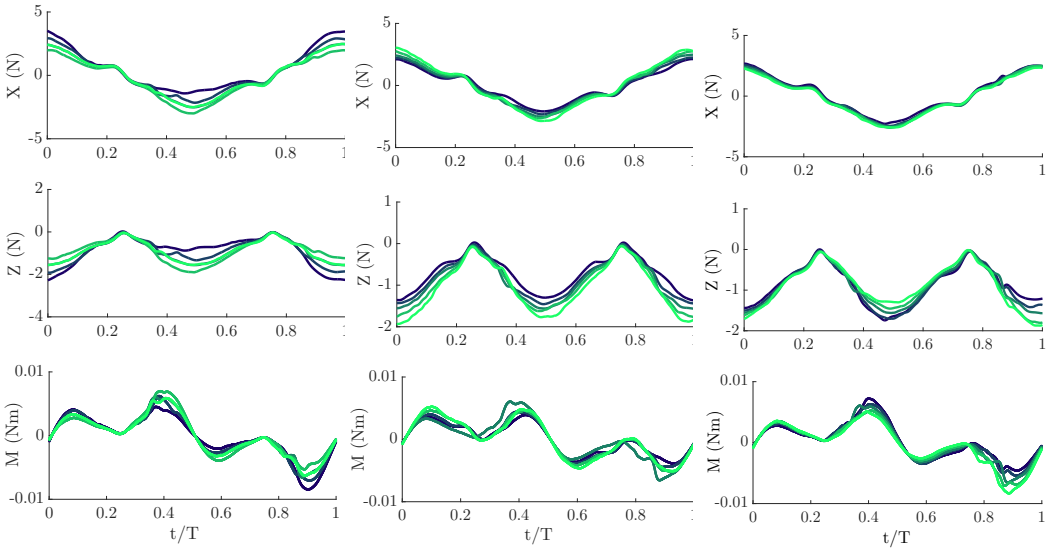


Fig. C.11: Longitudinal loads calculated by OVERTURNS CFD over a single wingstroke for the flapping wing MAV in hover. Left three plots show loads for varying Δu, center 3 show loads for varying Δw, right 3 show loads for varying Δq.

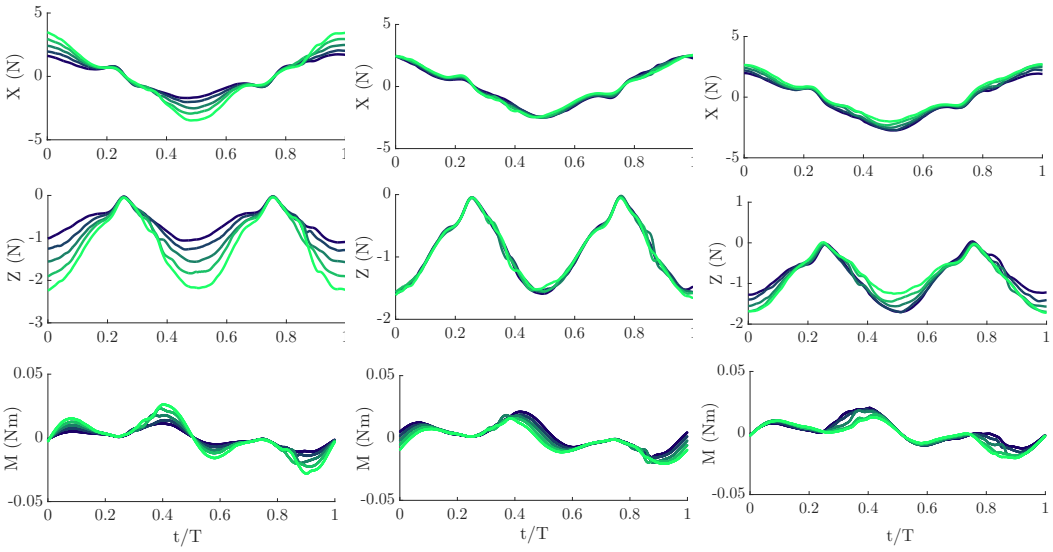


Fig. C.12: Longitudinal loads calculated by OVERTURNS CFD over a single wingstroke for the flapping wing MAV in hover. Left three plots show loads for varying Δu, center 3 show loads for varying Δw, right 3 show loads for varying Δq.

Bibliography

[1] Unmanned Aerial Vehicle Systems Association. Civil and commercial uas applications. https://www.uavs.org/commercial, 2016. Accessed: 2016-12-24.

[2] CBS Interactive Inc. Amazon unveils futuristic plan: delivery by drone. http://www.cbsnews.com/news/amazon-unveils-futuristic-plan-delivery-by-drone/, 2013. Accessed: 2016-12-22.

[3] Kyle Wiggers. Google has patented a drone that delivers medical supplies on demand. http://www.digitaltrends.com/cool-tech/google-patent-medical-supply-drone/, 2016. Accessed: 2016-12-22.

[4] April Glaser. Ups successfully delivered medical supplies by drone to an island off the atlantic coast. http://flyzipline.com/product/, 2016. Accessed: 2016-12-22.

[5] Amar Toor. This startup is using drones to deliver medicine in rwanda. http://www.theverge.com/2016/4/5/11367274/zipline-drone-delivery-rwanda-medicine-blood.

[6] Aaron Mamiit. Facebook's aquila soars in test flight: Solar-powered drone will provide internet access to everyone. http://http://www.techtimes.com/articles/170974/20160722/facebooks-aquila-soars-in-test-flight-solar-powered-drone-will-provide-internet-access-to-everyone.htm, 2016. Accessed: 2016-12-23.

[7] US Department of Transportation Federal Aviation Administration. Small unmanned aircraft rule (part 107), 2016.

[8] US Department of Transportation Federal Aviation Administration. Press release – FAA registered nearly 300,000 unmanned aircraft owners. https://www.faa.gov/news/press_releases/news_story.cfm?newsId=19914, 2016. accessed: 2016-12-22.

[9] James M McMichael and Michael S Francis. Micro air vehicles-toward a new dimension in flight. *U.S. Defense Advanced Research Projects Agency*, 1997.

[10] K Chang, P Rammos, SA Wilkerson, M Bundy, and S Andrew Gadsden. Lipo battery energy studies for improved flight performance of unmanned aerial systems. In *SPIE Defense+ Security*, pages 98370W–98370W. International Society for Optics and Photonics, 2016.

[11] Stephen J Morris. Design and flight test results for micro-sized fixed-wing and vtol aircraft. In *Proceedings of the First International Conference on Emerging Technologies for Micro Ai Vehicles, Georgia Institute of Technology, Atlanta, GA*. Citeseer, 1997.

[12] Joel Grasmeyer and Matthew Keennon. Development of the black widow micro air vehicle. In *39th aerospace sciences meeting and exhibit*, page 127, 2001.

[13] Brent Petersen, Byron Erath, Kevin Henry, Mark Lyon, Kendall Fowkes, and W Jerry Bowman. Development of a micro air vehicle for maximum endurance and minimum size. In *41st Aerospace Sciences Meeting and Exhibit*, page 416, 2003.

[14] Randal W Beard, Derek Kingston, Morgan Quigley, Deryl Snyder, Reed Christiansen, Walt Johnson, Timothy McLain, and Michael Goodrich. Autonomous vehicle technologies for small fixed-wing uavs. *Journal of Aerospace Computing, Information, and Communication*, 2(1):92–108, 2005.

[15] Cezary R Galinski. Gust resistant fixed wing micro air vehicle. *Journal of aircraft*, 43(5):1586–1588, 2006.

[16] P Ifju, D Jenkins, Scott Ettinger, Yongsheng Lian, Wei Shyy, and M Waszak. Flexible-wing-based micro air vehicles. In *40th AIAA Aerospace Sciences Meeting & Exhibit*, page 705, 2002.

[17] Felipe Bohorquez, Paul Samuel, Jayant Sirohi, Darryll Pines, Lael Rudd, and Ron Perel. Design, analysis and hover performance of a rotary wing micro air vehicle. *Journal of the American Helicopter Society*, 48(2):80–90, 2003.

[18] Matthew Keennon, Karl Klingebiel, and Henry Won. Development of the nano hummingbird: A tailless flapping wing micro air vehicle. In *50th AIAA Aerospace Sciences Meeting including the New Horizons Forum and Aerospace Exposition*, page 588, 2012.

[19] Robert J Wood. The first takeoff of a biologically inspired at-scale robotic insect. *IEEE transactions on robotics*, 24(2):341–347, 2008.

[20] GCHE De Croon, KME De Clercq, Remes Ruijsink, B Remes, and C De Wagter. Design, aerodynamics, and vision-based control of the delfly. *International Journal of Micro Air Vehicles*, 1(2):71–97, 2009.

[21] Larry Young, Edwin Aiken, Jeffrey Johnson, Raymond Demblewski, Jason Andrews, and James Klem. New concepts and perspectives on micro-rotorcraft and small autonomous rotary-wing vehicles. In *20th AIAA Applied Aerodynamics Conference*, page 2816, 2002.

[22] Samir Bouabdallah, Pierpaolo Murrieri, and Roland Siegwart. Design and control of an indoor micro quadrotor. In *Robotics and Automation, 2004. Proceedings. ICRA'04. 2004 IEEE International Conference on*, volume 5, pages 4393–4398. IEEE, 2004.

[23] V Hrishikeshavan and I Chopra. Design and testing of a shrouded rotor mav with anti-torque vanes. In *Proceedings of the 64th Annual National Forum of the American Helicopter Society, Montreal, Canada*, 2008.

[24] Joseph K Conroy, J Sean Humbert, and Darryll J Pines. System identification of a rotary-wing micro air vehicle. *Journal of the American Helicopter Society*, 56(2):25001–25001, 2011.

[25] John Gerdes, Alex Holness, Ariel Perez-Rosado, Luke Roberts, Adrian Greisinger, Eli Barnett, Johannes Kempny, Deepak Lingam, Chen-Haur Yeh, Hugh A Bruck, et al. Robo raven: a flapping-wing air vehicle with highly compliant and independently controlled wings. *Soft Robotics*, 1(4):275–288, 2014.

[26] T Nick Pornsin-Sirirak, Yu-Chong Tai, Chih-Ming Ho, and Matt Keennon. Microbat: A palm-sized electrically powered ornithopter. In *Proceedings of NASA/JPL Workshop on Biomorphic Robotics*, pages 14–17, 2001.

[27] Rajkiran Madangopal, Zaeem A Khan, and Sunil K Agrawal. Biologically inspired design of small flapping wing air vehicles using four-bar mechanisms and quasi-steady aerodynamics. *Journal of Mechanical Design*, 127(4):809–816, 2005.

[28] Dario Floreano and Robert J Wood. Science, technology and the future of small autonomous drones. *Nature*, 521(7553):460–466, 2015.

[29] Mohamed Gad-el Hak. Flow control: The future. *Journal of aircraft*, 38(3):402–418, 2001.

[30] J.G. Leishman. *Principles of Helicopter Dynamics*. Cambridge University Press, New York, 2 edition, 2006.

[31] Benjamin R Hein and Inderjit Chopra. Hover performance of a micro air vehicle: rotors at low reynolds number. *Journal of the American Helicopter Society*, 52(3):254–262, 2007.

[32] Sam Zarovy, Mark Costello, Ankur Mehta, Greg Gremillion, Derek Miller, Badri Ranganathan, J Sean Humbert, and Paul Samuel. Experimental study of gust effects on micro air vehicles. In *AIAA Atmospheric Flight Mechanics Conference*, page 7818, 2010.

[33] Darryll J Pines and Felipe Bohorquez. Challenges facing future micro-air-vehicle development. *Journal of aircraft*, 43(2):290–305, 2006.

[34] Hendrik Tennekes. *The simple science of flight: from insects to jumbo jets*. MIT press, 2009.

[35] David Lentink and Michael H Dickinson. Rotational accelerations stabilize leading edge vortices on revolving fly wings. *Journal of Experimental Biology*, 212(16):2705–2719, 2009.

[36] Michael H Dickinson and Karl G Goetz. Unsteady aerodynamic performance of model wings at low reynolds numbers. *Journal of Experimental Biology*, pages 45–45, 1993.

[37] Coen Van Den Berg and Charles P Ellington. The vortex wake of a hovering model hawkmoth. *Philosophical Transactions of the Royal Society of London B: Biological Sciences*, 352(1351):317–328, 1997.

[38] Jason T Vance, Douglas L Altshuler, William B Dickson, Michael H Dickinson, and Stephen P Roberts. Hovering flight in the honeybee apis mellifera: kinematic mechanisms for varying aerodynamic forces. *Physiological and Biochemical Zoology*, 87(6):870–881, 2014.

[39] Leif Ristroph, Attila J Bergou, John Guckenheimer, Z Jane Wang, and Itai Cohen. Paddling mode of forward flight in insects. *Physical review letters*, 106(17):178103, 2011.

[40] T. Weis-Fogh. Energetics of hovering flight in hummingbirds and *Drosophila*. *The Journal of Experimental Biology*, 56:79–107, 1972.

[41] Fritz-Olaf Lehmann, Sanjay P Sane, and Michael Dickinson. The aerodynamic effects of wing–wing interaction in flapping insect wings. *Journal of Experimental Biology*, 208(16):3075–3092, 2005.

[42] Matthew M Parsons, Holger G Krapp, and Simon B Laughlin. Sensor fusion in identified visual interneurons. *Current Biology*, 20(7):624–628, 2010.

[43] Graham K Taylor and Holger G Krapp. Sensory systems and flight stability: what do insects measure and why? *Advances in insect physiology*, 34:231–316, 2007.

[44] Gregory Gremillion, J Sean Humbert, and Holger G Krapp. Bio-inspired modeling and implementation of the ocelli visual system of flying insects. *Biological cybernetics*, 108(6):735–746, 2014.

[45] I. Faruque and J.S. Humbert. Dipteran insect flight dynamics. part 1: Longitudinal motion about hover. *The Journal of Theoretical Biology*, 264(2):538–552, 2010.

[46] Taylor, G. and Thomas, A. Dynamic flight stability in the desert locust *Schistocerca gregaria*. *The Journal of Experimental Biology*, 206:2803–2829, 2003.

[47] Dickson, W., Polidoro, P., Tanner, M., and Dickinson, M. A linear systems analysis of the yaw dynamics of a dynamically scaled insect model. *Journal of Experimental Biology*, 213:3047–3061, 2010.

[48] Hesselberg, T. and Lehman, F. Turning behavior depends on frictional damping in the fruitfly drosophila. *Journal of Experimental Biology*, 210:4319–4334, 2007.

[49] Sun, M. and Xiong, Y. Dynamic flight stability of a hovering bumblebee. *The Journal of Experimental Biology*, 208:447–459, 2005.

[50] Sun, M., Wang, J., and Xiong, Y. Dynamic flight stability of hovering insects. *Acta Mechanica Sinica*, 23:231–246, 2007.

[51] Yanlai Zhang and Mao Sun. Dynamic flight stability of a hovering model insect: lateral motion. *Acta Mechanica Sinica*, 26(2):175–190, 2010.

[52] Gao, N., Aono, H., and Liu, H. Perturbation analysis of 6dof flight dynamics and passive dynamic stability of hovering fruit fly *Drosophila Melanogaster*. *Journal of Theoretical Biology*, 270:98–111, 2011.

[53] C.P. Ellington. The aerodynamics of hovering insect flight i: The quasi-steady analysis. *Philosophical Transactions of the Royal Society of London*, 305 Series B:1–15, 1984.

[54] Dickinson, M., Lehmann, F., and Sane, S. Wing rotation and the aerodynamic basis of insect flight. *Science*, 284:1954–1960, 1999.

[55] C.P. Ellington. The aerodynamics of hovering insect flight ii: Morphological parameters. *Philosophical Transactions of the Royal Society of London*, 305 Series B:17–40, 1984.

[56] Sane, S. and Dickinson, M. The aerodynamic effects of wing rotation and a revised quasi-steady model of flapping flight. *The Journal of Experimental Biology*, 205:1087–1096, 2002.

[57] Herbert Wagner. Über die entstehung des dynamischen auftriebes von tragflügeln. *ZAMM-Journal of Applied Mathematics and Mechanics/Zeitschrift für Angewandte Mathematik und Mechanik*, 5(1):17–35, 1925.

[58] Theodore Theodorsen. Generaltheoryofaerodynamicinstabilityand themechanismof flutter. *NACARep*, 496:7, 1935.

[59] TH Von Karman. Airfoil theory for non-uniform motion. *Journal of the Aeronautical Sciences*, 5(10):379–390, 1938.

[60] TS Beddoes. A synthesis of unsteady aerodynamic effects including stall hysteresis. *Vertica*, 1(2):113–123, 1976.

[61] J Gordon Leishman and TS Beddoes. A semi-empirical model for dynamic stall. *Journal of the American Helicopter society*, 34(3):3–17, 1989.

[62] Haithem E Taha, Muhammad R Hajj, and Philip S Beran. State-space representation of the unsteady aerodynamics of flapping flight. *Aerospace Science and Technology*, 34:1–11, 2014.

[63] Julian D Cole. Perturbation methods in applied mathematics blaisdell. *Waltham, Mass*, 1968.

[64] Jiang Hao Wu and Mao Sun. Floquet stability analysis of the longitudinal dynamics of two hovering model insects. *Journal of The Royal Society Interface*, 9(74):2033–2046, 2012.

[65] Zhang, Y.L. and Sun, M. Control for small-speed lateral flight in a model insect. *Bioinspiration & Biomechanics*, 2011.

[66] Na Xu and Mao Sun. Lateral dynamic flight stability of a model bumblebee in hovering and forward flight. *Journal of theoretical biology*, 319:102–115, 2013.

[67] Michael F Land and TS Collett. Chasing behaviour of houseflies (fannia canicularis). *Journal of comparative physiology*, 89(4):331–357, 1974.

[68] Roger C Hardie and Padinjat Raghu. Visual transduction in drosophila. *Nature*, 413(6852):186–193, 2001.

[69] Gerbera Nalbach and R Hengstenberg. The halteres of the blowfly calliphora. *Journal of Comparative Physiology A*, 175(6):695–708, 1994.

[70] Jerome Casas and Stephen Simpson. *Advances in Insect Physiology: Insect Mechanics and Control*, volume 34. Academic Press, 2007.

[71] Amir Fayyazuddin and Michael H Dickinson. Haltere afferents provide direct, electrotonic input to a steering motor neuron in the blowfly, calliphora. *Journal of Neuroscience*, 16(16):5225–5232, 1996.

[72] I. Faruque and J.S. Humbert. Dipteran insect flight dynamics. part 2: Lateral-directional motion about hover. *The Journal of Theoretical Biology*, 265(3):306–313, 2010.

[73] Gordon J Berman and Z Wang. Energy-minimizing kinematics in hovering insect flight. *Journal of Fluid Mechanics*, 582:153–168, 2007.

[74] Fritz-Olaf Lehmann and Michael H Dickinson. The control of wing kinematics and flight forces in fruit flies (drosophila spp.). *The Journal of experimental biology*, 201(3):385–401, 1998.

[75] Sanjay P Sane and Michael H Dickinson. The control of flight force by a flapping wing: lift and drag production. *Journal of experimental biology*, 204(15):2607–2626, 2001.

[76] J Sean Humbert and Imraan A Faruque. Analysis of insect-inspired wingstroke kinematic perturbations for longitudinal control. *Journal of Guidance, Control, and Dynamics*, 34(2):618–623, 2011.

[77] T. Hedrick. Software techniques for two and three-dimensional kinematic measurements of biological and biomimetic systems. *Journal of Bioinspiration and Biomimetics*, 2008.

[78] M. Osborne. Aerodynamics of flapping flight with applications to insects. *The Journal of Experimental Biology*, 28(2):221–245, 1951.

[79] Shyy, W., Lian, Y., Tang, J., Viieru, D., and Liu, H. *Aerodynamics of Low Reynolds Number Flyers*. Cambridge University Press, New York, 2008.

[80] C.P. Ellington. The aerodynamics of hovering insect flight iii: Kinematics. *Philosophical Transactions of the Royal Society of London*, 305 Series B:41–78, 1984.

[81] Bush, B. and Baeder, J. Force production mechanisms of a flapping mav wing. In *AHS International Specialists Conference on Aeromechanics*, San Fransisco, CA, January 23–25 2008.

[82] Bush, B., MacFarlane, K., Baeder, J., and Humbert, J.S. Development of immersed boundary code with application to mav stability analysis. In *27th Army Science Conference*, Orlando, FL, November 29 – December 2 2010.

[83] Kim, J. and Moin, P. Application of a fractional-step method to incompressible navier-stokes equations. *Journal of Computational Physics*, 59:308–323, 1984.

[84] C.P. Ellington. The aerodynamics of hovering insect flight vi: Lift and power requirements. *Philosophical Transactions of the Royal Society of London*, 305 Series B:115–144, 1984.

[85] Fritz-Olaf Lehmann and Michael H Dickinson. The changes in power requirements and muscle efficiency during elevated force production in the fruit fly drosophila melanogaster. *Journal of Experimental Biology*, 200(7):1133–1143, 1997.

[86] Xinyan Deng, Luca Schenato, Wei Chung Wu, and S Shankar Sastry. Flapping flight for biomimetic robotic insects: Part i-system modeling. *Robotics, IEEE Transactions on*, 22(4):776–788, 2006.

[87] Gratzel, C., Nelson, B., and Fry, S. Frequency response of lift control in *Drosophila*. *Journal of the Royal Society Interface*, 7:1603–1616, 2010.

[88] W. Johnson. *Helicopter Theory*. Dover Publications, Inc., New York, 1994.

[89] Kemin Zhou, Gregory Salomon, and Eva Wu. Balanced realization and model reduction for unstable systems. *International Journal of Robust and Nonlinear Control*, 9(3):183–198, 1999.

[90] Renee C Gardner and J Sean Humbert. Comparative framework for maneuverability and gust tolerance of microhelicopters. *Journal of Aircraft*, pages 1–8, 2014.

[91] Steven N Fry, Rosalyn Sayaman, and Michael H Dickinson. The aerodynamics of hovering flight in drosophila. *Journal of Experimental Biology*, 208(12):2303–2318, 2005.

[92] Seth A Budick and Michael H Dickinson. Free-flight responses of drosophila melanogaster to attractive odors. *Journal of experimental biology*, 209(15):3001–3017, 2006.

[93] Markus Mronz and Fritz-Olaf Lehmann. The free-flight response of drosophila to motion of the visual environment. *Journal of Experimental Biology*, 211(13):2026–2045, 2008.

[94] A Roland Ennos. The kinematics an daerodynamics of the free flight of some diptera. *Journal of Experimental Biology*, 142(1):49–85, 1989.

[95] JM Zanker. The wing beat of drosophila melanogaster. i. kinematics. *Philosophical Transactions of the Royal Society of London. B, Biological Sciences*, 327(1238):1–18, 1990.

[96] Michael H Dickinson, Fritz-Olaf Lehmann, and KG Gotz. The active control of wing rotation by drosophila. *Journal of experimental biology*, 182(1):173–189, 1993.

[97] Steven N Fry, Rosalyn Sayaman, and Michael H Dickinson. The aerodynamics of free-flight maneuvers in drosophila. *Science*, 300(5618):495–498, 2003.

[98] John C Doyle, Keith Glover, Pramod P Khargonekar, and Bruce A Francis. State-space solutions to standard H_2 and H_∞ control problems. *IEEE Transactions on Automatic control*, 34(8):831–847, 1989.

[99] Randal K Douglas, Robert H Chen, and Jason L Speyer. Linear system input-order reduction by hankel norm maximization. *Journal of guidance, control, and dynamics*, 27(1):150–154, 2004.

[100] RA Thompson, MF Wehling, J Evers, and WE Dixon. Evaluation of the haltere as a biologically inspired inertial rate measurement sensor. In *Guidance, Navigation, and Control Conference*, 2008.

[101] MS Tu and MH Dickinson. The control of wing kinematics by two steering muscles of the blowfly (calliphora vicina). *Journal of Comparative Physiology A*, 178(6):813–830, 1996.

[102] Claire N Balint and Michael H Dickinson. The correlation between wing kinematics and steering muscle activity in the blowfly calliphora vicina. *Journal of experimental biology*, 204(24):4213–4226, 2001.

[103] David Coleman and Moble Benedict. On the development of a robotic hummingbird. In *54th AIAA Aerospace Sciences Meeting*, page 0144, 2016.

[104] Vinod K Lakshminarayan and James D Baeder. Computational investigation of microscale coaxial-rotor aerodynamics in hover. *Journal of Aircraft*, 47(3):940–955, 2010.

[105] Tarandeep S Kalra, Vinod K Lakshminarayan, and James D Baeder. Cfd validation of micro hovering rotor in ground effect. In *American Helicopter Society 66th Annual Forum Proceedings*. Citeseer, 2010.

[106] R Malhan, J Baeder, I Chopra, and P Masarati. Investigation of aerodynamics of flapping wings for mav applications using experiments and cfd–csd analysis. In *Proceedings of the American Helicopter Society 5th International Specialists Meeting on Unmanned Rotorcraft and Network Centric Operations, Scottsdale, AZ*, 2013.

[107] Buelow P. E. O., Schwer D. A., Feng J., and C. L. Merkle. A preconditioned dual-time, diagonalized adi scheme for unsteady computations. In *13th AIAA Computational Fluid Dynamics Conference, Snowmass Village, CO*, July, 1997.

[108] Shishir A Pandya, Sankaran Venkateswaran, and Thomas H Pulliam. Implementation of preconditioned dual-time procedures in overflow. *AIAA paper*, 72:2003, 2003.

[109] Philippe R Spalart and Steven R Allmaras. A one equation turbulence model for aerodinamic flows. *AIAA journal*, 94, 1992.

[110] Simon M Walker, Adrian LR Thomas, and Graham K Taylor. Deformable wing kinematics in free-flying hoverflies. *Journal of the Royal Society Interface*, page rsif20090120, 2009.

[111] Siddarth Kolluru Venkata and Anya R Jones. Leading-edge vortex structure over multiple revolutions of a rotating wing. *Journal of Aircraft*, 50(4):1312–1316, 2013.